Master's thesis in Engineering Nanoscience

Exploring the effects of pressure on the magnetic properties of quasi-low dimensional quantum magnets via thermodynamic measurements

Emelie Zhu

Division of Synchrotron Radiation Research
Department of Physics

Supervisor: Elizabeth Blackburn

Co-supervisor: Ekaterina Klyushina

Examiner: Francesca Curbis

March 5, 2024

Abstract

Four model solid state compounds were used to experimentally investigate the effects of pressure on the interactions in one- and two-dimensional Heisenberg magnetic models. $BaCuSi_2O_6$, $BaCu_2V_2O_8$, $SrCuO_2$ and $CuGeO_3$ were successfully synthesized via solid-state reactions and characterized via x-ray diffraction. $BaCu_2V_2O_8$ was additionally characterized via spectroscopic techniques to confirm the oxidation state of the material.

The powder magnetic susceptibility of $BaCuSi_2O_6$ was successfully measured and analyzed both at ambient conditions and under applied pressures. The extracted values of $J_{intra} \sim 4.4$ meV and $J_{inter} \sim 0.75$ meV at ambient pressure were found to be in good agreement with previously published data. We found that applying pressure significantly increases the interdimer interaction while the dominant intradimer interaction is only slightly affected by applying pressure.

The single crystal magnetic susceptibility of $BaCu_2V_2O_8$ was successfully measured and analyzed in ambient conditions. The extracted values of the strong intradimer interaction $J_{intra} = 39.39$ meV and the weaker interdimer interaction $J'_{inter} = -15$ meV were found to be in good and reasonable agreement respectively with published results.

Measurements of single crystal magnetic susceptibility of $BaCu_2V_2O_8$ under applied pressure have been done but analysis require additional background measurements of the pressure cell.

Low dimensional quantum magnets: what are they and how are they affected by pressure?

By: *Emelie Zhu*

The properties of quantum magnets are determined by the interactions of ions in a material. By measuring the bulk, we gained insight on how the individuals ions behave.

Recently quantum devices have become an increasingly fascinating and promising technology. To keep up with these advances, new materials and new phenomena need to be explored and understood so that we have replacements ready when “modern” technology eventually become obsolete. The phenomenon of interest in this work is quantum magnetism. Superconductors, quantum computers and spintronics are just a few technologies that will benefit from quantum magnetism.

Classically, magnetism is about collective behavior of a large group of atoms. Quantum magnetism instead describes the magnetic properties of individual atoms. More specifically we looked at “paired up” magnetic atoms. Surprisingly enough, the properties of individual atoms and pairs can be observed through measurements of the whole material.

The goal was to study the effect of pressure on quantum magnets. We estimated the pair-creating interaction in these magnetic materials. We did this both for a regular measurement and after applying pressure to the material. We found that applying pressure changes the strength of the interactions but not the nature of the interactions.

The reason why pressure is of interest is because pressure can change the properties of materials. For example, everyone knows that water boils at 100 degrees Celsius. This is however not true on Mount Everest where water boils at 70 degrees Celsius. This is because the (atmospheric) pressure is lower on Mount Everest than on most inhabited places on Earth. Another example is that applying pressure on ice can cause it to melt. While water is a simple molecule with two atom-types as building blocks, the quantum magnets studied in this project consist of many different types of atoms that have their own effects on the overall material. Therefore, the explanations to explain these magnetic materials isn’t always straightforward.

The quantum magnets were first synthesized since they are rather complicated structures and can’t be bought. After making the magnets and looking at how purely they were made, we continued to study two.

The magnetic material studied most thoroughly was used in ancient China as a pigment known as *Han purple* or *Chinese purple*. It was already produced in 800 BC and later used as decorative paint on the famous terracotta warriors from 220 AD. However, this special material disappeared in the following 17 centuries, only to be discovered together with the terracotta statues in 1974. It would take another two decades before chemists knew how to make it again. Today we consider this ancient pigment as a potential messenger of our path to the future of quantum magnetism.

Abbreviations

1D one-dimensional

2D two-dimensional

AC alternating current

AFM antiferromagnetic

AP ambient pressure

CIF Crystallographic Information File

DC direct current

FM ferromagnetic

NEXAFS Near-Edge X-ray Absorption Fine Structure

PXRD Powder X-Ray Diffraction

SQUID Superconducting Quantum Interference Device

TSFZ travelling-solvent floating zone

XAS X-ray Absorption Spectroscopy

XPS X-ray Photoelectron Spectroscopy

XRD X-Ray Diffraction

Acknowledgements

To start, I would like to thank my supervisor Elizabeth Blackburn and Ekaterina Klyushina for your guidance and support during this project. Your expertise has been invaluable throughout this journey and without it my thesis would not have been feasible and I would not have learned as much as I have. I am grateful to you both for this challenging but exciting experience as well since it has given me the opportunity to try on many new techniques, gone to new places and met so many helpful and friendly people.

I would also like to express my sincere gratitude to the following individuals whose contributions have been invaluable in the completion of this thesis:

To Mingee Chung, Matthew Coak, and Aly Abdeldaim from the Condensed Matter Physics group at the University of Birmingham, I extend my heartfelt gratitude for the access to the MPMS and pressure cell. I truly appreciate your assistance with my measurements and your valuable suggestions throughout this project. Without your help I would not have been able to begin to explore my thesis questions.

Special thanks to Alexander Klyushin at the SPECIES-beamline at MAX for his support and guidance in all matters pertaining to spectroscopy and MAX IV. From helping me with the beamtime proposal to conducting measurements and answering my questions, your expertise and patience proved indispensable. I enjoyed my beamtime and experience of a synchrotron facility despite the long hours.

I am grateful to Nazmul Islam at Helmholtz Zentrum Berlin für Materialien und Energie (HZB) for letting me use your equipment at HZB to synthesize $CuGeO_3$. It was interesting to see the insides of a research institute in Germany and $CuGeO_3$ was one of my favourite compounds to synthesize.

Thank you to Mark Rambaran at the Centre for Analysis and Synthesis for helping me with finding the best PXRD-settings for my compounds and with pelletizing my samples. My samples would not have been ready for measurement without your guidance.

I would also like to thank Oskar Stepancic and Ahmed Alshemi from the 'Magnetism and superconductivity' group for their help when others in the research group were away on experiments. Thank you both for unlocking doors and helping me with the most random but essential problems that cropped up.

Finally, I must thank my friends and family who have supported me during this whole process. Thank you for always believing in me and seeing my strengths when I wasn't quite as willing to do so for myself.

Contents

Chapter 1

Introduction

This thesis aims to explore the effects of pressure on the magnetic properties of quasi-low dimensional quantum magnets via thermodynamic measurements.

Magnetism is a phenomena most people encounter in their daily lives, whether it is the magnets on your fridge, the compass you bring on a hike or the NMR or MRI scan you may have at a hospital. What is not commonly known is that the repulsive and attractive interactions between the electrons of atoms are what govern the macroscopic properties of magnets. Magnetism is still of fundamental interest in condensed matter physics because of the different novel phenomena exhibited in different magnetic systems. Low dimensional magnets are currently of interest because we can use them to experimentally observe theoretically predicted novel magnetic phenomena. However low dimensional magnetic systems only exhibit these phenomena at lower temperatures where the behavior-governing magnetic interactions exceed the fluctuations caused by temperature.

The objective of this thesis is to explore the effects of pressure on a series of four compounds, $BaCuSi_2O_6$, $BaCu_2V_2O_8$, $SrCuO_2$ and $CuGeO_3$, that are copper based antiferromagnets where the Cu^{2+} ions carry $S = \frac{1}{2}$. All four compounds are almost ideal physical realizations of various one-dimensional (1D) and two-dimensional (2D) quantum magnetic models whose magnetic properties are well understood at ambient pressure and the main goal of this thesis is to investigate how the magnetic exchange interactions change due to pressure in these systems.

The structure of the thesis is outlined as following. An introduction to the context and objective of the thesis is stated in the rest of this chapter. Chapter 2 provides the reader with a more in depth theoretical background to the magnetic behavior of low dimensional magnets, the models describing these systems and information on how the systems can be analyzed through their bulk properties. In Chapter 3 an overview of the experimental techniques used in this thesis will be given. Chapter 4 will have four subchapters for every compound studied in this thesis: $BaCuSi_2O_6$, $BaCu_2V_2O_8$, $SrCuO_2$ and $CuGeO_3$. All subchapters will follow the same structure beginning with an overview and literature investigation of the compound, followed by a section on synthesis and characterization via powder X-ray diffraction and spectroscopic techniques where they where used. Only the magnetic properties of $BaCuSi_2O_6$ and $BaCu_2V_2O_8$ were measured and analyzed, with the latter only for ambient pressure. The magnetic properties of $SrCuO_2$ were measured but not analyzed due to time constraints. Finally a summarizing discussion and outlook are given in Chapter 5.

Chapter 2

Theoretical Background

This chapter is divided in three parts. The first part will provide the reader with the background to where magnetism originates from and the second part will introduce the different magnetic systems studied. The final part will introduce the theoretical concepts necessary to understand the magnetic properties and analysis of the results.

A short introduction to the three types of magnetism that will be discussed will first be given: paramagnetism, ferromagnetism and antiferromagnetism. All types of magnetism are dictated by the unpaired electrons in the shells and orbitals of atoms and the different behavior they exhibit.

Paramagnetism is when an externally applied magnetic field weakly induces internal magnetic fields that align with the externally applied field in a material. It occurs because unpaired electrons in the material have a magnetic moment, spin. The spins are oriented randomly until the external magnetic field is applied and revert to being oriented randomly once the external field is removed. This behavior is typical of many magnetic materials at high temperature.

Ferromagnetism is the type of magnetism that is most commonly associated with magnetism; ferromagnetic materials are strongly attracted to magnets and can magnetize permanently if the material or the applied magnetic field is strong enough. Neighboring spins align parallel in ferromagnetic interaction.

Antiferromagnetism is also an example of ordered magnetism but with a net magnetization of zero. Neighboring spins align antiparallel in antiferromagnetic interaction which leads to a net magnetization of zero. A lattice of antiferromagnetic spins can be decomposed into two sublattices of spins. These are arranged so that electrons with spin up will only be surrounded by electrons with spin down and vice versa.

2.1 Magnetic ions in crystals

Magnetic moment is caused by the unpaired electrons of magnetic ions. To understand this we can first look at the single magnetic ion and its properties.

2.1.1 Free magnetic ion

The magnetic ion consists of nucleus surrounded by the electrons where each electron is characterized by unique set of four quantum numbers: the *principal quantum number* n, the *orbital angular momentum* of the electron l and the *projections* of its *spin* and *orbital angular momentum* on a given z-axis m_s and m_l respectively. The quantum numbers are related via $l = 0, 1, 2, ..., n-1$ and $|m_l| \leq l$ where n can be any natural number. $m_s = +\frac{1}{2}$ or $-\frac{1}{2}$. The spin and orbital angular momenta have magnetic moments associated with them as:

$$\vec{\mu}_s = -g_s \cdot \mu_B \cdot \vec{s} \qquad\qquad \vec{\mu}_l = -g_l \cdot \mu_B \cdot \vec{l}$$

where g_s is the electron-spin g-factor and μ_B is the Bohr magneton. The sum of the spin- and orbit-angular momenta defines the *total angular momentum* $\vec{j} = \vec{s} + \vec{l}$ of single electron. The magnetic moment associated with the total angular momentum is $\vec{\mu}_j = \vec{\mu}_s + \vec{\mu}_l$, where the absolute value equals $|\vec{\mu}_j| = g_j \cdot \mu_B \sqrt{j(j+1)}$ and g_j is the gyromagnetic Landé g-factor.

The g-factor is a unitless quantity that characterizes the total angular momentum of an atom. It is worth noting to not confuse it with other g-factors that describe either the spin or orbital angular momentum of the electron. It helps describe the energy levels of an atom in a weak potential. The electron energy levels in atoms are degenerate with the same angular momentum. However, when the atom is in a weak potential, such as that from a crystal field, the degeneracy is lifted.

When the atom contains several electrons the *total angular momentum* should be calculated either using $\boldsymbol{j}$-$\boldsymbol{j}$-coupling or $\boldsymbol{LS}$-coupling depending on the energy of the *spin-orbit* interaction. If the *spin-orbit* interaction is strong then the total angular momentum should be calculated as a sum of the total angular momenta of all individual electrons otherwise *total angular momentum* can be taken as a sum of total spin $\boldsymbol{S}$ and total orbital angular momentum $\boldsymbol{L}$.

The principal quantum number determine how the electrons are combined into the electronic shells. If the upper occupied shell is not fully filled, the total angular momentum does not vanish. Thus, the electron configuration of the partially filled electron shells is the key to a magnetic ion's behavior. Hund's rules determine how the electrons fill the electron shell to (i) maximise the total spin $\boldsymbol{S}$ and (ii) maximise the total orbital momentum $\boldsymbol{L}$. By maximising $\boldsymbol{S}$, the Coulomb energy is minimized by the Pauli exclusion principle while maximising $\boldsymbol{L}$ reduces Coulomb repulsion between the orbiting electrons. The third rule (iii) states that the ground state is when $\boldsymbol{J}$ is minimized for atoms with less than half-filled shells, $\boldsymbol{J} = |\boldsymbol{L} - \boldsymbol{S}|$, while the ground state for atoms with more than half-filled shells is when $\boldsymbol{J}$ is maximized, $\boldsymbol{J} = |\boldsymbol{L} + \boldsymbol{S}|$.

2.1.2 Crystal field

The attractive and repulsive interactions between many neighboring magnetic ions in crystals form various electrostatic interactions. The potential created by the surrounding crystal is known as the crystal field. The crystal field act as a perturbation on the isolated 'free' magnetic ions. However, the local environment set by the nearest-neighbor ions can be sufficient for determining the energy levels of the magnetic ions.

Crystals have lower symmetry than a spherical Coulomb potential, which leads to energy splitting of the degenerate energy levels. The local crystal environment has a certain symmetry that controls the splitting. Molecular orbitals form how the electron orbitals of the magnetic ion overlap with those of the neighboring ligand ions, splitting the energy levels of the molecular orbitals.

In particular for the copper ion, the five-fold degenerate $3d$-orbital is of interest. The local crystal environment controls the observed crystal field splitting; some examples are illustrated in figure 2.1. Crystal field theory can be used to predict how the environments with their different symmetries will split the orbitals to get different degeneracies, splitting and ordering of the d-orbitals with respect to energetically favorable combinations.

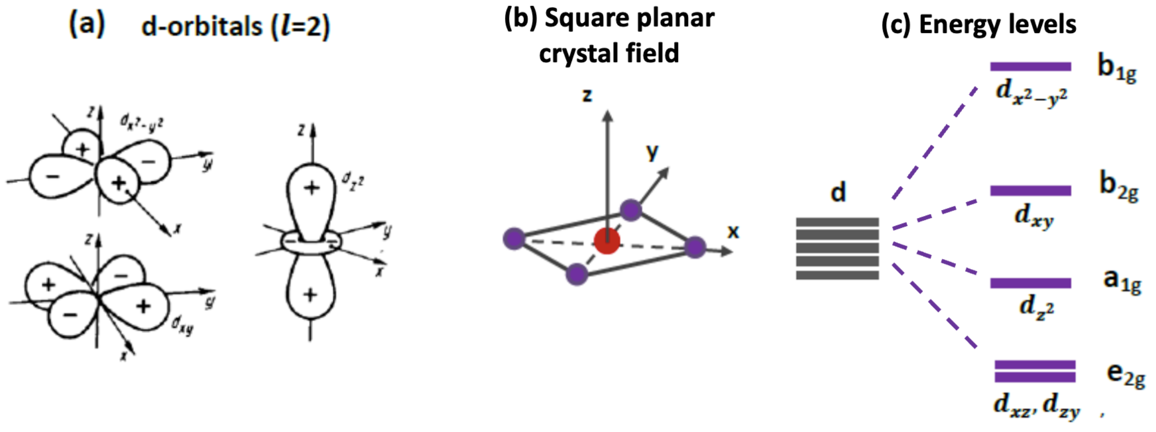

Figure 2.1: (a) The angular distribution of the d-orbital. Positive and negative sign on lobes indicate the phase of the electrons when molecular orbitals are being formed. (b) The crystal field of the d-orbital of an in a square planar environment. (c) The energy levels in the square planar environment. Figure taken with permission from [1]

The square planar geometry, such as those in $[CuO_4]^{2-}$-plaquettes for example, has a low degree of symmetry in the local crystal environment of the magnetic ions. The square planar crystal field splits the five degenerate d-orbitals first into the two lowest lying d_{xz} and d_{zy} d-orbitals that overlap minimally with the oxygen's p-orbitals. Following this, the second d_{z^2} orbital is partially distributed along the plane where the oxygen's p-orbitals lie but the orbitals still overlap only weakly. However, d_{xy} and $d_{x^2-y^2}$ lie within the square plane where the oxygen atoms are located and therefore overlap significantly with the oxygen p-orbitals. d_{xy} point between the oxygen atoms whereas $d_{x^2-y^2}$ point directly towards the oxygen atoms and their p-orbitals. With 9 electrons in the 3d shell of the Cu^{2+} ions discussed in the thesis, the $d_{x^2-y^2}$ orbital will thus be half-filled and responsible for the magnetic properties studied in the compounds of this thesis.

A strong crystal field environment can quench the total orbital angular momentum of magnetic ions, $\boldsymbol{L} = 0$. This leads to a necessary amendment in Hund's third rule in determining the total angular momentum for certain crystal environments and compounds. In a semi-classical understanding quenching originates from the orbital angular momentum precessing in the crystal field so that the magnitude is unchanged but all components average to zero [2]. It results in the quenching of orbital angular momentum in non-degenerate molecular orbitals. This is observed for the electron orbitals in the $3d^9$ Cu^{2+} in a square planar crystal field in the example. The highest molecular orbital b_{1g} is unfilled and non-degenerate. This leads to complete quenching of the orbital angular momentum of the magnetic Cu^{2+} ions in that crystal field. In turn it cannot contribute to the total angular moment $\boldsymbol{J}$ and therefore the total angular momentum is $\boldsymbol{J} = \boldsymbol{S}$.

2.1.3 Magnetic exchange interactions

In magnetic materials, magnetic electrons interact with each other via exchange interactions. The electrons of the same magnetic ions interact with each other but also with the electrons on neighboring magnetic ions. There are different types of magnetic exchange interactions that arise due to different physical processes.

Direct exchange interactions take place between electrons of nearest neighboring ions of the same magnetic atom. When the electron spins are parallel, the Pauli exclusion principle states that they cannot occupy the same orbital while having the same spin.

The *kinetic exchange* interaction is the mechanism that minimizes the kinetic energy of hopping electrons. This mechanism is based on the minimizing of the kinetic energy of the tunnelling electrons due to their spatial delocalization in the bonding state and is the source of interactions between magnetic ions.

For magnetic ions that are spatially separated, their electron orbitals overlap very little and both the direct and kinetic exchange interactions are reduced. This is the case for non-neighboring magnetic ions. Instead the magnetic ions can interact via *superexchange* interaction which is indirect exchange based on the interaction of the magnetic ions with a non-magnetic one between them. Usually superexchange interaction is antiferromagnetic because it lowers the kinetic energy of the system when the electrons can be delocalized over the three atoms. [2] This can be interpreted as virtual electron transfers between the atoms. This behavior can arise in fluorides or in the oxides studied in this thesis.

The Goodenough-Kanamori rule describes the nature of superexchange interactions. It states that the superexchange is antiferromagnetic when the overlapping orbitals are half-filled, which is the case for the Cu-O bonds studied in this thesis. The other part of the rule states that superexchange is ferromagnetic when the virtual shared electron transfer is from a half-filled to an empty orbital or from a filled to a half-filled orbital. The behavior of superexchange interactions is also strongly connected to the Cu-O-Cu bond angles because it directly relates the overlap of the Cu^{2+} d-orbitals to the O^{2-} p-orbitals that mediate the said exchange.

2.2 Low-dimensional Magnetic Models

Despite having a three-dimensional crystal structure, magnetic compounds exhibit magnetic exchange interactions primarily along specific directions. This arises from the fact that the interactions are heavily governed by the overlap of electronic orbitals of neighboring magnetic ions. These orbitals are non-isotropic and follow the crystal symmetry, the electronic structure of the magnetic ions, and the local environment as explored in the previous section. This thesis is interested in Heisenberg chains with spins $S = \frac{1}{2}$. The main focus is on one dimensional magnetic systems but a two dimensional system will also be discussed as well as the excitations that affect the ordering of the different systems. These systems can exhibit three dimensional long range order at temperatures lower than its critical transition temperature due to the excitations of the system.

2.2.1 One and Two Dimensional Magnets

In the Heisenberg model, the spins of the magnetic ions are localized and the spins can point in any direction in three-dimensional space. Neighbouring magnetic ions couple with each other along one specific crystallographic directions via magnetic exchange constants $J_{i,j}$. These exchange constants vary in magnitude along different directions and in sign depending on whether they couple ferromagnetically or antiferromagnetically. The magnetic properties of the Heisenberg model can be described by the Hamiltonian

$$\hat{H} = \sum_{i,j} J_{i,j} \vec{S}_i \cdot \vec{S}_j \tag{2.1}$$

where $\vec{S}_i$ and $\vec{S}_j$ are the total spins of the ith and jth magnetic ions. The coupling is antiferromagnetic if $J_{i,j} > 0$ whilst $J_{i,j} < 0$ implies the coupling is ferromagnetic. The sum is computed over nearest neighbours and can be computed for a lattice of one, two or three dimensions depending on model of the system.

The Uniform 1D $S = 1/2$ Heisenberg Chain

The uniform 1D Heisenberg chain has nearest neighbor interactions only along one axis. The Hamiltonian of the one-dimensional chain reduces to

$$\hat{H} = J \sum_{i} \vec{S}_i \cdot \vec{S}_{i+1} \tag{2.2}$$

due to each spin only having two neighbours that are equally spaced.

For Heisenberg $S = 1/2$ spin chains the excitations are known as spinons. The spinons are fractional excitations that are created in pairs due to the spin-flip. These pairs propagate along the chain and the dispersion relation $\hbar\omega = \pi|J \sin(qa)|$, where J is the antiferromagnetic (AFM) coupling interaction, a and q are the lattice constant and the wavevector along the chain direction respectively [2]. The excitation is gapless for the one dimensional uniform chain with spin $S = 1/2$, see Figure 2.2. However, the magnetic excitation spectrum becomes gapped by Δ upon dimerization as a gap between the singlet ground state ($S = 0$) and the triplet excited states ($S = 1$) is formed. Figure 2.2 shows a schematic of how the excitation spectrum for the uniform Heisenberg chain changes upon dimerization. Note that upon doubling of the real space unit lattice, the Brillouin zone is halved. The further details for the Hamiltonian and energy dispersion of the 1D $S = 1/2$ dimerized chain will be given below.

The $S = 1/2$ Dimerized (Alternating) 1D Heisenberg Chain

In the *1D* $S = 1/2$ *dimerized Heisenberg chain* the magnetic exchange interactions are not uniform and alternate in strength along the chain direction so that the dominant J_{intra} and weaker exchange interactions J_{inter} exists in the system as shown in Figure 2.4. The magnetic ions that interact via strong J_{intra} form pairs – *dimers* – while they weakly interact with each other via J_{inter} along one particular direction forming a *dimerized chain.* The system is typically characterized by the dimerization parameter $\alpha \equiv J_{inter}/J_{intra}$.

The uniform 1D Heisenberg chain is one limit of the dimerized chain where $\alpha = 1$ and $J_{intra} = J_{inter} = J$. The exchange interactions and the geometries of the different chains can be compared schematically in Figures 2.3 and 2.4 respectively.

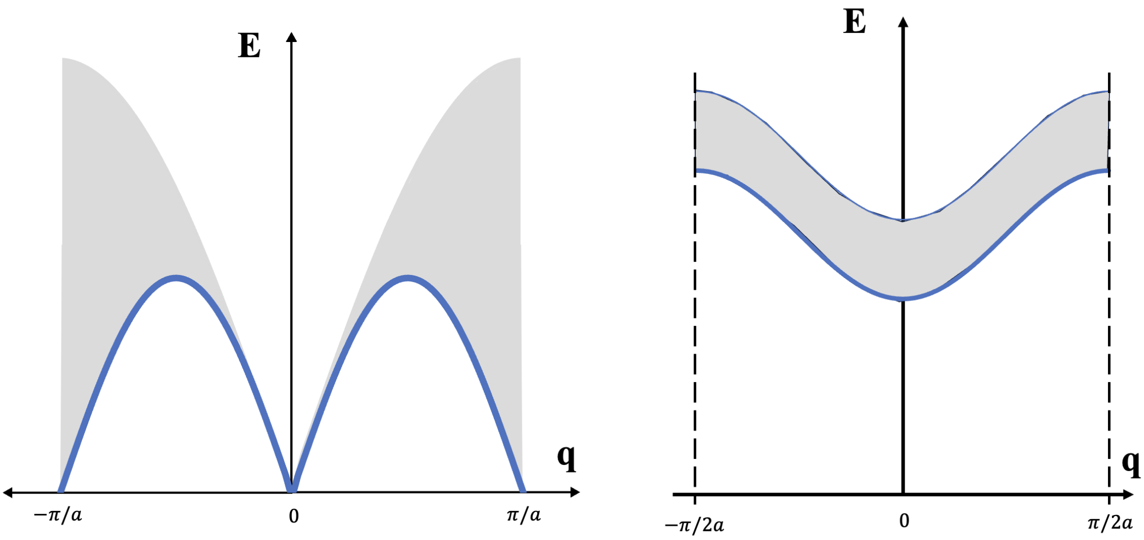

Figure 2.2: Schematic representation of the elementary excitation dispersion spectrum for (a) uniform Heisenberg antiferromagnetic chain and (b) an alternating (dimerized) Heisenberg antiferromagnetic chain. Shaded area correspond to continuum of excitations measured in a neutron scattering experiment. The distance in (b) $2a = a_1 + a_2$ as shown in Figure 2.4. Figure adapted from [2]

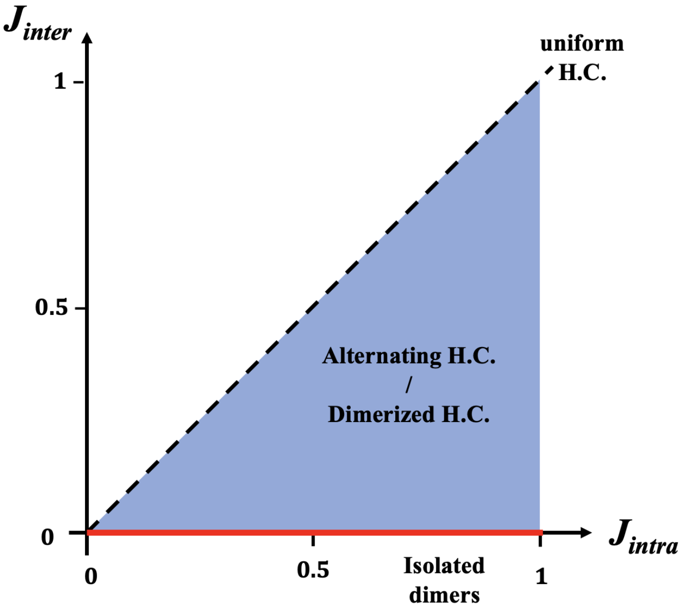

Figure 2.3: Diagram of relationship between J_{intra} and J_{inter} in the different 1D magnetic systems concerned in the thesis. HC = Heisenberg chain.

The 1D dimerized (or alternating) Heisenberg chain with spins $\vec{S_1}$ and $\vec{S_2}$ has the Hamiltonian [3]

$$\hat{H} = \sum_{i=1}^{L/2} J_{intra}\vec{S}_{2i-1} \cdot \vec{S}_{2i} + J_{inter}\vec{S}_{2i} \cdot \vec{S}_{2i+1} \tag{2.3}$$

for a chain with L ions.

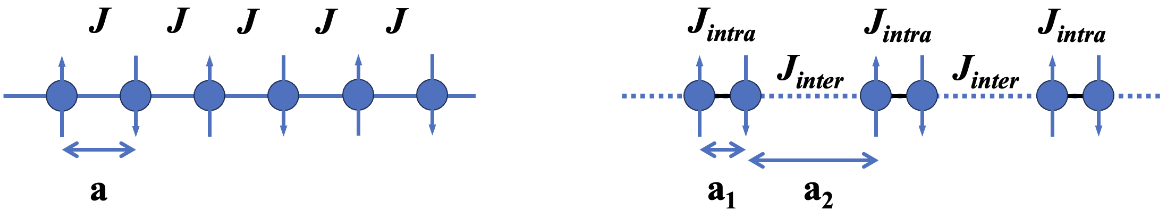

Figure 2.4: Geometry of a uniform 1D Heisenberg chain (left) and an alternating 1D Heisenberg chain (right).

The dimerization via antiferromagnetic interaction consequentially forms a singlet ground state $S = 0(|0,0\rangle)$ and a triplet of excited states $S = 1(|1,1\rangle, |1,0\rangle, |1,-1\rangle)$, whose energy level diagram is shown in Figure 2.5 a. The projection of the total magnetic moment of a spin singlet in any direction is equal to 0 whereas that of the spin triplet is equal to 1 [4]. When the Hamiltonian operator is applied on the eigenstates, the eigenvalues obtained are $-\frac{3}{4}J_0$ and $\frac{1}{4}J_0$ for the ground and excited states respectively. The difference in energy between the ground and excited states result in an energy gap in excitation spectra where is $\Delta = J_{intra}$ in case of the non-interacting dimers. In strongly magnetic fields, the degeneracy of the excited states is lifted.

The interaction between neighboring dimers result in a dispersion of the excited states. The energy width of the dispersion is equal to J_{inter} and is centered at J_{intra}.

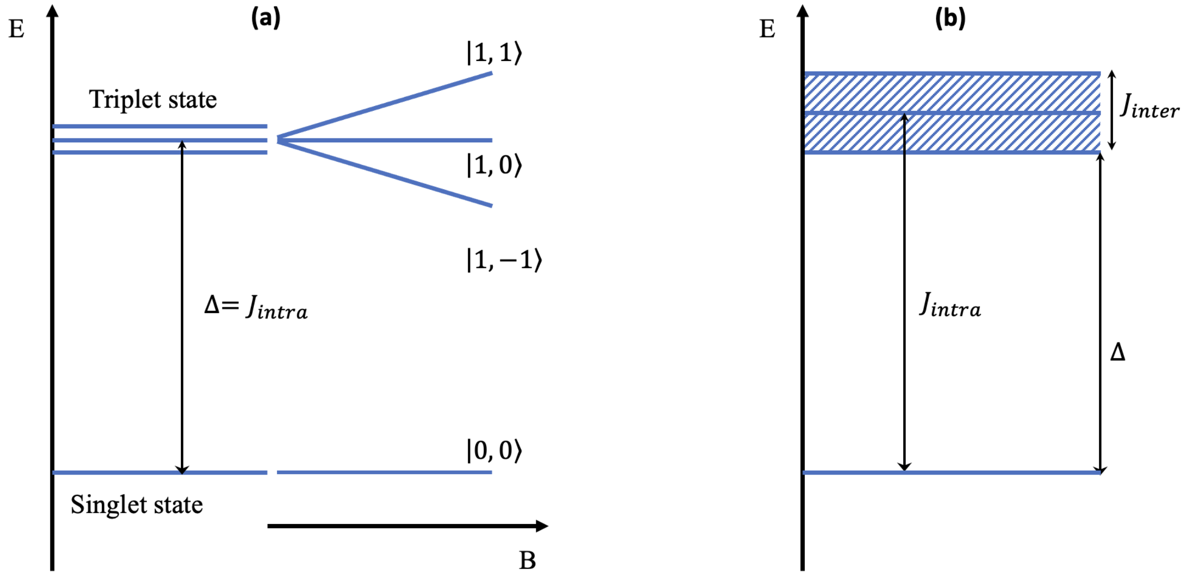

Figure 2.5: Energy level diagram of (a) an isolated spin-$\frac{1}{2}$ dimer system and (b) a weakly coupled spin-$\frac{1}{2}$ dimer system. Figure adapted from [5]

The *spin-Peierls transition* is where the uniform chain becomes dimerized under a certain transition temperature T_{SP}. Both the uniform and alternating Heisenberg models exist within the same system as the uniform chain becomes an alternating chain at temperatures below T_{SP}. The transition stems from weak magnetoelastic coupling known as spin-phonon coupling [2]. The one dimensional electronic structure along which the spins are uniform coupled to the three dimensional vibrations of the phonons. The exchange energy is directly coupled to the spacing of the pliable lattice. Very few materials exhibit a spin-Peierls transition because more rigid antiferromagnetic chains typically order in three dimensions due to the interchain spin-spin coupling being stronger than the spin-phonon coupling of the spin-Peierls transition.

The other limit of the alternating 1D Heisenberg chain are *isolated dimers* where $\alpha = 0$ and $J_{inter} = 0$. The isolated dimer pairs do not magnetically interact with other dimers and have the simple Hamiltonian:

$$\hat{H}_{dimer} = J_{intra}\vec{s}_1 \cdot \vec{s}_2 \tag{2.4}$$

The Hamiltonian of a total system of N number of isolated dimers becomes the simple sum of Hamiltonians of the individual dimers:

$$\hat{H}_{dimer} = J_{intra}\sum_{i}^{N} \vec{s}_{i1} \cdot \vec{s}_{i2} \tag{2.5}$$

The magnetic chain does not always only consist of one structural chain of magnetic ions. In many real materials with well isolated magnetic ions the exchanges with next nearest neighbors J_{NNN} also factor in to the interactions that dictate the whole system's magnetic properties. These systems that consist of two coupled chains are known as zigzag chains.

Two Dimensional Dimerized Magnets

The same kind of dimerization of nearest neighbor interactions can apply to a two-dimensional system. The dimers are arranged not in a chain but rather in a plane, forming a lattice. It has the same physics and excitations as the one dimensional dimerized system but is modified to account for more neighbors. The 2D Heisenberg dimerized magnetic system has the Hamiltonian:

$$\hat{H} = \frac{1}{2}\sum_{i} J_{intra}\vec{S}_{i,1} \cdot \vec{S}_{i,2} + \frac{1}{2}\sum_{(ij)}\sum_{\alpha,\beta} J_{inter}\vec{S}_{i\alpha} \cdot \vec{S}_{j\beta} \tag{2.6}$$

that extends the Hamiltonian of the 1D dimerized (alternating) Heisenberg chain (equation 2.3) to two dimensions.

Intermediate states between a two dimensional and a perfectly one dimensional antiferromagnetic (or ferromagnetic) state can also form as spin ladders. This arises when spin chains are spatially close enough that they can couple to form a spin ladder [4], where the spin chains form 'legs' of the ladder and dimer pair the 'rungs' of the ladder. The spin ladder's properties vary significantly between spin ladders with an even or an odd number of legs.

2.3 Macroscopic magnetic properties

The properties of low dimensional magnetic systems can be explored via their macroscopic properties. Macroscopic bulk measurements such as heat capacity, magnetization and magnetic susceptibility give experimental access to key characteristics of magnetic behaviour of quasi-low dimensional quantum magnets such as phase transitions, transition temperatures, type and strength of the magnetic exchange couplings.

The *Curie-Weiss law* describes the magnetic susceptibility of magnets in the paramagnetic region above the Curie-Weiss temperature θ_{CW}:

$$\chi = \frac{C}{T - \theta_{CW}} \tag{2.7}$$

where C is a material specific Curie constant and T is the temperature. Straight-line graphs can be obtained from plotting the inverse susceptibility versus temperature:

$$\frac{1}{\chi} = \frac{T}{C} - \frac{\theta_{CW}}{C} \tag{2.8}$$

The temperature axis intercept can be used to determine the magnetic state of the system; a ferromagnet will have a positive Curie-Weiss temperature, an antiferromagnet will have a negative Curie-Weiss temperature and a paramagnetic system will have $\theta_{CW} = 0$. For the ferromagnets, their critical temperature is known as the Curie temperature T_C where $\theta_{CW} = T_C$. For antiferromagnets, their critical temperature is known as the Néel temperature T_N where $T_N = -\theta_{CW}$ and $T_N > 0$.

Experimentally determined Weiss temperatures θ in antiferromagnets often differ significantly from $-T_N$ due to assumptions and simplifications made about the magnetization of the two sublattices [2].

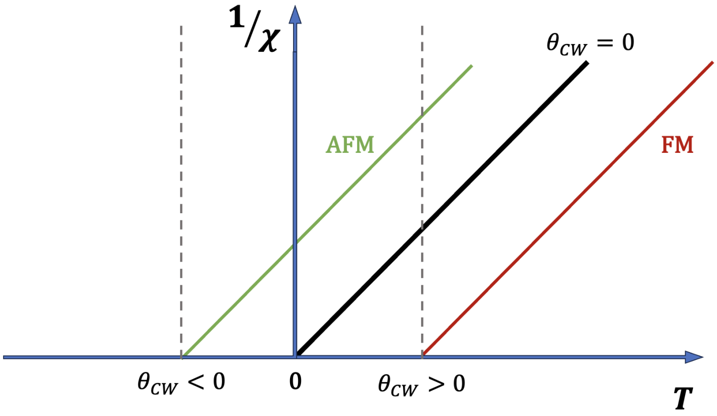

Figure 2.6: Schematic of inverse susceptibility $1/\chi$ as a function of temperature for the three types of magnetic states: antiferromagnetic (green), paramagnetic (black) and ferromagnetic (red).

There are different models to predict and describe how the bulk properties of different low dimensional systems behave. The model used to describe the magnetic susceptibility over the whole temperature range can be obtained from [6]:

$$\chi_{obs} = \chi_0 + \chi_{imp} + \chi_{dimer}. \tag{2.9}$$

χ_0 and χ_{imp} are the temperature independent term and the paramagnetic impurity contributions. χ_{dimer} depends on the dimer model for the measured system. The susceptibility for the *isolated dimer model* is given by

$$\chi_{isolated} = \frac{3C/T}{3 + \exp(J_{intra}/k_B T)} \tag{2.10}$$

where J_{intra} is the intradimer coupling constant, C is the material specific Curie constant, k_B is Boltzmann's constant and T is temperature. The susceptibility of the *weakly coupled dimer model* is

$$\chi_{w.c.} = \frac{3C/T}{3 + \exp(J_{intra}/k_BT) + J'_{inter}/k_BT} \tag{2.11}$$

where J'_{inter} is the sum of the weaker interdimer exchange J_{inter} interactions acting on each dimer.

At low temperatures, temperature independent contributions and impurities will dominate the measurable magnetic susceptibility of materials. The temperature independent contribution arises from the core diamagnetism present in all materials due to the initial repulsion electrons experience in a magnetic field [7]. The temperature independent contribution is a weak constant term, typically $\sim 10^{-5}$ cm^3/mol depending on the ions and energy gap of the sample. The paramagnetic contribution of any impurities in the sample will also dominate the magnetic susceptiblity at low temperatures.

The paramagnetic behavior of impurities at low temperatures come from defects in the crystal lattice and follow Curie-Weiss law:

$$\chi_{imp} = \frac{C_{imp}}{T - \theta_{CW,imp}} \tag{2.12}$$

The material specific Curie constant is defined as

$$C = \frac{N_A g^2 \mu_B^2 S(S+1)}{3k_B} \tag{2.13}$$

where Avogradro's constant N_A, the Landé g, the Bohr magneton μ_B, spin S and Boltzmann's constant k_B. This is true for the materials in strong crystal field environments where the orbital is quenched and $\boldsymbol{J} = \boldsymbol{S}$.

Chapter 3

Experimental Methods

This chapter contains detailed information about the different experimental methods used in the thesis. When necessary, some theory will be provided before sharing the procedures for the specific technique. The order is based on the preparation and characterization order of the investigated compounds.

The first part explains how polycrystalline samples of four different compounds, $SrCuO_2$, $CuGeO_3$, $BaCuSi_2O_6$ and $BaCu_2V_2O_8$, were grown using solid state synthesis.

Characterization of all synthesized samples was performed using Powder X-Ray Diffraction (PXRD) and the analysis of successful crystal growth of the desired compounds was completed using Rietveld analysis. The quality of the samples were controlled by powder X-ray diffraction measurements.

Due to the presence of unidentified impurities from the synthesis of $BaCu_2V_2O_8$, further characterization of the powder sample was performed using X-ray spectroscopical techniques. The X-ray Photoelectron Spectroscopy (XPS) and X-ray Absorption Spectroscopy (XAS) measurements of $BaCu_2V_2O_8$ were performed at the SPECIES-beamline at MAX IV.

The main goal of this research is to investigate the effects of hydrostatic pressure on magnetic properties of these four different compounds using thermodynamic measurements. This was done through constant-field susceptibility measurements that were performed for $BaCuSi_2O_6$ and $BaCu_2V_2O_8$. Both compounds were measured in ambient pressure and with applied pressure.

3.1 Solid State Synthesis

All polycrystalline samples of $BaCuSi_2O_6$, $BaCu_2V_2O_8$, $SrCuO_2$ and $CuGeO_3$ studied in this work were synthesized by standard solid-state reactions. The conditions used were obtained from previously published articles [8–11]. The synthesis of $BaCu_2V_2O_8$, $BaCuSi_2O_6$ and $SrCuO_2$ was done at the Centre for Analysis and Synthesis (CAS) at Lund University while $CuGeO_3$ was synthesized at Helmholtz-Zentrum Berlin (HZB) in collaboration with Dr. Nazmul Islam due to the need for a furnace supplied with oxygen flow.

The synthesis using solid-state reactions entailed mixing precursors in stochiometric ratios with a small amount of ethanol and heating in high temperatures with intermediate grinding. Intermediate grindings of the products were conducted to increase the homogeneity of the precursor mixture and to ensure complete reaction of the reactants, which should reduce the amount of impurity phases [12]. Detailed reactions for the four compounds are given in the related sections in chapter 4.

At CAS the samples were sintered in *alumina* crucibles in a muffle furnace. At HZB, the $CuGeO_3$ sample was sintered in an *alumina* crucible in a tube furnace supplied with a steady flow of oxygen.

The samples were pelletized in preparation for magnetometer measurements under pressure. A hydraulic press was used to apply $\sim$ 1 ton of pressure for 10 minutes. The die had a diameter of 13 mm and the thickness of the pellets varied between 3 to 7 mm depending on the amount of sample pressed together.

3.1.1 Single Crystal Growth

In addition, a single crystal sample of $BaCu_2V_2O_8$ was available for this project. This single crystal was grown using the travelling-solvent floating zone (TSFZ) technique in Helmholtz-Zentrum Berlin by Dr. N. Islam[11].

After obtaining a pure single phase of polycrystalline powder, a single crystal can be grown using this powder. The principle behind the travelling-solvent floating zone crystallization method is shown in Figure 3.1. Tungsten halide lamps are used to melt a part of the solid feed rod [13]. A seed rod is placed in contact with one end of the feed rod. The lamp-assisted heating forms a point with molten solvent with two solid-liquid interfaces, one between the melt and the feed rod and one between the melt and the seed rod. The lamps proceed to move, translating the molten zone along the feed rod. As it moves away from the seed rod, the melt at the seed-melt interface freezes and crystallizes as a large single crystal.

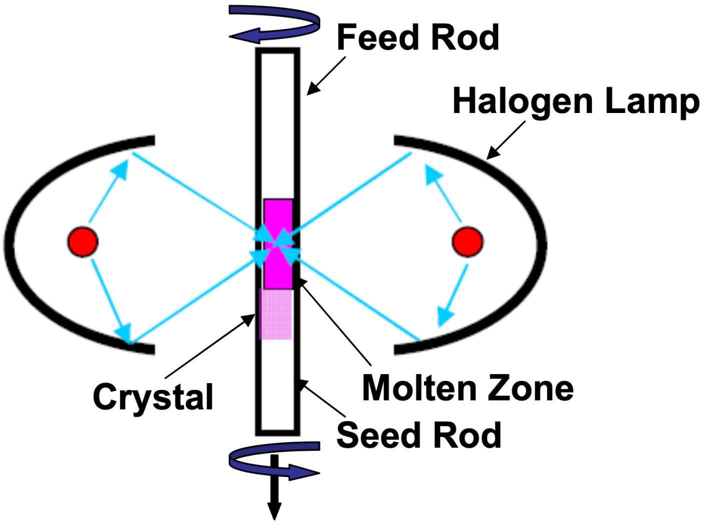

Figure 3.1: Schematic of the traveling-solvent-floating-zone furnace. Figure taken with permission from [1].

3.2 X-Ray Diffraction

Diffraction techniques provide very powerful and direct tools to investigate a material's crystal structure and X-ray diffraction is the most commonly used and accessible laboratory technique. In this work X-ray diffraction was used to check the quality of the powder samples after crystal growth.

The technique is based on the conventional diffraction principles which are governed by the Bragg Law. When plane waves are incident on a crystal lattice under angle θ where they are reflected from the successive parallel crystal planes of spacing d. The reflected waves interfere constructively if the Bragg condition $2d\sin\theta = n\lambda$ is satisfied, where any integer n and the wavelength of the incident light λ is equal to the path difference between the reflected beams. The different planes are characterized by different interplanar distances in the crystal structure. Therefore for the fixed wavelength of the incident beam the Bragg condition will be satisfied at different angles, generating unique diffraction pattern for different particular crystal structures.

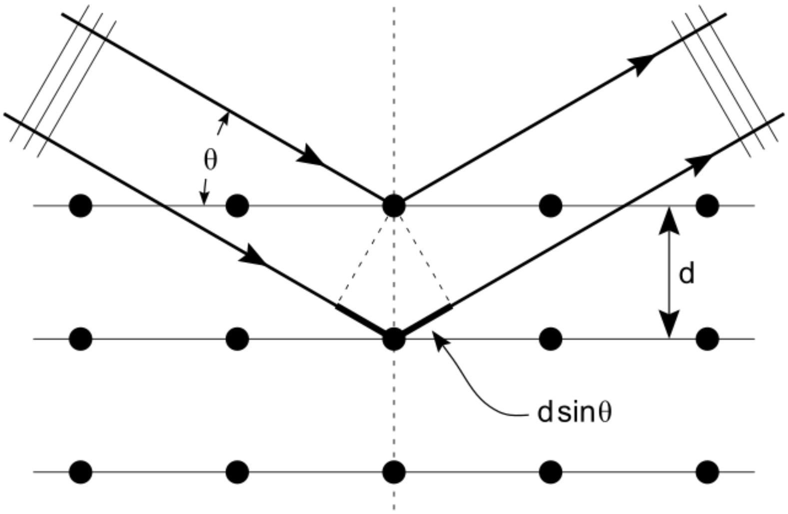

Figure 3.2: Bragg diffraction from a cubic crystal lattice. Plane waves incident on a crystal lattice at angle θ are partially reflected by successive parallel crystal planes of spacing d. The superposed reflected waves interfere constructively if the Bragg condition $2d\sin\theta = n\lambda$ is satisfied (Image attributed to Hydrargyrum at English Wikipedia, CC BY-SA 3.0)

Powder X-Ray Diffraction (XRD) can provide important information about the crystal phases present and the sample purity when the measured diffraction pattern is compared with calculated or previously reported patterns for that compound's crystal structure. PXRD measurements are considered a bulk characterization technique and therefore provide an average observation on the sample as opposed to single-crystal XRD that look at a limited area.

The powder X-ray diffractometer uses an X-ray source, a sample stage and a detector. The set up requires the ability to vary the angle θ between the source and the sample while the detector rotates around the sample to record the intensity of reflected X-rays at angles of 2θ from the source. The X-ray source can be either set up in transmission mode or reflection mode. Different samples suit different geometries. To ensure a better statistical average of the sample is recorded for PXRD, the sample stage can rotate at an angle perpendicular to the sample plane.

X-ray diffractometers can use different X-ray sources. Synchrotrons and X-ray tubes can both be used but X-ray tubes are commercially available and therefore accessible in laboratory environments. Both source types are based on the acceleration of electrons. For the X-ray tube, a high voltage is applied between a tungsten cathode and a metal target anode in vacuum. The tungsten cathode is heated, producing free electrons that accelerate towards the anode due to the potential applied across the tube. When the accelerated electrons hit the metal target core electrons are knocked out and electrons in the outer orbitals drop down to fill the vacancies. This relaxation process emits the X-rays of the source. The metal target must be cooled due to the large heat production of the process. The choice of metal determines the source's wavelength because of the different energies associated with the atomic transitions for different metals. Copper is a commonly used X-ray source with well known transitions. There are typically multiple intense transitions for a metal; copper has a Cu K_α and a Cu K_β transition. The wavelength for the Cu K_β transition can be removed used a filter. The Cu K_α X-ray is not monochromatic due to fine-structure splitting but modern X-ray devices use a crystal monochromator to eliminate one of the signals. This produces a monochromatic Cu $K_{\alpha1}$ X-ray beam with wavelength $\lambda = 1.54056$ Å.

The diffraction techniques based on neutrons or electrons mentioned at the beginning of the section function similarly but can provide additional information. Electron diffraction methods such as transmission electron microscopy (TEM) and low energy electron diffraction (LEED) can record reciprocal space patterns of crystals and be used to understand the real space arrangement of crystals. Neutron diffraction and scattering can provide more information of samples. Neutrons are diffracted by the nucleus of atoms and can thereby provide more information on materials as even one element's isotopes have distinctly different characteristics. Neutrons have a spin and can therefore interact with the magnetic moments of an atom's electron cloud, providing insight on the microscopic magnetic structure of materials. This is typically used to confirm the excitation spectra of magnetic materials definitively after predictions of magnetic interactions from initial thermodynamic measurements.

The X-ray diffraction measurements were performed using the STOE STADI MP diffractometer available at CAS, Lund University. Measurements were performed in transmission mode at room temperature using Cu $\mathrm{K}_{\alpha1}$ $\lambda = 1.54056$ Å. The Cu $\mathrm{K}_{\alpha2}$ was filtered and do not contribute to the diffraction pattern. The collected data were refined using FullProf software [14]. The initial parameters of the crystal structures of desired compounds and the impurity phases were taken from the Inorganic Crystal Structure Database (ICSD) [15], the American Mineralogist Crystal Structure Database (AMCSD) [16] and literature. The lattice parameters and atomic positions of all phases were then varied during the refinement routing. The references for the different Crystallographic Information File (CIF) will be reported together with the respective crystal phase in the later paragraph. All diffractograms were partially affected by the use of adhesive tape (810 adhesive Scotch tape) to mount the samples. It results in the increasing of the background at lower 2θ angles and results in a slight slope of the background at angles lower than 30°. This adhesive is supposed to have the lowest background [17].

3.2.1 Rietveld Refinement

In a diffractogram, multiple peaks emerge among some background. The background arises from scattering in the sample holder, air or from the experimental setup. The peaks are characterized by their position, intensity and shape and can gain detailed information about the sample's structure. The peak's position at a particular angle 2θ depend on the unit cell and crystal space group of the sample whereas the intensity depend on the exact atomic positions of elements in the unit cell and the elemental composition of the sample. Typically described by Gaussian, Lorentzian, or pseudo-Voigt functions, peak shapes result from the convolution of various factors, including instrumental contributions and structural effects from the sample.

While an ideal, defect-free, single phase sample would yield delta-function peaks, real-world samples exhibit broadened peaks due to finite-sized crystallites, crystal boundaries, dislocations, instrumental effects and imperfections affecting atomic displacements in lattice planes. Precise analysis of a diffractogram can offer detailed qualitative and quantitative insight into the sample's structure. Various methods and programs, such as the Rietveld refinement method, simplify this process. Rietveld refinement allows the fit of a structural model, obtained from theoretical models or previously published data, to the observed data via varying selected parameters of the model. Instrumental parameters, peak shape functions and atomic positions are varied to obtain the best fit of observed peak positions, shapes, and intensities. A successful refinement unveils information on the sample's structure, crystallite size, and much more. Rietveld refinement is based on a least-squares fitting of the model to the observed data.

The obtained diffraction patterns were analyzed using Rietveld refinement in FullProf Suite to determine the unit cell dimensions and phase purity of the samples. The calculated diffraction models for all compounds were obtained from CIF available through different crystallographic databases. The peak shapes were described by the pseudo-Voigt function as implemented in FullProf, which were then fitted to the observed peaks [17]. Following FullProf procedures, background was first determined and subtracted from the observed data. In the following order, different parameters were allowed to vary to improve the fit of calculated models to the observed data: scale factor, instrumental zero point, lattice constants and atomic positions. High sample purity is indicated by good agreement between calculated model and observed data. The presence of unexpected peaks when fit with only one crystal model indicates the presence of impurity phases.

3.3 Characterization via Spectroscopic techniques

3.3.1 X-ray Photoelectron Spectroscopy

XPS is commonly used to analyse the chemical composition of surfaces. It is based on the concept behind the photoelectric effect and provides information on both the chemical and the electronic state of the investigated atoms.

The technique involves irradiating the sample with photons of a certain energy $h\nu$. The atoms on the surface absorb the energy of the photon into its core-level electrons and later emits photoelectrons to compensate for the absorbed photon energy as dictated by the law of energy conservation. The electron's energy consists of binding energy E_B and work function Φ to be emitted from the surface. The last component of the electron's energy is its measurable kinetic energy E_K.

$$h\nu = E_B + \Phi + E_K \tag{3.1}$$

X-ray photoelectron spectroscopy (XPS) is a surface sensitive technique due to the emission of electrons only taking place in the topmost layers of the sample. This is due to the short inelastic mean free path of electrons in solid materials. As a consequence of this, different depths between 5 and 50 Å of the sample surface can be probed by using different photon excitation energies between 200 and 2000 eV [18]. The inelastic mean free path varies slightly for different elements and solid compounds but they all follow a universal curve. Although X-rays can penetrate further into the sample, the emission of electrons only take place on the surface.

The XP spectra show the measured intensity of photoelectrons as a function of kinetic energy E_K or binding energy E_B. The different chemical environments that the atoms are in can be deduced by comparing the differences in binding energy of the sample to references either from literature or by taking measurements of known samples. These differences in binding energy are known as chemical shifts and provide information on the different chemical states of the atom that absorbed the photon into its core level.

The composition of the sample, i.e. the atomic percentage, can be calculated in a straightforward manner from the peaks. This is under the assumption that the sample is homogeneous and single phase within the sampling depth. By dividing the area of an element's peak I by a sensitivity factor S, a normalized peak area is obtained. The atomic fraction is this normalized peak area I/S divided by the sum of the normalized peak areas, which in turn can be multiplied by 100% for atomic percentage. The sensitivity factor is determined by the different settings of the instruments and which orbital the peak is from. [19]

XPS lines for all transitions, except those for the s-orbitals, manifest as doublets due to spin-orbit splitting. The intensities of the doublets are related as a ratio depending on the identity of the concerned orbital. A p-orbital splits into $p_{1/2}$ and $p_{3/2}$ peaks of intensity ratio 1:2 whereas a d-orbital splits into $d_{3/2}$ and $d_{5/2}$ peaks of intensity ratio 2:3. [20]

Static charging takes place when a non-conducting sample is irradiated. Positive charge builds up and creates a field on the surface. This increases the energy the emitted electron must have before it can be emitted, thus causing a shift in the measured energy of the electron.

3.3.2 X-ray Absorption Spectroscopy

X-ray absorption spectroscopy (XAS) also involves exciting a core-level electron but results in a transition of the core-level electron to an unoccupied state in the conduction band. The Near-Edge X-ray Absorption Fine Structure (NEXAFS) measurements investigate the spectral region of energies just below the absorption edge whereas Extended X-ray Absorption Fine Structure (EXAFS) spectra covers the energies above the absorption edge. The absorption edge is defined as the energy where there is a sharp discontinuity in the absorption spectrum of an element. This occurs when the energy of the absorbed photons corresponds to the electronic transition energy. Figure 3.3 shows an overview of the edges and the corresponding atomic subshells that the electron transitions from.

NEXAFS is a highly surface sensitive technique from which information on the oxidation state of the atoms can be obtained. This is because the conduction band is perturbed by the neighboring atoms that the absorbing atom is bonded to and in what combination they are bonded. The photoelectron from the absorbing atom is scattered because of the neighboring atoms' electrons. This creates spectral “fingerprints” that are unique to different local bonding environments that can be used to compare and identify the bonding environment of the investigated sample.

Certain transitions are forbidden because of the selection rules for electric dipole transitions. They are as following [21]:

- The change in the total angular momentum $\Delta j = \pm 1$
- The change in the orbital anglar momentum $\Delta l = \pm 1$
- The change in the spin angular momentum $\Delta s = 0$

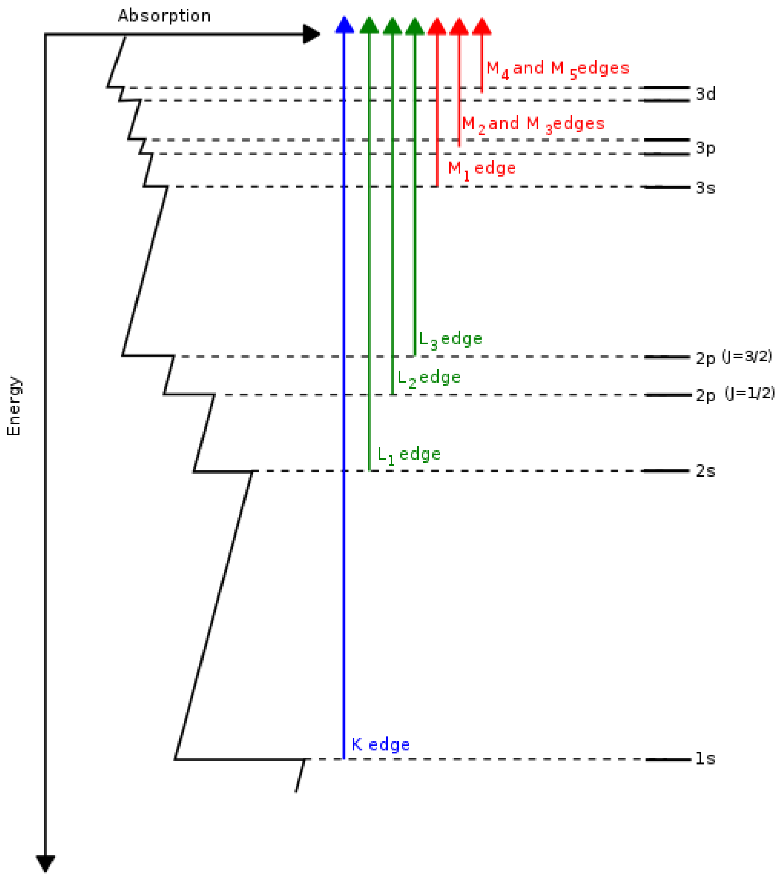

Figure 3.3: Diagram showing which transitions contribute to X-ray absorption edges (Image attributed to Atenderholt, CC BY-SA 3.0, via Wikimedia Commons)

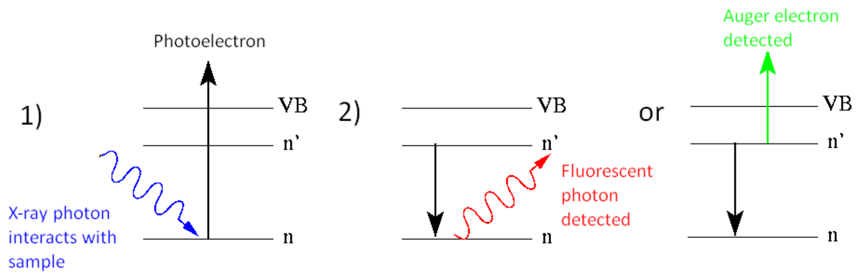

Figure 3.4: Diagram showing photoelectron emission and the two alternatives to filling the core hole by either fluorescence or emission of Auger electrons. (Image attributed to Alison Chaiken (wikimedia commons: Chaiken); Modified by GoddersUK, CC BY-SA 3.0, via Wikimedia Commons)

XAS techniques can be broken down to four modes that measure either the fluorescent photons or the Auger electrons. Compared to XPS measurements which have a fixed photon energy and electron intensity is recorded as a function of electron kinetic energy, XAS scans the photon energy and records the intensity of absorbed x-rays via detecting the number of fluorescent photons or Auger electrons. Absorption detection can be performed by four different modes: total electron yield, partial (Auger) electron yield, fluorescence yield and transmission mode. The first two techniques detect electrons whereas the latter two detect photons. The different modes are suitable for probing at different sample depths because of the different ways matter and electrons or photons interact. Total and partial electron yield analyze the number of the emitted electron as a function of photon energy. The difference between them lie in the range of energies that are detected; total electron yield measure electrons of all energies whereas partial electron yield only measures the electrons with a kinetic energy above a certain threshold. A third distinction can be made for partial Auger electron yield that measures in a smaller window of energies and is centered around the Auger peak. Fluorescence yield detects the emitted fluorescent signal from a thin adsorbate layer of the substrate. Transmission mode calculates absorption based on the logarithmic ratio between the intensity of incoming X-rays and the detected intensity of X-ray photons that have passed through the sample [22].

3.3.3 The SPECIES-beamline at MAX IV

The XPS and NEXAFS experiments were conducted at the ambient pressure (AP)-XPS branch of SPECIES beamline at MAX IV laboratory in Lund, Sweden [23].

The energy range of the X-rays available at the SPECIES-beamline is between 30 eV to 1 500 eV. The FWHM beam size in the APXPS end-station measure 100 × 100 µm. The detector and X-ray beam set at the magic angle (54.7%). This renders the orbitals' asymmetry factors' contribution to the instrument's sensitivity factor S uniform for all peaks [24].

The photon flux of the APXPS end-station varies with photon energy. The behavior of this variation can be seen in the appendix.

3.4 Characterization with a Magnetometer

The samples' magnetic properties were measured and characterized at the Advanced Materials Characterisation Facility at the University of Birmingham in collaboration with Dr. Mingee Chung, Dr. Matthew Coak and Dr. Aly Abdeldaim from the Condensed Matter Group.

The first part of this section provides the reader with a brief overview of how the equipment functions and its set up. The second part details how the measurements of samples in ambient pressure were prepared while the third part details how the measurements under applied pressure were prepared. The last part provides the reader with information on how to treat raw data with weak magnetic signals to extract useful data for those measurements.

3.4.1 Magnetometer set up

Magnetic susceptibility measurements are useful in extracting information about a system's magnetic properties as they reveal how the material system responds to an applied magnetic field. The magnetic susceptibility χ relates the system's magnetic moment $\boldsymbol{M}$

that is induced by applying a magnetic field $\boldsymbol{H}$ to the system via $\mathbf{M} = \chi\mathbf{H}$ [7]. Magnetic measurements can be performed by applying either a direct current (DC) or a alternating current (AC) magnetic field and taking measurements at different temperatures. Applying a DC field probes the properties of the material under equilibrium conditions whereas applying a time-variant AC field probes the material's dynamics. Analysing magnetic susceptibility data as a function of temperature provides access to the sign and magnitude of magnetic exchange interactions.

The magnetic susceptibility measurements relevant for this thesis are traditional DC scans using a Superconducting Quantum Interference Device (SQUID). The one used was a MPMS3 from Quantum Design. The SQUID magnetometer uses two parallel Josephson junctions to form a superconducting loop that can detect magnetic fields and magnetic flux with high sensitivity. A second order gradiometer, also known as a pick-up coil, is inductively coupled to the SQUID [25]. As the sample is scanned through the gradiometer, screening currents are generated through the mechanical movement. This happens due to the movement of the sample generating a magnetic flux that interrupts the superconducting loop of the SQUID [26]. The screening current is the applied bias current necessary to re-establish the superconducting loop. This current is converted into to a voltage and a spatially dependent voltage waveform is generated, see figure 3.5. From the voltage waveform, determination of the sample's placement in the sample holder can be obtained and the magnetic moment of the sample can be calculated.

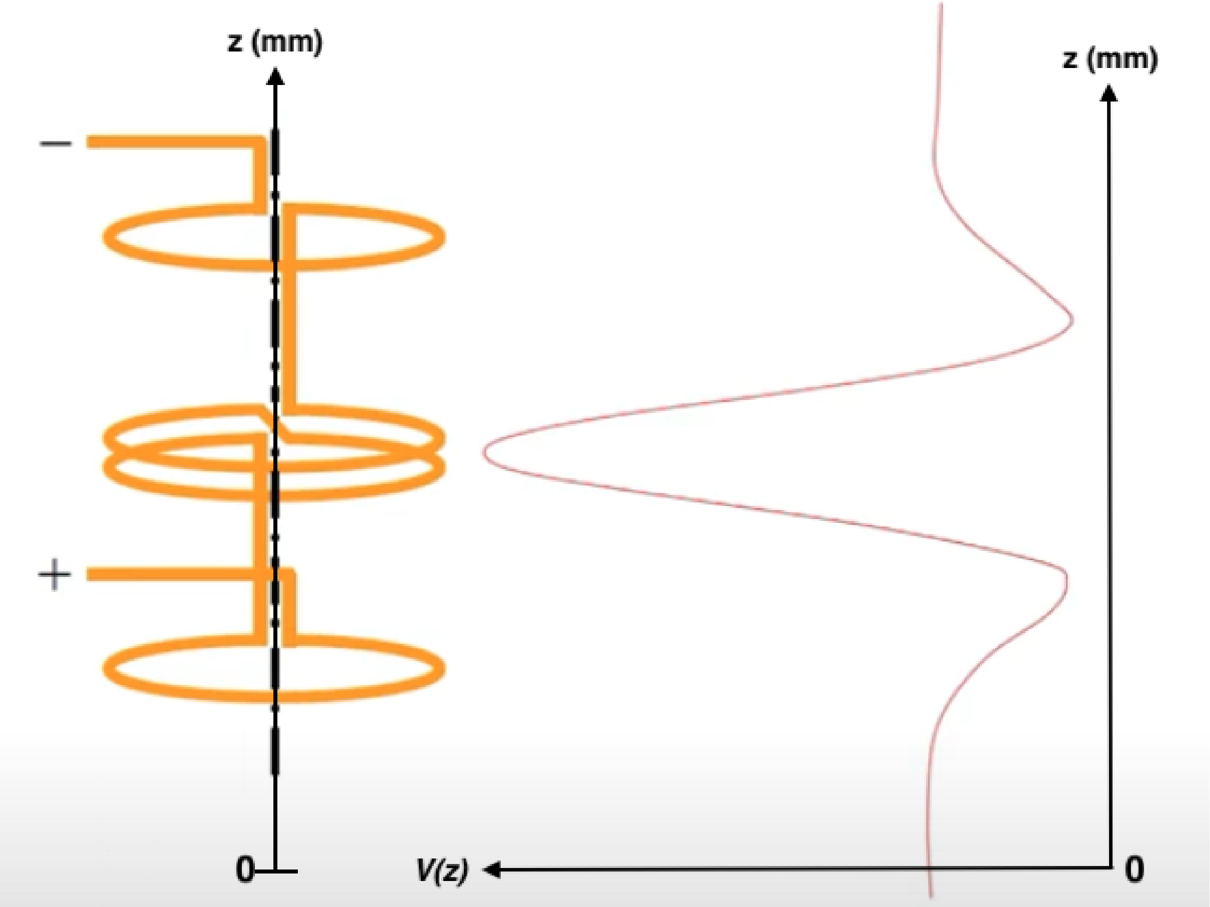

Figure 3.5: Schematic of the gradiometer (in yellow, on the left) and of the voltage waveform (on the right). The gradiometer's two poles are connected to a SQUID. The SQUID detects the change in magnetic flux from the movement of the sample inside the gradiometer, producing a voltage proportional to the change in magnetic flux caused by the sample. This can then be mapped for voltage as a function of the sample's position z along the scan-axis, i.e. a spatially dependent voltage waveform. Figure taken and adapted from Quantum Design [25]

The MPMS3 machine is equipped with MultiVu software that automatically fits this voltage waveform to calculate the magnetic moment of the sample. The software assumes that the sample can be modeled as a small point-like dipole for its calculation of the magnetic moment. This makes the automatic fitting of the magnetic moment of spatially extended samples problematic at times as the sample cannot be approximated to a point. Automatic fitting of the magnetic moment in the MPMS3 can also be inappropriately fit if the sample's magnetic moment is too small relative to the background or if there are magnetic impurities present on the sample holder. This fit can be performed in two ways, either by assuming the sample has a fixed position in the center or by assuming a free center [26]. The fixed center mode only fits the amplitude of voltage waveform with the magnetic moment of the assumed point whereas the free center mode fits the sample position together with the amplitude.

The direction of the applied magnetic field relative to the crystallographic orientation of the systems can have varying effects on the susceptibility measured in a single crystal sample. This is dependent on whether the single crystal's magnetic moment is isotropic or anisotropic. Polycrystalline samples have no particular crystallographic orientation and therefore the measured susceptibility will be averaged over the whole sample.

3.4.2 Measurements in ambient pressure

The samples were prepared for magnetometer measurements by manually grinding the polycrystalline sample. The powder was placed between two layers of parafilm in polycarbonate capsules centered in the straw sample holder. The samples were zero field cooled at 12 K per minute until they reached base temperature. A magnetic field of 1 T was applied before measurements were taken. The measurements of DC moments were taken continuously from 1.9 K to 300 K with a sweep rate of 2 K per minute.

3.4.3 Measurements under applied pressure

Samples were placed inside a pressure cell to record their magnetic properties under pressure. For measurements under applied pressure, pelletized polycrystalline samples or single crystal samples are required. A schematic of a pressure cell compatible with the MPMS3 magnetometer can be seen in figure 3.6. The pelletized sample was placed inside a teflon tube. A tin pressure reference (manometer) was placed inside the tube before the tube was placed inside the pressure cell. The teflon tube was then filled with the pressure transmitting medium Daphne Oil 7373. Teflon caps were placed at both ends of the tube to seal the sample region. The teflon tube was centered in the center cylinder before pistons were placed on either ends of the cylinder. Teflon powder was applied to the pistons before the piston backups, side cylinders and the cylinder pressurization nut were assembled. The gap between the pressurization nut and the side cylinders were equally big prior to pressurization.

To apply and determine the pressure on the sample, the pressurization nuts on the cell were tightened manually with spanners to compress the cell and measurements of the reference tin were performed prior to susceptibility measurements. The compression of the cell was indicative of the approximate applied pressure as given by the manual for the pressure cell provided by Quantum Design. The definitive pressure of the cell was determined by a sweep of the magnetic DC moment in a region around the manometer's superconducting temperature. The shift of tin's superconducting transition temperature within this temperature range was used together with an equation from the pressure cell's manual to determine the applied pressure. The temperature range was from 3.2 K to 3.8 K for the tin manometer. A field of 1 Oe is sufficient for the reference measurement.

If the pressure cell is assembled incorrectly or if an air bubble has formed within the Teflon tube, the applied pressure of the cell will vary and other potential magnetic impurities could be introduced to the measurement region.

The samples were zero field cooled at 5 K per minute from 300 K to 10 K and then cooled at a rate of 1 K per minute until were reached 1.9 K. Temperature changes must be slower when the equipment is under pressure to ensure the safety of users and the equipment. A magnetic field of 1 T was applied before measurements were taken. The measurements of DC moments were taken continuously from 1.9 K to 300 K with a sweep rate of 0.8 K per minute.

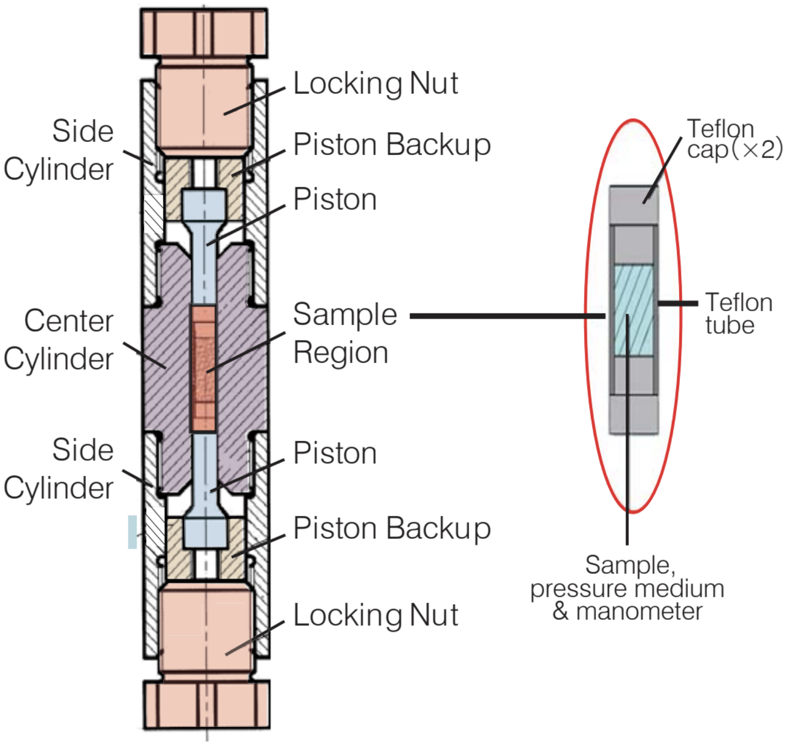

Figure 3.6: Schematic of the pressure cell. Figure taken from Quantum Design [27]

3.4.4 Manual fitting using SquidLab

For certain measurements the MultiVu software provided by Quantum Design to fit the measured waveform will not be well-fit by the response function. This could happen when the magnetic moment is relatively small compared to the background, which is likely to happen for measurements performed on samples with a small magnetic moment in a pressure cell. Manual fitting of the samples' voltage waveform can be performed using the open-source program SquidLab [28].

SquidLab is a useful tool for background subtraction and fitting of the voltage waveform to more accurately obtain the magnetic moment of the sample. After measurement of the sample is completed, the pressure cell is to be set up with the same conditions, with respect to manometer, pressure medium and cell length, without the sample. The same measurement should then be performed to obtain a background measurement. The voltage waveform of the background can thus be obtained and after subtraction from the sample's background the magnetic moment of the sample can be obtained.

Chapter 4

Results and Discussion

This chapter presents further details on the four compounds investigated in the thesis; $BaCuSi_2O_6$, $BaCu_2V_2O_8$, $SrCuO_2$ and $CuGeO_3$. Each respective section starts by providing an overview of the established knowledge available from literature on the compound's crystal and magnetic models. This is followed by a section describing the synthesis procedure of the compound and their characterization using powder x-ray diffraction. The polycrystalline $BaCu_2V_2O_8$ sample was further characterized via spectroscopic techniques. Finally, the two compounds $BaCuSi_2O_6$ and $BaCu_2V_2O_8$ were selected for further magnetic measurements. These subchapters contain sections detailing the measurement of the magnetic susceptibility and analysis taken in ambient pressure and under applied pressure when possible.

4.1 Barium copper silicate $BaCuSi_2O_6$

4.1.1 Overview

$BaCuSi_2O_6$ is the realization of a quasi-two-dimensional dimerized system investigated in this thesis. In room temperature its crystal structure is tetragonally body-centered, as shown in Figure 4.1 with Cu-Cu distances marked. It is defined by space group $I4_1/acd$ with lattice parameters $a = b = 9.97$ Å and $c = 22.30$ Å [10]. In this structure, Ba atoms separate the staggered copper silicate $Cu_2(SiO_3)_4$ bilayers. These copper silicate bilayers comprise two layers of square planar CuO_4 plates containing the Cu^{2+} magnetic ions with spin $\frac{1}{2}$. The CuO_4 plates are joined in the edges via SiO_4 tetrahedra. The Cu^{2+} magnetic ions in vertical pairs of CuO_4 plates are bounded by the antiferromagnetic exchange interaction J_{intra} forming the magnetic dimers within the $Cu_2(SiO_3)_4$ bilayers as they lie parallel to another in the (001) crystallographic plane.

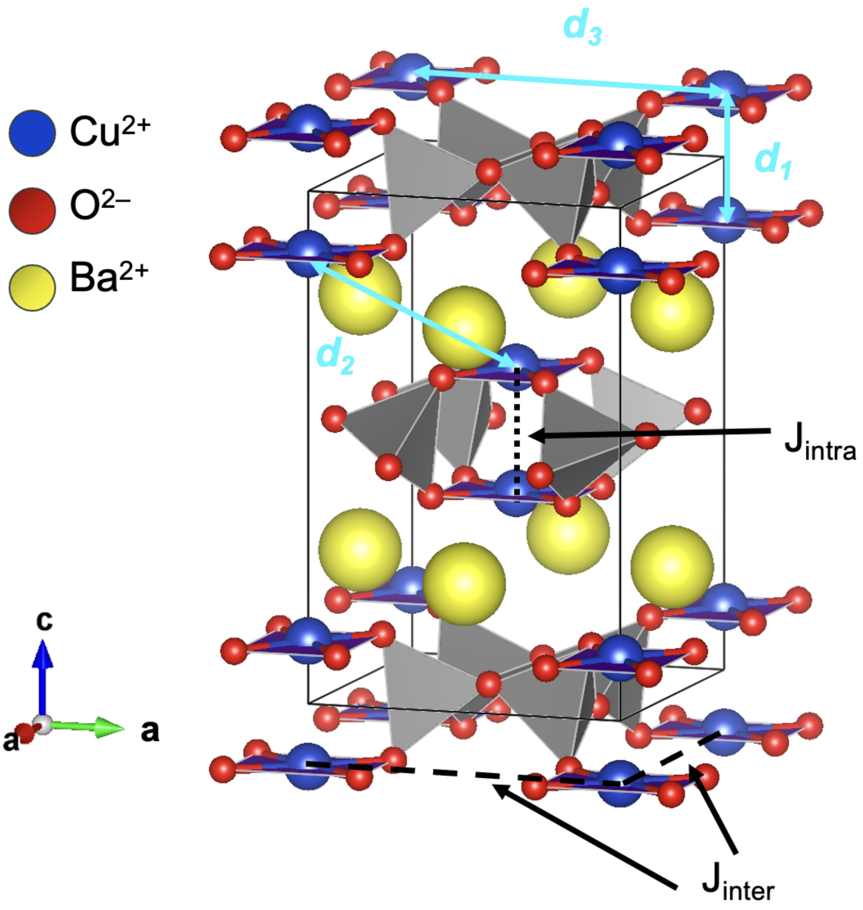

Figure 4.1: The crystal structure of $BaCuSi_2O_6$

At room temperature the intradimer Cu-Cu distance ($d_1 = 2.72$ Å) inside $Cu_2(SiO_3)_4$ bilayer is significantly shorter than the interdimer Cu-Cu distance within the single layer ($d_3 \sim 7$ Å) as well as interlayer Cu-Cu dimer distance ($d_2 \sim 5.75$ Å) [29, 30].

The vertical Cu^{2+} dimers placed on a square lattice plane within each $Cu_2(SiO_3)_4$ layer. These square lattice layers are vertically staggered, as shown in Figure 4.1 where J_{intra} is the intradimer Heisenberg AFM coupling constant and J_{inter} is the weaker interdimer coupling constant between nearest-neighbors within the same plane. A third, weaker AFM coupling J_{layer} between dimers on adjacent $Cu_2(SiO_3)_4$ layers has been found in $BaCuSi_2O_6$. It is neglectably weaker than both J_{intra} and J_{inter} and estimated to be $\sim 0.2 J_{inter}$ [5] thus will be neglected in the analysis of this thesis.

The magnetic properties of $BaCuSi_2O_6$ can be described by the following Hamiltonian:

$$\hat{H} = \sum_i J_{intra} \vec{S}_{i,1} \cdot \vec{S}_{i,2} + \sum_{(ij)} \sum_{\alpha,\beta} J_{inter} \vec{S}_{i\alpha} \cdot \vec{S}_{j\beta} \tag{4.1}$$

Here J_{intra} is the intradimer AFM coupling constant that binds the spins into the dimer, i is the index of the dimer site and $\vec{S}_{i,1}$ and $\vec{S}_{i,2}$ are the two spins forming the dimer at site i, (ij) are the nearest neighbors within the same plane whereas α and β label distinguish layers within $Cu_2(SiO_3)_4$ bilayers. J_{inter} is the magnetic exchange coupling between the dimers.

The intra- and interdimer exchange interactions in the Hamiltonian of $BaCuSi_2O_6$ at ambient pressure have been studied using different techniques by a few separate research groups. Early inelastic neutron scattering measurements performed on $BaCuSi_2O_6$ by Sasago *et al.* estimated $J_{intra} = 4.5$ meV when it was still hypothesized to be an isolated dimer [31]. Jaime *et al.* [5] estimated the intradimer and interdimer exchanges to $J_{intra} = 4.45$ meV and $J_{inter} = 0.58$ meV, respectively, from the analysis of the magnetic susceptibility of $BaCuSi_2O_6$ extracted as $\chi = dM/dH$ from high magnetic field magnetization measurements. These susceptibility values were complemented with Monte-Carlo simulations performed for the system's effective Hamiltonian.

Most recently, the intra-dimer and inter-dimer exchange interactions have been found to be $J_{intra} = 4.45$ meV and $J_{inter} = 0.51$ meV respectively by Sebastian *et al.* [30, 32] via experimentally mapping the phase boundary of $BaCuSi_2O_6$ using magnetic torque, magnetocaloric effect, specific heat measurements and Monte-Carlo simulations [30].

The gap in the magnetic excitation spectra was found to be $\Delta = 4.5$ meV [31]. No transition for magnetic long range order has been observed for $BaCuSi_2O_6$.

The g-factor for $BaCuSi_2O_6$ was determined experimentally via electron spin resonance measurements to be $g_c = 2.31$ and $g_{ab} = 2.03$ for the two crystal orientations [30].

$BaCuSi_2O_6$ first attracted attention as a material that undergoes Bose-Einstein condensation at low temperatures in high magnetic fields where $H > 23$ T [32]. Investigation of the magnetic properties under applied magnetic field is beyond the scope of this thesis but interested readers can look for the details in Reference [30].

In this thesis we will explore pressure effects on the magnetic properties of $BaCuSi_2O_6$. The effects of pressure on the crystal structure of $BaCuSi_2O_6$ have been studied for pressures up to 30 GPa [33]. The lattice parameters a and c decrease steadily with increased pressure. The pressure-induced structural phase transition in $BaCuSi_2O_6$ occurs at 15 GPa, where the coordination geometry of the Cu^{2+} ions changes from square-planar to tetrahedral. Note that this transition takes place outside the range of pressure investigated in this project.

In this thesis, we are focused on the investigation of the effects of pressure on the strength of the magnetic exchange interactions in $BaCuSi_2O_6$.

4.1.2 Synthesis

The powder sample of $BaCuSi_2O_6$ was synthesized using the solid state reaction

$$BaCO_3 + CuO + 2\,SiO_2 \longrightarrow BaCuSi_2O_6 + \uparrow CO_2 \tag{4.2}$$

The precursors $BaCO_3$ (99.95% Thermo Fisher Scientific), CuO (99.9995% Thermo Fisher Scientific) and SiO_2 (99.95% Thermo Fisher Scientific) were mixed in a stochiometric 1:1:2 molar ratio with 3.9467g, 1.5909g and 2.4033g, respectively, to obtain 6.1 g of $BaCuSi_2O_6$ powder [10]. The precursors were mixed in a small amount of ethanol and then sintered in an AL23 alumina crucible at 1035°C for 300 h total with intermediate grindings after 30 h, 60 h, 100 h, 130 h, 160 h, 210 h and 240 h, respectively. Every sintering process was heated and cooled at 175°C per hour. The sintering temperature of 1035°C was chosen to reduce amount of the impurity phases, as the choice of sintering temperature has a large effect on the phase formation of $BaCuSi_2O_6$ as found by van Well *et al.* [10]. It was found that 1035°C is the optimal temperature for synthesis of $BaCuSi_2O_6$ while even a small deviation of 5°C leads to a noticeable increase in the formation of the impurity phases.

Previous studies show that synthesis of a pure phase of $BaCuSi_2O_6$ is challenging due to the formation of multiple impurity phases, which are usually $BaCu_2Si_2O_7$ and $BaCuSi_4O_{10}$

[10], but $Ba_4Si_6O_{16}$, $BaSiO_3$ and Cu_2O can also contribute [29]. The sintering temperature has dramatic impact on the impurity formation. It was found that polycrystalline crystal growth of $BaCuSi_2O_6$ performed at sintering temperature of 1000°C forms impurity phases of $BaCu_2Si_2O_7$ and $BaCuSi_4O_{10}$ apart of the main phase whereas sintering at a higher temperatures, such as of 1100°C, leads to the decomposition of main phase $BaCuSi_2O_6$ [10]. A decrease in the obtained amount of $BaCuSi_2O_6$ observed after sintering at 1100°C can also be attributed to the reduction of Cu^{2+} to Cu^{1+} which takes place at temperatures above 1050°C [10]. Sheptyakov *et al.* found that pressing the powder prior to sintering is one method of reducing the impurity phases [29]. They sintered the ground precursors mixture at 900°C for 20 h and pulverized the resulting powder which then was pelletized and sintered at 1010°C for 20 h. These conditions lead to formation of small amount of several impurity phases. Sheptyakov *et al.* identified the composition of their impurity phases as $BaCu_2Si_2O_7$, $BaCuSi_4O_{10}$, $Ba_4Si_6O_{16}$, $BaSiO_3$ and Cu_2O and determined that approximately 93% of their sample is in the main $BaCuSi_2O_6$ phase.

Another factor which influences on the amount of the impurity is the duration of sintering. Recent studies reveal that the long sintering time (approximately 300 hours) reduces amount of impurities even without prior pulverizing and pressing the sample [10, 30]. The present thesis will quantitatively explore the effect of time of sintering on the impurities formation in polycrystalline sample $BaCuSi_2O_6$.

Polycrystalline $BaCuSi_2O_6$ can also be synthesized via mild hydrothermal method in a narow pH range [34]. However, the necessary resources for this technique were unavailable and cannot be used for this work.

4.1.3 Characterization by powder x-ray diffraction

Powder X-ray diffraction measurements were taken after 100 h, 210 h and 300 h of sintering to control the quality of the sample and monitor the evolution of the impurity phases during the crystal growth. The diffractograms for $BaCuSi_2O_6$ were taken over the 2θ angles from 10° to 70° in steps of 0.045° with measuring time of 8 s per point.

The top graph in Figure 4.2 shows the refined diffraction pattern of $BaCuSi_2O_6$ when the sample had been sintered for 100 h. To fit the data we used the model that consisted of five expected phase: $BaCuSi_2O_6$, $BaCu_2Si_2O_7$, CuO, $BaCO_3$ and SiO_2 where CuO, $BaCO_3$ and SiO_2 are precursors. The initial parameters of the crystal structures for these phases have been taken from published data and then clarified during the analysis [35–39]. The refined lattice parameters of that sample are given in the first column of table 4.1 whereas the refined atomic positions are given in table 4.2. The atomic positions of $BaCuSi_2O_6$ are in good agreement with the values published in Reference [35]. Refinement reveals that the sample mainly consists of composition of $BaCuSi_2O_6$ and $BaCu_2Si_2O_7$ being 76.44% and 13.74% respectively with small amount of precursors left. The impurity phase $BaCu_2Si_2O_7$ can be seen in the diffraction patten as two peaks at 22.7°and 32.8°(blue diamonds in Figure 4.2) which withstood throughout the whole sintering process. The presence of other reported impurities such as $BaCuSi_4O_{10}$ and $Ba_4Si_6O_{16}$ [40, 41] were sought for but were undetectable. Therefore they were not included in the model. See table 4.1 for the full breakdown of impurity phases.

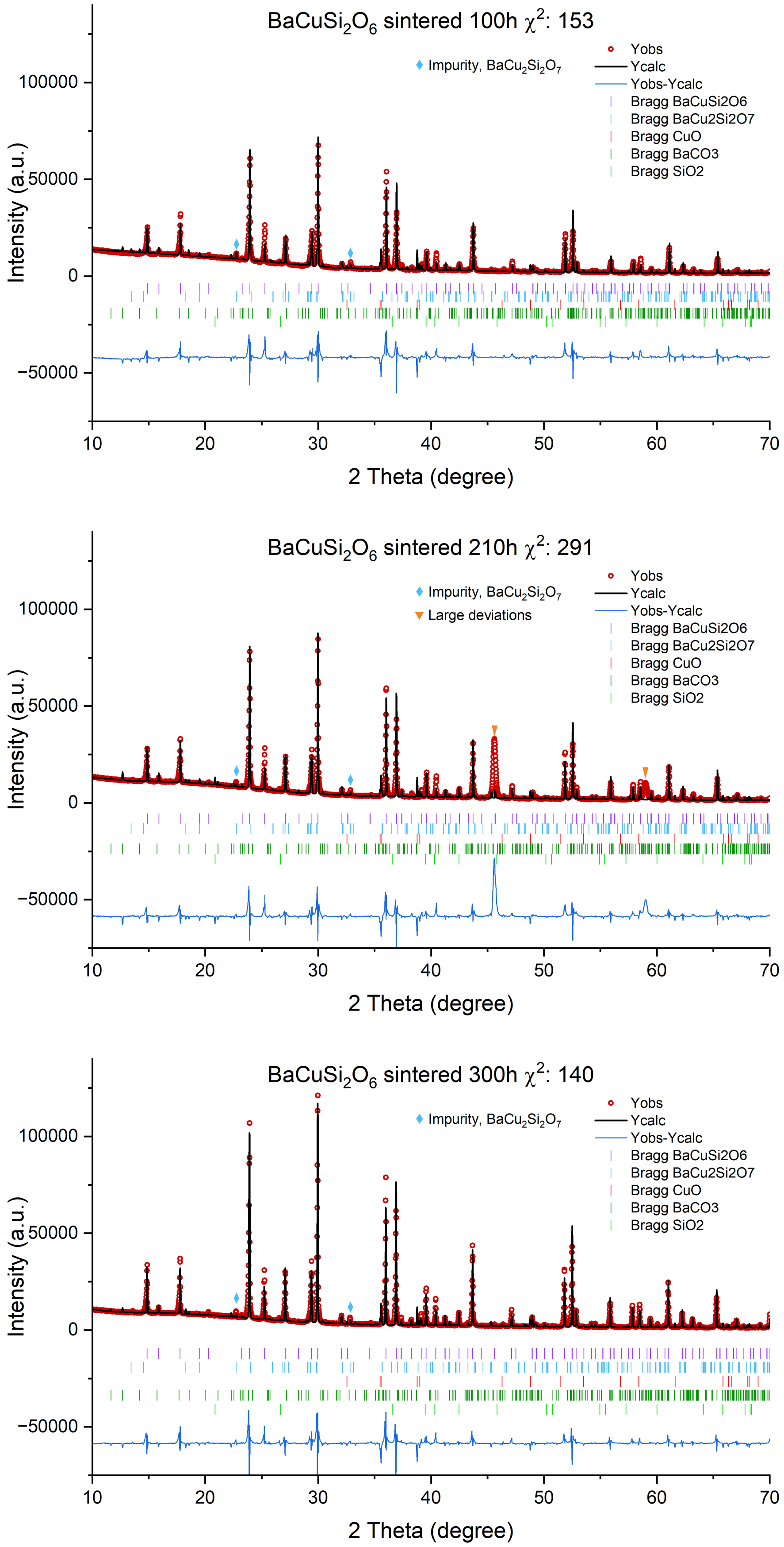

Figure 4.2: Rietveld refinement of the $BaCuSi_2O_6$ powder x-ray diffraction data taken after 100 h (top), 210 h (middle) and 300 h (bottom) of sintering. The red circles are the data points, the black line is the model, the blue line is the difference between data and model and the vertical bars are Bragg peak positions of the different phases included in the model. All data was collected at room temperature

The refined PXRD-pattern of the sample sintered for 210 h is presented in the middle graph in Figure 4.2. The refinement has been done using the same set of phases as for the sample sintered for 100 h. The results reveal that after 210 hours of sintering the amount of the amount of the main phase $BaCuSi_2O_6$ is slightly raising from 73 to 75 % and the main contribution to the impurities is given by biphase $BaCu_2Si_2O_7$ which found to be 11.67 %. Thus, both $BaCuSi_2O_6$ and $BaCu_2Si_2O_7$ phases have increased in amount and percent while the precursors have decreased compared to sintering at 100 h. The refined lattice parameters of $BaCuSi_2O_6$ are given in the second column of table 4.1 whereas the refined atomic positions are given in table 4.3. The atomic positions of $BaCuSi_2O_6$ match the values published in Reference [35]. In addition to identified phases, two extra peaks appear in the diffraction pattern at 2θ of 45.6°and 59.0 ° (orange triangles in Figure 4.2). We were unable to identify both peaks but they both disappeared after sintering for 300 h and therefore, do not affect the final sample.

The refined PXRD-pattern taken on the sample sintered for 300 h is presented in the bottom graph in Figure 4.2. The refined lattice parameters of that sample are given in the third column of table 4.1 whereas the refined atomic positions are given in table 4.4. The unidentified impurity peaks that appear after sintering for 210 h disappeared which leads to the highly probable conclusion that the impurity decomposed upon further sintering. Refinement concluded that the sample was phase impure still after 300 h of sintering but has consistently improved compared to shorter sintering times. The composition of $BaCuSi_2O_6$ and $BaCu_2Si_2O_7$ was 84.83% and 8.19% respectively with small amounts of precursor left. The main phase $BaCuSi_2O_6$ increased while the biphase $BaCu_2Si_2O_7$ and precursors decreased. See table 4.1 for the full breakdown of impurity phases.

The synthesis of $BaCuSi_2O_6$ was deemed sufficiently successful to carry out further characterization of its magnetic properties.

	100 h	210 h	300 h	Ref. [10]
a, b [Å]	9.96133(9)	9.95759(8)	9.96988(6)	9.970(1)
c [Å]	22.28564(33)	22.28014(30)	22.30434(24)	22.304(4)
Composition	%	%	%	%
$BaCuSi_2O_6$	76.44(1.19)	79.55(1.46)	84.83(0.92)	–
$BaCu_2Si_2O_7$	13.74(0.72)	13.00(0.81)	8.19(0.45)	–
CuO	5.93(0.07)	5.05(0.07)	3.99(0.03)	–
$BaCO_3$	3.23(0.36)	1.82(0.39)	2.50(0.21)	–
SiO_2	0.66(0.01)	0.58(0.01)	0.49(0.00)	–

Table 4.1: Lattice parameters and phase compositionsat room temperature for the polycrystalline sample of $BaCuSi_2O_6$ sintered for 100 h, 210 h and 300 h at 1035°C and data from reference. Refined from PXRD data.

100 h			
Atom	x	y	z
Ba	0.25	0.99058	0.5
Cu	0	0.25	0.06421
Si	0.27082	0.75026	0.88772
O1	0.22158	0.72826	0.82432
O2	0.35358	0.88164	0.86073
O3	0.29974	0.77371	0.05075

Table 4.2: Atomic positions for $BaCuSi_2O_6$, sintered for 100 h, refined from PXRD data.

210 h			
Atom	x	y	z
Ba	0.25	0.99058	0.5
Cu	0	0.25	0.06364
Si	0.26375	0.76386	0.88730
O1	0.20794	0.77284	0.82227
O2	0.38987	0.90482	0.86751
O3	0.28114	0.80138	0.05017

Table 4.3: Atomic positions for $BaCuSi_2O_6$, sintered for 210 h, refined from PXRD data.

300 h			
Atom	x	y	z
Ba	0.25	0.99057	0.5
Cu	0	0.25	0.06390
Si	0.27361	0.75347	0.88485
O1	0.21121	0.71907	0.82276
O2	0.36382	0.87858	0.85917
O3	0.31342	0.77526	0.05737

Table 4.4: Atomic positions for $BaCuSi_2O_6$, sintered for 300 h, refined from PXRD data.

Ref [10]			
Atom	x	y	z
Ba	0.245	0	0.25
Cu	0	0.25	0.062
Si	0.276	0.756	0.872
O1	0.208	0.743	0.810
O2	0.366	0.851	0.861
O3	0.310	0.781	0.065

Table 4.5: Atomic positions for $BaCuSi_2O_6$, sintered at 1035°C from [10].

4.1.4 Magnetic susceptibility measurements in ambient pressure

The samples' magnetic properties were measured at the Advanced Materials Characterisation Facility at the University of Birmingham in collaboration with Dr. Mingee Chung, Dr. Matthew Coak and Dr. Aly Abdeldaim from the Condensed Matter Group.

Experimental settings

The magnetic susceptibility measurements of powder sample of $BaCuSi_2O_6$ were performed using MPMS3 from Quantum Design. The sample was first manually ground in an agate mortar and then weighed and mounted to the sample holder. The sample with mass of 73.9 mg was zero field cooled with a cool rate of 12 K per minute until it reached base temperature of 1.9 K. The measurements of DC magnetic susceptibility were taken continuously from 1.9 K to 300 K with a sweep rate of 2 K per minute in a magnetic field of 1 T.

General results

Figure 4.3 presents the susceptibility data collected over the temperature range from 1.9 K to 300 K. The data were normalized to obtain the susceptibility per mole of Cu^{2+} magnetic ion. The results reveal the paramagnetic behavior at high temperatures (above 100 K)

With decreasing temperature the data display a broad maximum at $T \approx 30$ K that can be attributed to short-range magnetic correlations and is widely observed in quasi-low dimensional quantum magnets [42, 43]. Below this maximum, the susceptibility smoothly drops till $T \approx 10$ K. The absence of any additional sudden and sharp features suggests the absence of phase transitions in the compound. At temperatures lower than $T < 10$ K, the susceptibility increases sharply as the temperature approaches zero. This behavior is usually named Curie tail and is attributed to the presence of almost paramagnetic impurities [7]. Apart from the sharp increase due to the paramagnetic impurity contribution, magnetic susceptibility of $BaCuSi_2O_6$ tends towards zero at a finite temperature. This behavior indicates the presence of the energy gap in the magnetic excitation spectra of $BaCuSi_2O_6$ and suggests that system is dimerized. However, the temperature at which the susceptibility reaches zero is obscured by the sharp Curie impurity tail.

The low temperature region $1.9 \text{ K} \leq T \leq 4.9$ K was fitted to account for the impurities' and the temperature independent contributions, such as diamagnetic contribution, to the magnetic susceptibility. This helps clearly distinguish the crystal's magnetic behavior from the magnetic properties of the impurities. The impurity and the temperature independent contributions are plotted in the solid red line in Figure 4.3. The yellow circles in Figure 4.3 show the data after subtracting the impurity contributions. It follows the same temperature behavior with the raw data but has a lower amplitude of the maximum at $T \approx 30$ K and raises the susceptibility in the paramagnetic region by a small amount. It reaches zero between 4.33 K and 4.63 K, confirming the presence of an energy gap in the excitation spectrum of the sample.

The magnetic exchange interactions present in $BaCuSi_2O_6$, the sign and magnitude of the magnetic interactions, can be estimated from the fit analysis using the models that were discussed in section 2.3. This will be done after initial Curie-Weiss analysis.

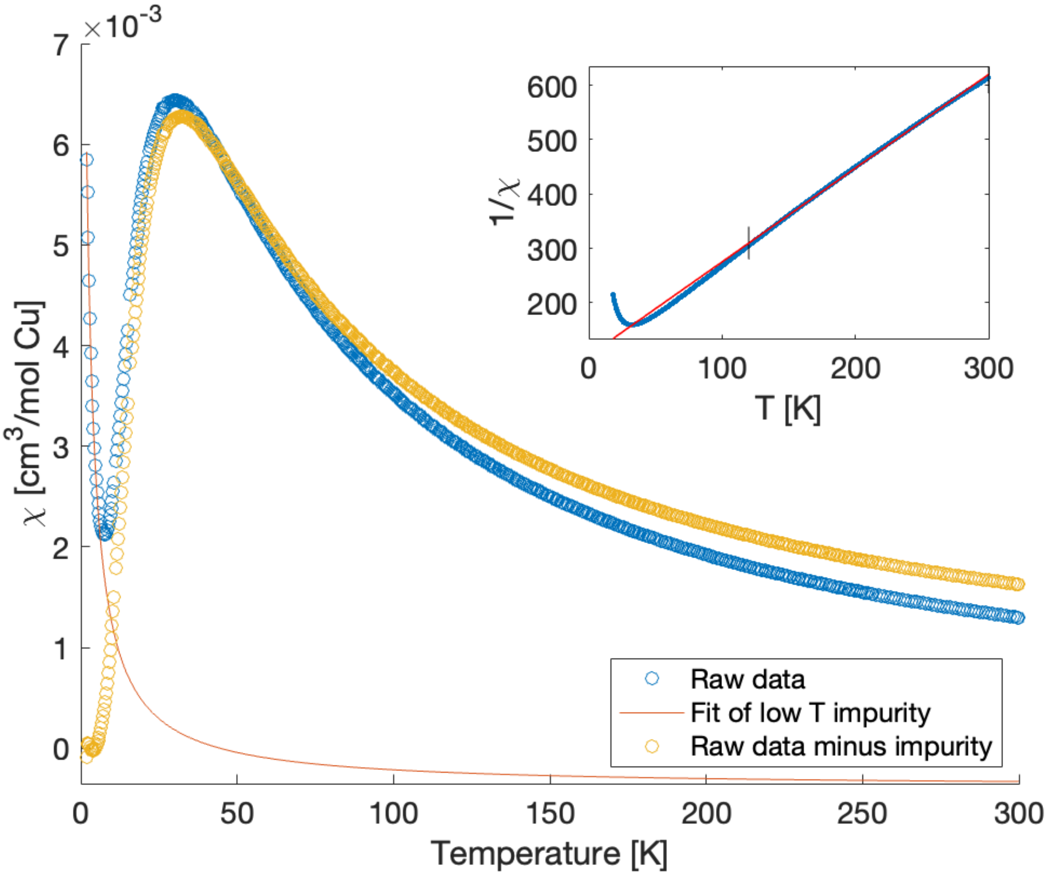

Figure 4.3: The powder magnetic susceptibility χ of $BaCuSi_2O_6$ measured in an applied magnetic field of 1 T, normalized to the molar amount of Cu^{2+} ions. Inset shows the inverse susceptibility after the substruction of the impurity Curie tail. The impurity-corrected inverse susceptibility data was fitted to Curie-Weiss law over the temperature range of 120 - 300 K which is indicated by bars on the plot.

Curie-Weiss behavior

The magnetic system is in a paramagnetic state in the high temperature region, where analysis with the Curie-Weiss law can be performed to determine the Curie-Weiss temperature of $BaCuSi_2O_6$. Ferromagnets are characterized by a positive Curie-Weiss temperature while antiferromagnets have a negative Curie-Weiss temperature. Thus, the sign of Curie-Weiss temperature of $BaCuSi_2O_6$ enables the determination of the type of the dominant magnetic exchange interaction in the system. The inverse susceptibility after correcting for the impurity contribution in the normalized raw data is plotted in the inset of Figure 4.3. Because it is unknown above which temperature $BaCuSi_2O_6$ is in the paramagnetic phase, the data was fitted over the temperature region T_{start}–300 K where T_{start} was varied between 80 K $\leq T \leq$ 240 K. The final T_{start} was chosen to be $T = 120$ K because at higher T_{start} the results of fit analysis remains the same. By fitting the inverse susceptibility over the high temperature region the Curie-Weiss temperature θ_{CW} and the Curie constant C were found to be $-59.5(3)$ K and $0.5797(5)$ $\mathrm{cm^3K/mol}$ respectively. The results reveal that the Curie-Weiss temperature of $BaCuSi_2O_6$ is negative and therefore the dominant magnetic interaction is antiferromagnetic.

Fitting data with the isolated dimer model

The green curve in Figure 4.4 is the fit of the magnetic susceptibility (χ) data of $BaCuSi_2O_6$ to the isolated dimer model which is defined by equation 2.9 and 2.10. The extracted parameters are found to be $\chi_0 = 5.2(3) \times 10^{-5}$ cm^3/mol, $C_{imp} = 1.52(1) \times 10^{-2}$ cm^{3}K/mol, $\theta_{CW,imp} = -0.75(4)$ K, $C = 0.5109(8)$ cm^{3}K/mol and $J_{intra} = 4.399(6)$ meV. The extracted value of $J_{intra} = 4.399(6)$ meV is in good agreement with previously published $J_{intra} = 4.5$ meV obtained with the same approach [31].

The fit of the isolated dimer model with only the dominant intradimer exchange interaction J_{intra} provides a good agreement with the data almost over whole temperature region except 25-35 K where χ has a maximum. Indeed, the fitted curve in Figure 4.3 goes noticeably above the data suggesting that the isolated dimer model does not ideally describe $BaCuSi_2O_6$.

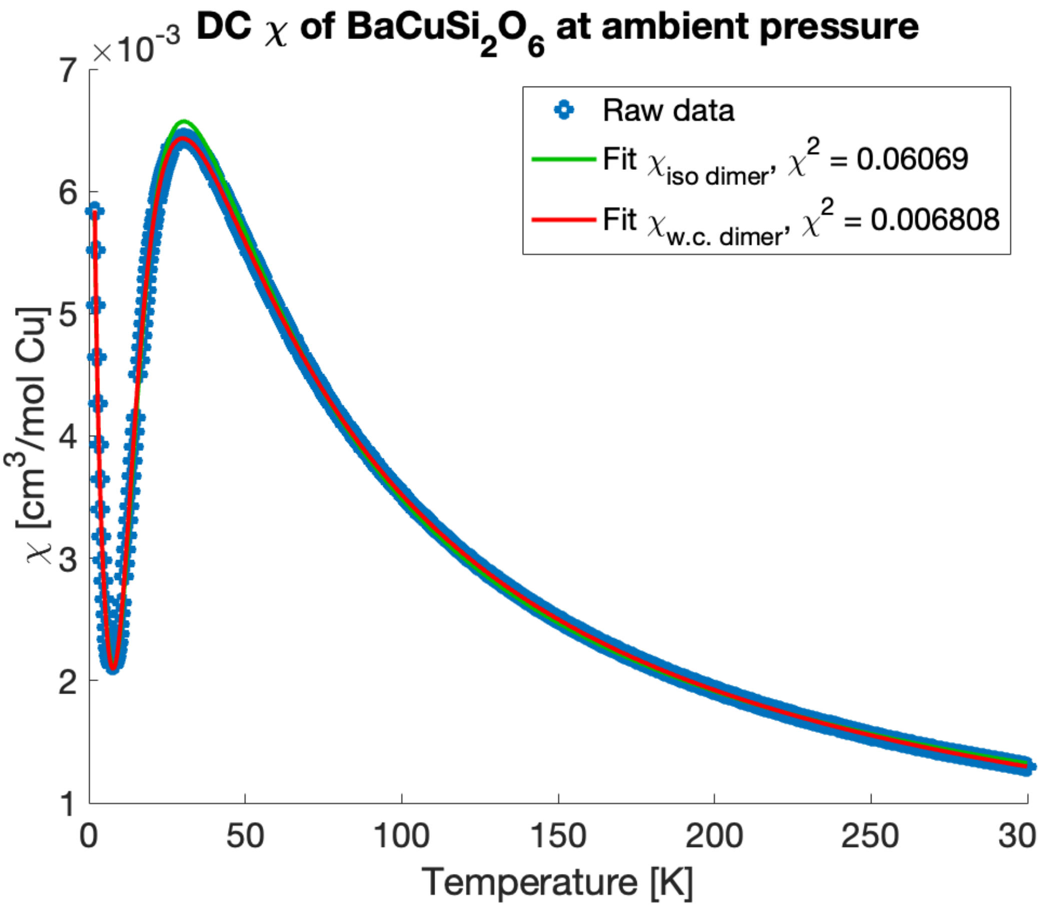

Figure 4.4: The raw susceptibility data χ of $BaCuSi_2O_6$ fitted with the isolated dimer model and the weakly coupled dimer model. The blue open circles are the raw data points, the green solid line is the fit to the isolated dimer model while the red solid line is the fit to the weakly coupled dimer model.

Fitting data with the weakly coupled dimer model

The red curve in Figure 4.4 is the fit of the raw data to the weakly coupled dimer model as defined by equation 2.9 and 2.11. This model takes into account both the dominant intradimer- and a weaker interdimer-dimer exchange interactions in $BaCuSi_2O_6$.

The parameters were found to be $\chi_0 = -1.01(3) \times 10^{-4}$ cm^3/mol, $C_{imp} = 1.618(5) \times 10^{-2}$ cm^{3}K/mol, $\theta_{CW,imp} = -0.82(1)$K, $C = 0.578(1)$ cm^{3}K/mol, $J_{intra} = 4.389(2)$ meV and $J'_{inter} = 3.008(48)$ meV. Although the sum contribution of the interdimer couplings J'_{inter} is found to be significant, the value of intradimer exchange J_{intra} extracted from the weakly dimer model remains almost the same with the one obtained using the isolated dimer approach.

Discussion

The results of the fit analysis performed using the weakly coupled dimer model (solid red line in Figure 4.5) can be compared to the results of the isolated dimer model (solid green line in Figure 4.5) where all parameters have been varied during the fit. The weakly coupled dimer model provides much better agreement with the data than the isolated dimer model suggesting that the interdimer coupling has to be taken into account. This can be visually determined from Figure 4.4 as well as from comparison of the chi-square agreement as reported in the figure's legend for the respective fits. There is a factor of 10 improvement of the chi-square parameter for the weakly coupled dimer model with respect to the isolated dimer model. This fit however estimates that the dominant and weaker secondary exchange are of similar magnitude, which is contradictory to previous findings for $BaCuSi_2O_6$ that estimated that the secondary interdimer exchange would be $\sim 10\%$ of the dominant intradimer exchange [5, 30].

Previous studies on $BaCuSi_2O_6$ estimated the magnitudes of the J_{intra} and J'_{inter} exchange coupling using various experimental and theoretical methods that have different sensitivity in determining the exchange couplings. To investigate the agreement of J_{intra} and J'_{inter} obtained in this work with the previously published results, the data was fitted using weakly coupled dimer model where J_{intra} and J'_{inter} were fixed to the values published in literature while other parameters were varied. If only J_{intra} was available in the reference, then J'_{inter} was also varied. The values of the fixed and varied parameters are summarized in table 4.6 for different models where first two columns provide values obtained in the present thesis using isolated and weakly coupled dimers models, respectively. The third, forth and fifth columns provide the results extracted from the fit analysis of our experimental data using the weakly-coupled dimer model where J_{intra} and J'_{inter} were fixed to the values taken from References [5, 30, 32]. Note, that in the third column J'_{inter} was also varied during the fit, because Sasago *et al.* estimated only J_{intra} in their work [31].

Figure 4.5 presents all results of the fitting carried out in this section. The inset is a close up of the peak region. The yellow dot-dash curve in Figure 4.5 shows the results obtained using the weakly coupled dimer model with J_{intra} fixed to 4.5 meV as obtained from Sasago *et al.* [31] and J'_{inter} was freely varied. The comparison of the fit to the results obtained using weakly-coupled dimer model where both J_{intra} and J'_{inter} were varied (red line in Figure 4.5) reveals that J_{intra} set to 4.5 meV provides worse agreement with the data. The extracted J'_{inter} for the both cases are found to be the same and independent if J_{intra} was set to 4.5 meV or freely varied.

The solid orange curve in Figure 4.5 shows the fit of the experimental data to the weakly coupled dimer model with J_{intra} and J'_{inter} fixed to 4.45 meV and 0.58 meV according to the work of Jaime *et al.* [5]. The results reveal that the weakly coupled dimer model with J_{intra} set to 4.45 meV and J'_{inter} set to 0.58 meV describe the experimental data even worse then the previous model where J_{intra} was taken from work of Sasago *et* *al.* and J'_{inter} was freely varied.

In addition, the experimental data was fitted to the weakly coupled dimer model with J_{intra} and J'_{inter} fixed to 4.45 meV and 0.51 meV respectively as obtained from Sebastian *et al.* [32]. This fit is plotted by the black dashed curve in Figure 4.5 and reveal that this model provides the worst agreement with the data compared to all other models that were just discussed above.

Parameter	Isolated	W.C.	Sasago	Jaime	Sebastian
C [cm^{3}K/mol]	0.5109(8)	0.578(1)	0.587(3)	0.5278(6)	0.526(6)
J_{intra} [meV]	4.399(6)	4.389(2)	4.5	4.45	4.45
J_{inter} [meV]	-	3.008(48)	3.0(1)	0.58	0.51
χ_0, 1×10^{-6} [cm^3/mol]	52(3)	-101(3)	-132(7)	7(3)	1.1(3)
C_{imp}, 1×10^{-2}[cm^{3}K/mol]	1.52(1)	1.618(5)	1.79(1)	1.623(9)	1.620(9)
$\theta_{CW,imp}$ [K]	-0.75(4)	-0.82(1)	-1.23(3)	-0.95(3)	-0.95(3)

Table 4.6: Table of different obtained and input parameters

However, the fit with the isolated dimer model is still acceptable at $\chi^2 = 0.06069$.

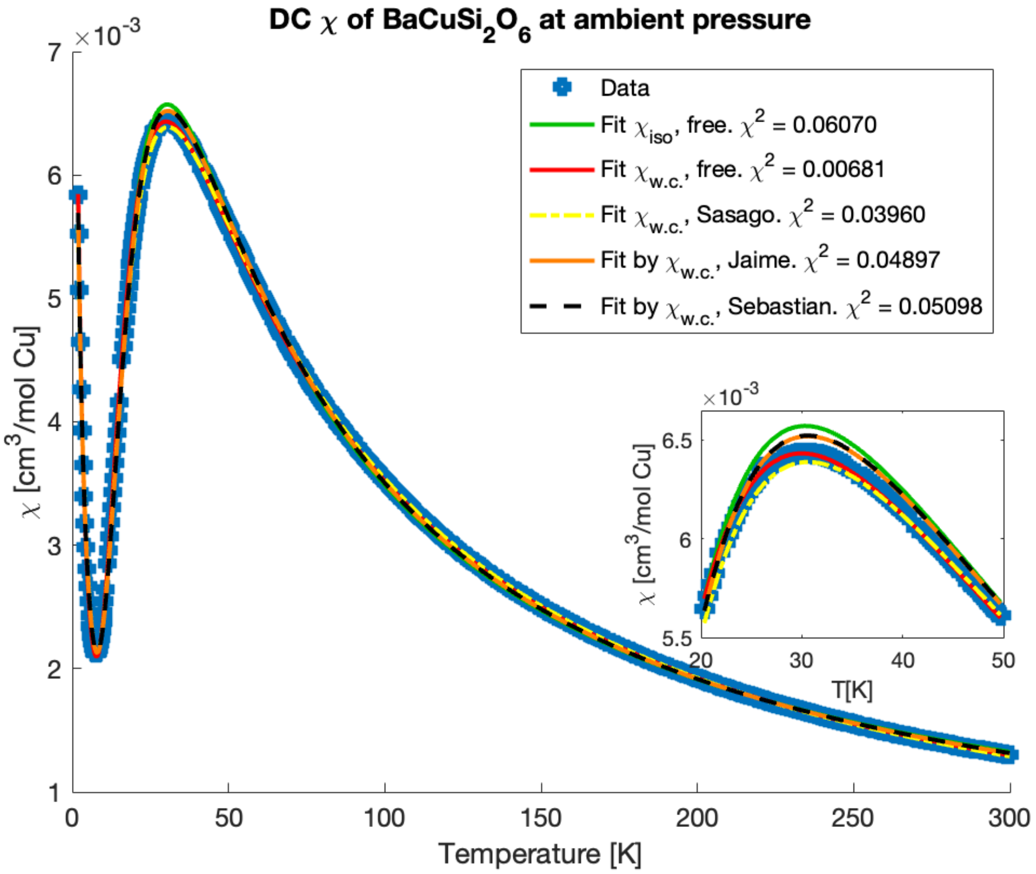

Figure 4.5: The raw susceptibility data χ as a function of temperature T for $BaCuSi_2O_6$ in an applied field of 1 T. Data fitted with isolated dimer model, weakly coupled dimer model and partially fitted weakly coupled dimer model with literature values.

The values obtained by freely fitting the intradimer exchange interactions for both the isolated and the weakly coupled dimer model are consistently comparable to those previously published in magnitude, $J_{intra} = 4.4$ meV. Thereby we can conclude with confidence that the dominant intradimer exchange interaction is positive and is 4.4 meV.

There is consistently a large difference between the weaker interdimer exchange interaction and that of all published figures. The obtained $J_{inter} = 3.008 \approx 3.0$ meV is of comparable magnitude to that of the dominant intradimer exchange interaction. This is contradictory to the assumption in the weakly coupled dimer model that the significantly weaker interdimer exchange would be. This can be accounted for by looking more closely at the weakly coupled dimer model used to analyse the data, that is equations 2.11. J'_{inter} in the model is the sum of the interdimer exchange interactions. More accurately, it is the effective field on each spin due to coupling with neighboring spins, which is the sum of the couplings for interdimer couplings [43]. The values for the interdimer exchange J_{inter} extracted from previous studies were the exchange constants between neighboring in-plane dimers only. This indicates that there is more than one interdimer exchange acting on a dimer, making the sum of the interdimer exchange to be a combination.

A simple example for how to evaluate the relationship between the obtained sum J'_{inter} and individual interdimer exchanges J_{inter} will now be presented. If a simplistic model of the 2D-AFM lattice for $BaCuSi_2O_6$ is constructed, the sum can be assumed to consist of four equivalent interdimer exchanges if all four nearest-neighbor dimers in the lattice are regarded as equivalent. The fitted value $J'_{inter} = 3.0$ meV would then be divided to $J_{inter} = 0.75$ meV. The magnitude of this estimate would be more in line with that of previously reported single interdimer exchanges of J_{inter}. As previously stated, determining the magnitude of the weak interdimer exchange cannot be done with confidence via static susceptibility measurements alone. Other techniques such as single crystal inelastic neutron scattering are necessary. In turn single crystal samples would be required for the mentioned techniques which are beyond the resources in time and equipment available for this thesis.

None of the fitted solutions favour a model where the weak interdimer interaction J'_{inter} was negative. Thereby, the case where the interdimer interaction would be ferromagnetic can be excluded.

4.1.5 Magnetic susceptibility measurements under applied pressure

The samples' magnetic properties were measured at the Advanced Materials Characterisation Facility at the University of Birmingham in collaboration with Dr. Mingee Chung, Dr. Matthew Coak and Dr. Aly Abdeldaim from the Condensed Matter Group.

Experimental settings

The high-pressure powder magnetic susceptibility measurements of $BaCuSi_2O_6$ were also performed using the MPMS3 from Quantum Design.

The investigated powder sample of $BaCuSi_2O_6$ sample was initially pelletized using 2 ton of applied pressure to create a pellet 1.3 mm in diameter. From this 1.3 mm pellet a smaller pellet was manually obtained by cutting and scraping a piece that would fit inside the pressure cell. The mass of the final measured sample was 26.0 mg. The small pelletized sample was placed inside a Teflon tube with a diameter of 1.7 mm. The tin-manometer was placed inside the tube inside the pressure cell before being filled with the pressure transmitting medium Daphne Oil 7373. To apply pressure, the locking nuts on the cell were tightened to compress the cell, obtaining applied pressure on the sample. The applied compression was indicative of the approximate pressure applied as given by the manual for the pressure cell as provided by Quantum Design.

Before starting susceptibility measurements over the whole temperature range, a sweep of the magnetic DC moment from 3.2 K to 3.8 K was taken to determine the final pressure. The shift of tin's superconducting transition temperature within this temperature range was used to determine the applied sample pressure within the cell.

The sample was zero field cooled at 5 K per minute from 300 K to 10 K and then cooled at a rate of 1 K per minute until it reached 1.9 K. A magnetic field of 1 T was applied before measurements were taken. The measurements of DC susceptibility were taken continuously from 1.9 K to 300 K with a sweep rate of 0.8 K per minute.

General results

The raw magnetic susceptibility data of $\mathrm{BaCuSi_2O_6}$ was normalized to obtain the susceptibility χ per mole of magnetic Cu^{2+} ion. Figure 4.6 presents the normalized χ of $\mathrm{BaCuSi_2O_6}$ under three different pressure conditions, including the fits with the weakly coupled dimer model. The three pressure conditions were ambient pressure (P_0), under 4.7 kbar (P_1) and under 7.9 kbar (P_2). The data for all pressures display the same temperature behavior as those at ambient pressure described in chapter 4.1.4. A difference for the different pressures was in the shift of their peak positions and the height of the maximum. The difference in peak positions indicate that the pressure affected the dominant intradimer exchange J_{intra} while the height of the peak could be due to both a change in the interactions J_{intra}, J_{inter} and the g-factor. The differences will be further analyzed in the later subsection when analyzed using the weakly coupled dimer model.

For the measurements in ambient pressure, the same impurity tail fitting from chapter 4.1.4 up to and including 4.9 K. The data under 4.7 kbar of applied pressure was fit with the impurity tail up to and including 5.3 K while the data from the highest pressure at 7.9 kbar was fit with the impurity tail up to and including 3.6 K. These impurity fits were kept constant for the following analysis of the Curie-Weiss behavior and of the Landé g-factor.

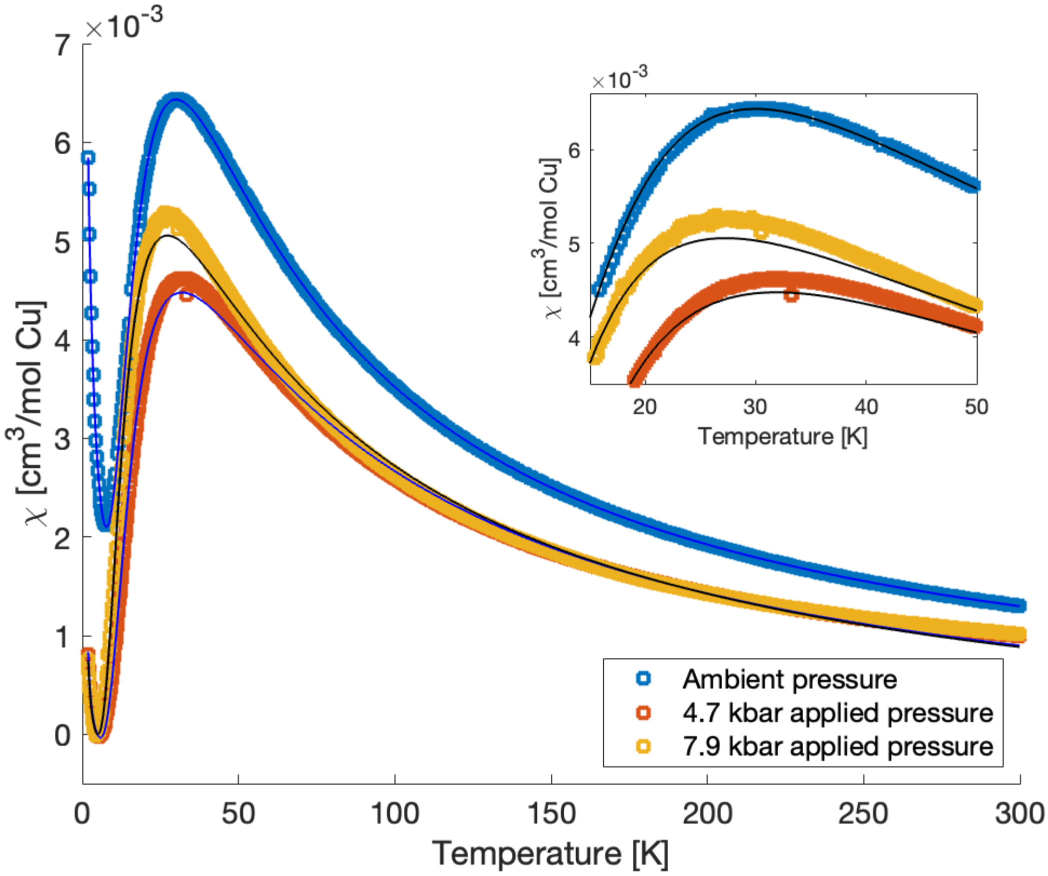

Figure 4.6: The temperature dependence of the magnetic susceptibility χ for $BaCuSi_2O_6$ in an applied field of 1 T. Data points for ambient pressure (blue), upon applying 4.7 kbar (red) and 7.9 kbar of pressure (yellow), normalized to the molar amount of Cu^{2+} ions. Inset is zoomed in on the peak region of the plots.

Curie-Weiss behavior

The analysis of the Curie Weiss behavior of $BaCuSi_2O_6$ at the three different pressures was carried out for different respective temperature ranges due to the system reaching its paramagnetic regime at different temperatures once subjected to applied pressure.

The paramagnetic temperature range for ambient pressure was $120\ \text{K} \leq T \leq 300\ \text{K}$. The Curie-Weiss temperature θ_{CW} and the Curie constant C were found to be $-59.5(3)$ K and 0.5797(5) $\text{cm}^3\text{K/mol}$ respectively when freely fit.

The paramagnetic temperature range for 4.7 kbar of applied pressure was $235\ \text{K} \leq T \leq 300\ \text{K}$. The Curie-Weiss temperature θ_{CW} and the Curie constant C were found to be $-139.3(1)$ K and 0.6015(6) $\text{cm}^3\text{K/mol}$ respectively when freely fit.

The paramagnetic temperature range for 7.9 kbar of applied pressure was $220\ \text{K} \leq T \leq 300\ \text{K}$. The Curie-Weiss temperature θ_{CW} and the Curie constant C were found to be $-186.3(1)$ K and 0.723(2) $\text{cm}^3\text{K/mol}$ respectively when freely fit.

Fitting data with the weakly coupled dimer model

The data at different pressures was fit with the weakly coupled dimer model as defined by equation 2.9 and 2.11 in chapter 2.3. Figure 4.6 presents the best fits as a solid black line at each respective temperature. The values for all fitted interactions are summarized in table 4.7.

Keeping in mind that the Landé g-factor has been suggested to be affected by pressure [44, 45], the analysis under pressure was extended to compare how the fit varies with different g-factors. The figures for visual comparison can be found in Appendix A. The Landé factor affects the Curie constant that in turn is related to height of the peak in susceptibility as described by equation 2.13. This is to investigate whether the difference in peak height can be explained by the g-factor changing with pressure and to ensure that the conclusions drawn about the magnetic interactions J are correct.

The g-factor for $BaCuSi_2O_6$ was previously found to be $g_c = 2.31$ and $g_{ab} = 2.03$ for a single crystal at ambient pressure [30]. The different g-factors compared in addition to the fitted value were the average of the literature values for $g = 2.17$ and the value obtained from freely fitting the Curie-constant of the $BaCuSi_2O_6$ sample at ambient pressure $g = 2.48$. The average of the literature values $g = 2.17$ was used because the measured sample was polycrystalline and no preferred crystal orientation should dominate the g-factor.

When first comparing the fitted value of $g = 2.48$ at ambient pressure with $2.03 \leq g \leq 2.31$ as found previously, our value was already outside the expected range for a polycrystalline average. This disagreement can be attributed to the limitation of the model and to the fitting of the impurity tail but the value is still acceptable. Once 4.7 kbar of pressure was applied, the fit for $g = 2.48$ was found to be significantly better than the fit with $g = 2.17$. The χ^2 goodness of fit improved from 1.175 to 0.190 when changing between fixing the g-factor from 2.17 to 2.48. The g-factor at 4.7 kbar is unlikely to be 2.17 as indicated by the poor fit. The obtained freely fit value for the g-factor at 4.7 kbar of pressure was 2.48(9) and was 2.56(8) for 7.9 kbar of pressure.

At 4.7 kbar the extracted Curie constant was $C = 0.577(1)$ cm^{3}K/mol. Both the intradimer interaction $J_{intra} = 4.447(7)$ meV and the sum of the interdimer interactions $J'_{inter} = 8.9(2)$ meV were found to increase in size compared to in ambient pressure. This increasing behavior was shown for all values of g. The sum of the intradimer and the interdimer exchanges $J_{tot} = 13.4(2)$ meV has increased as well when compared to the total at ambient pressure.

At 7.9 kbar the extracted Curie constant was $C = 0.613(1)$ cm^{3}K/mol. A lower value for the intradimer exchange J_{intra} was yielded for all g-factors than the value obtained at ambient pressure, with $J_{intra} = 3.8(2)$ when freely fitting C. However, the sum of the interdimer exchanges $J'_{inter} = 10.2(9)$ meV increased relative to ambient pressure. Thus, the sum of exchanges $J_{tot} = 14.0(1.1)$ meV has continued to increase when compared to the values obtained at ambient pressure and at 4.7 kbar of applied pressure.

Pressure	Ambient	4.7 kbar	7.9 kbar
T_{peak} [K]	32.7	31.6	26.5
θ_{CW} [K]	-59.5(3)	-139.3(1)	-186.3(1)
C [cm^{3}K/mol]	0.578(1)	0.577(1)	0.613(1)
J_{tot} [meV]	7.398(9)	13.3(2)	14.0(1.1)
χ^2	0.0068	0.076	0.15
	Interactions		
J_{intra} [meV]	4.390(2)	4.447(8)	3.8(2)
J'_{inter} [meV]	3.009(5)	8.9(2)	10.2(9)
J_{inter} [meV]	0.752(1)	2.225(5)	2.55(20)

Table 4.7: Table of different values measured at different pressures. Note: $J'_{inter} = 4J_{inter}$

Discussion

It cannot be concluded for certain that the changing maxima of the peaks with varied pressure is unrelated to a change in g due to pressure. It is most probable that the change is related to both a change in g and a change in the magnetic interactions of the system. The following speculations will however be supported by comparison with theoretically expected values and examining the behavior of all available parameters.

The behavior of the susceptibility of $BaCuSi_2O_6$ upon applying pressure is consistent with the weakly coupled dimer model's description of how J_{tot} and J_{intra} affects the susceptibility. The maximum's height is related to the interplay between the dominant intradimer exchange J_{intra}, the interdimer exchange J_{inter} and the Curie constant C. The position of the peak is also weakly related to the interdimer exchange J_{inter} present in the system but is more strongly related to the dominant intradimer exchange J_{intra}. The peak position of the maxima shifts marginally towards lower temperatures as pressure is applied while the shift is larger upon applying more pressure. This is consistent with the behavior of the intradimer interaction J_{intra} increasing marginally by $\sim$ 1% upon applying 4.7 kbar while the interdimer interaction J_{inter} increases by almost 200%. For these changes, the small increase in J_{intra} shifts the peak marginally to higher temperatures while the large increase in J_{inter} shifts the peak strongly to lower temperatures due to the size of the change. The peak shifts more significantly to lower temperatures upon applying 7.9 kbar of pressure. The intradimer interaction J_{intra} has decreased by $\sim$ 13% compared to at ambient pressure while the interdimer exchange J_{inter} has increased by 240%. The overall effect on the peak is a significant shift further towards lower temperatures as both interactions work in the same direction.

The steadily increasing total J_{tot} in $BaCuSi_2O_6$ with increasing pressure is also consistent with the behavior of the Curie-Weiss temperature θ_{CW} extracted from the paramagnetic region of the sample. J_{tot} increases and suggests that the antiferromagnetic interactions in the sample increases with applied pressure. This is supported by the steadily increasing magnitude of the Curie-Weiss temperature also indicating increasingly antiferromagnetic interactions in the sample.

4.1.6 Conclusion

High quality powder crystalline sample of $BaCuSi_2O_6$ was grown using solid-state reaction. The quality of the sample was characterized using PXRD and reveal a small amount of the impurity contribution with less than 7% and with only one biphase. The effect of the sintering time on the impurity formation was explored. The results reveal that 300 h of sintering is required for the pure phase formation while shorter sintering time leads to formation of extra impurity phases that decompose at longer sintering time.

The static magnetic susceptibility measurements of polycrystalline $BaCuSi_2O_6$ yielded results for the intradimer and interdimer couplings J_{intra} and J_{inter} at ambient conditions and under applied pressures. The value of J_{intra} in $BaCuSi_2O_6$ was found to be $J_{intra} = 4.389(2)$ meV which is in good agreement with all earlier published results. The J_{intra} only slightly varies with applied pressure, achieving its maximum value $J_{intra} = 4.447(8)$ meV at the intermediate pressure of 4.7 kbar. The interdimer coupling between two neighboring dimers is estimated to be $J_{inter} = 0.75$ meV which is in reasonable agreement with earlier published data. The interdimer coupling J_{inter} is found to be strongly affected by applying pressure. It rised steadily and achieved its maximum value $J_{inter} = 2.55$ meV at 7.9 kbar. This predicts a broader bandwidth of the dispersion but a lowering of the gap in the magnetic excitation spectra of $BaCuSi_2O_6$.

Moreover, the Curie-Weiss temperature of $BaCuSi_2O_6$ was extracted at ambient conditions and under applied pressure for the first time. At ambient conditions it was $\theta_{CW}=$ -59.5 K and rose with pressure to θ_{CW} = -186.3 K at 7.9 kbar. This is consistent with the observed increase of the total values of the magnetic exchange couplings observed in the system.

However, background measurements of the pressure cell are necessary to clarify the values of J_{inter} and θ_{CW} extracted from the analysis of susceptibility data of $BaCuSi_2O_6$ collected under pressure. Inelastic neutron scattering measurements of $BaCuSi_2O_6$ under high-pressure are necessary to fully explore the effects of pressure on the magnetic interactions in $BaCuSi_2O_6$.

4.2 Barium copper vanadate $BaCu_2V_2O_8$

4.2.1 Overview

$BaCu_2V_2O_8$ is a quasi-1D antiferromagnetic-ferromagnetic (AFM-ferromagnetic (FM)) dimerized chain. It is a tetragonal crystal structure with space group $I\bar{4}2d$ with lattice parameters $a = b = 12.744$ Å and $c = 8.148$ Å where the Cu^{2+} magnetic ions are coordinated by O^{2-} into square planar plaquettes, as seen in figure 4.7. These plaquettes are arranged in a screw chain along the c axis. It is along the c-axis that the dimers couple in one dimension, where the dimers are formed by the strong antiferromagnetic coupling and interact with each other weakly via ferromagnetic intradimer coupling [11].

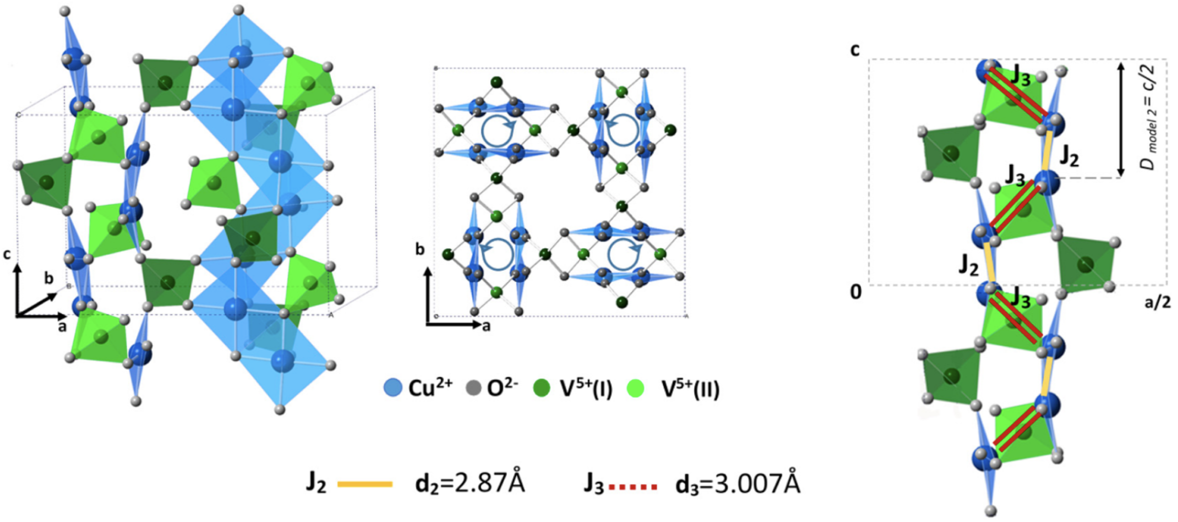

Figure 4.7: (left) The crystal structure of $BaCu_2V_2O_8$. Ba^{2+} ions are omitted and only two of four chains are shown for clarity. (middle) Projection of the crystal structure on the ab plane. Circles indicates the direction of rotation of the screw chain along the c axis. (right) The model of the screw chain arrangement within the crystal lattice. J_3 is the AFM intradimer coupling and J_2 is the FM interdimer coupling. Figure taken with permission from [11]

The magnetic properties of the Cu^{2+} magnetic ions with spin-$\frac{1}{2}$ are best described by the Hamiltonian [1]:

$$\hat{H} = \sum_i J_{intra}\vec{S}_{i,1} \cdot \vec{S}_{i,2} + J_{inter}\vec{S}_{i,2} \cdot \vec{S}_{i+1,1} \tag{4.3}$$

Here J_{intra} and J_{inter} are the intradimer and interdimer exchange couplings respectively whereas i is the index of the dimer site. A positive value for either exchanges J indicate antiferromagnetic interaction while a negative value indicates ferromagnetic interaction.

The magnetic exchange interactions have been determined via static magnetic susceptibility measurements on a single crystal [11]. These values differed depending on if they were taken with the magnetic field parallel or perpendicular to the c-axis of the crystal. When the magnetic field was applied parallel to the c-axis, the interactions were experimentally determined to be $J_{intra} = 39.67$ meV and $J_{inter} = -12.52$ meV whereas for applying the magnetic field perpendicular to the c-axis they were $J_{intra} = 39.94$ meV and $J_{inter} = -7.23$ meV. The observed deviation was attributed to the experimental error and values were averaged to the the final of $J_{intra} = 39.80 \pm 0.13$ meV and $J_{inter} = -9.87 \pm 2.64$ meV [11].

Results from further single crystal inelastic neutron scattering measurements of $BaCu_2V_2O_8$ amended $J_{intra} = 40.92$ meV and $J_{inter} = -11.97$ meV, unambiguously confirming that the interdimer coupling is ferromagnetic [11]. The observed magnetic excitation spectrum reveals that the energy gap is $\Delta = 35.37$ meV with a bandwidth of ~ 10 meV [11].

In particular, we are interested in investigating the effects of pressure on the strength and sign of the magnetic exchange interactions in $BaCu_2V_2O_8$.

4.2.2 Synthesis

The powder sample of $BaCu_2V_2O_8$ was synthesized using solid state reaction

$$BaCO_3 + 2\,CuO + V_2O_5 \longrightarrow BaCu_2V_2O_8 + \uparrow CO_2 \tag{4.4}$$

The precursors $BaCO_3$ (99.95% Thermo Fisher Scientific), CuO (99.9995% Thermo Fisher Scientific) and V_2O_5 (99.99% Thermo Fisher Scientific) were mixed in a 1:2:1 molar ratio with 2.9945g, 2.4142g and 2.7597g respectively to obtain 7.3 g of $BaCu_2V_2O_8$ powder [11]. The precursors were mixed in a small amount of ethanol before being sintered in an AL23 alumina crucible at 680°C for 24 h total. One instance intermediate grinding was performed after 12h of sintering. Every sintering process was heated and cooled at 175°C per hour.

The single crystal $BaCu_2V_2O_8$ used for magnetic susceptibility measurements was grown in the Crystal Laboratory at the Helmholtz Zentrum Berlin für Materialien und Energie (HZB) by Dr. Nazmul Islam using the floating zone method described in chapter 3.1.1. The polycrystalline feed rod was grown via solid-state reactions as described earlier in this section by mixing $BaCO_3$, CuO and V_2O_5 in a 1:2:1 molar ratio. The powder mixture was sintered in air at 650°C for 24 h total, with one instance of intermediate grinding. The powder was then packed into a rubber balloon and pressed hydrostatically up to 3 kbars in a cold-isostatic-pressure machine and sintered in air at 750°C for 12 h to form a dense cylindrical rod. The TFSZ technique used a small amount of off-stoichiometric solvent with 5 mol.% excess V_2O_5, that was prepared by solid-state reactions as for the feed rod. The single crystal was grown in ambient air atmosphere at a speed of 0.2 mm/h [11].

4.2.3 Characterization via powder x-ray diffraction

Figure 4.8 shows the refined diffraction pattern of $BaCu_2V_2O_8$ which was obtained on powder sample of $BaCu_2V_2O_8$ for 2θ angles between 10° and 80° in steps of 0.03° with measuring time of 8 s per point.

To fit the data we used the model that consisted of five expected phase: $BaCu_2V_2O_8$, $BaCuV_2O_7$, CuO, $BaCO_3$ and V_2O_5. The initial parameters of the crystal structures for these phases have been taken from published data and then clarified during the analysis [37, 38, 46–48]. Refinement concluded that the sample consisted of two phases, with composition of $BaCu_2V_2O_8$ and $BaCuV_2O_7$ being 46.29% and 45.61% respectively with small amounts of precursor left: 4.22% CuO, 1.24% $BaCO_3$ and 2.63% V_2O_5. The refined lattice parameters were $a = b = 12.75155(7)$ Å and $c = 8.14254(5)$ Å.

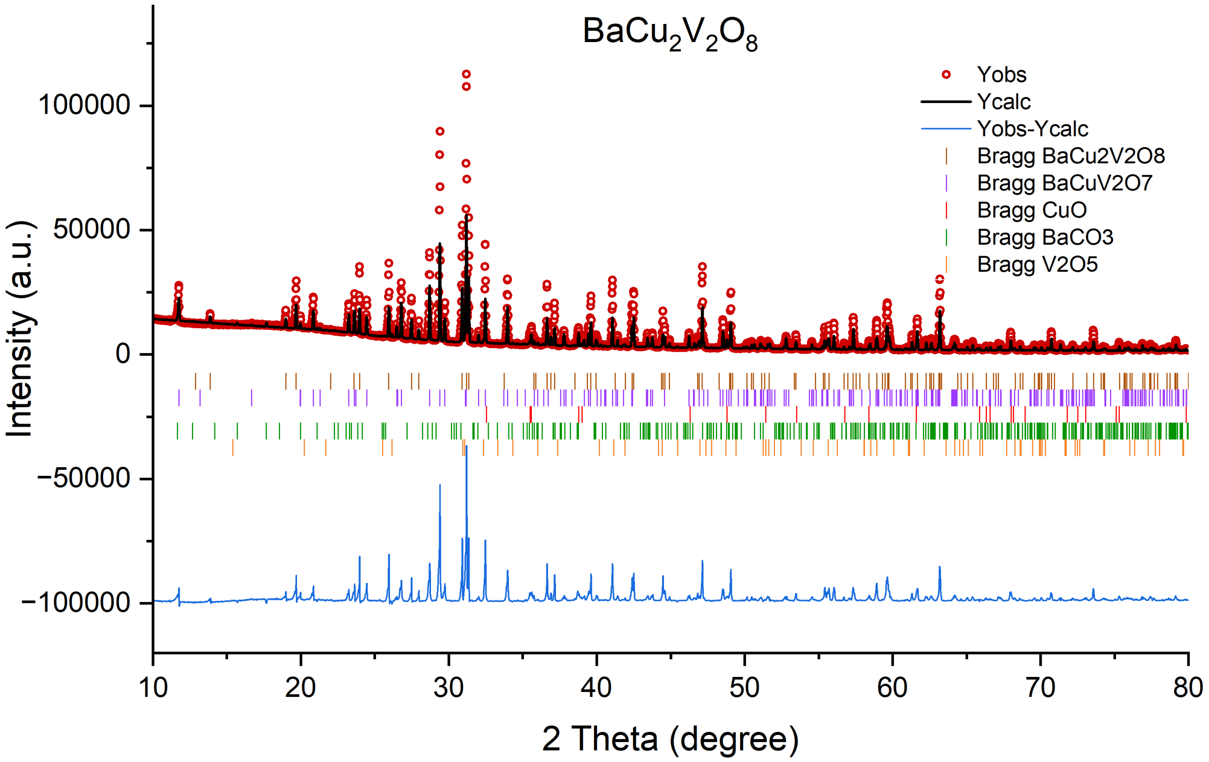

Figure 4.8: Rietveld refinement of the $BaCu_2V_2O_8$ powder x-ray diffraction data. The red circles are the data points, the black line is the model, the blue line is the difference between data and model and the vertical bars are Bragg peak positions of the different phases included in the model

Atom	x	y	z
Ba1	0.5	0.5	0
Ba2	0.5	0.5	0.5
Cu1	0.67229(77)	0.33992(73)	0.24668(269)
V1	0.25	0.55370(108)	0.875
V2	0.75	0.59390(120)	0.375
O1	0.81813(273)	0.31452(289)	0.25280(658)
O2	0.34453(400)	0.48432(272)	0.28226(738)
O3	0.13298(200)	0.16932(270)	0.49276(642)
O4	0.33783(409)	0.01979(249)	0.47965(754)

Table 4.8: Lattice parameters and atomic positions for $BaCu_2V_2O_8$, refined from PXRD data.

The diffractogram showed a significant amount of impurity was present in the sample. Initially, refinement of the data had many unaccounted peaks. Previous studies synthesizing $BaCu_2V_2O_8$ reported that small deviations from the molar ratio during crystal growth could drastically change the produced phase [49]. Many different phases form at similar sintering temperatures as the one used for synthesizing $BaCu_2V_2O_8$. The V^{5+} ions alongside the Cu^{2+} could also potentially change oxidation states and lead to the formation of numerous more impurity phases to include in the Rietveld refinement model.

4.2.4 Spectroscopic characterization

The sample's composition was investigated with spectroscopic techniques available at the SPECIES-beamline at MAX IV synchrotron laboratory following the initial characterization of the sample's bulk components using PXRD. This would provide a complementary technique to investigate the synthesized $BaCu_2V_2O_8$ sample and the oxidation state of the vanadium and copper ions.

The $BaCu_2V_2O_8$ sample was pelletized using a hydraulic press in prepearation for measurements. 1 tonne of pressure was applied for 10 minutes on a sample with a mass of $\sim$ 40 mg before being mounted onto the sample holder.

The reference compounds CuO and V_2O_5 from synthesis were mounted by pressing a small amount onto double sided carbon tape on another sample holder.

X-ray Photoelectron Spectroscopy

An initial survey scan from binding energy (BE) of 1000 to -2 eV was performed on the sample using an excitation energy of 1200 eV, step size of 0.5 eV and 0.1 s dwell time to create an overview of the surface's chemical composition. In figure 4.9 the main peaks at binding energy (BE) of 970, 810 and 550 eV can be assigned to Cu $2p$, Ba $3d$ and O $1s$ together with V $2p$, respectively. The small high-binding energy shift of main peaks and Fermi level with respect to the literature values can be attributed to the sample charging. The broad features at binding energy from 600 to 800 eV are typically assigned to the Cu LMM Auger spectra. From this overview, there is a distinct lack of the C $1s$ line around 285 eV. This strengthens the conclusion from PXRD measurements in chapter 4.2.2 that no carbon based by-phase is present, that is the CO_3 precursor.

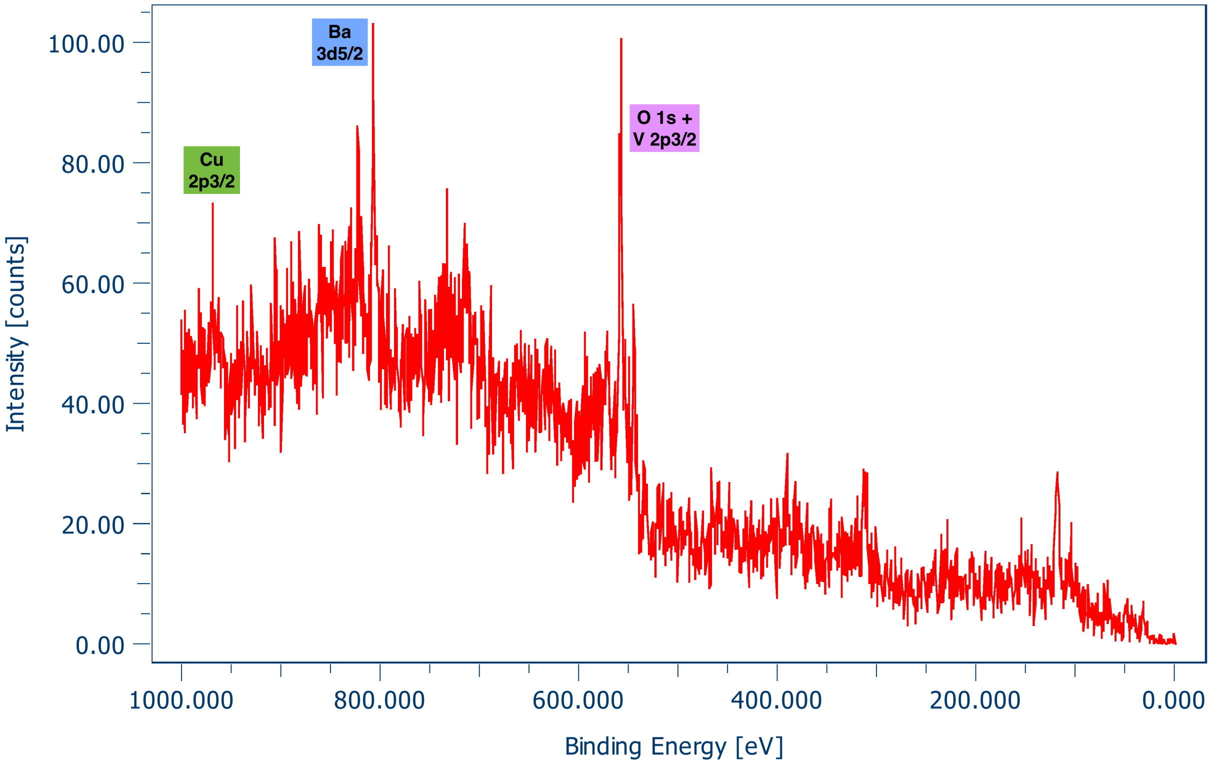

Figure 4.9: Overview XPS spectra of the $BaCu_2V_2O_8$-sample measured with an excitation energy of 1200 eV.

Figure 4.10 presents the high resolution Cu $2p_{3/2}$ spectra. The scan was performed between BE of 980 to 925 eV using an excitation energy of 1080 eV, step size of 0.05 eV and 0.1 s dwell time. Fitting the area of the Cu peak was performed using SpecsLab Prodigy's Fit Area function after subtracting a Shirley background. The $2p_{3/2}$ peak area was fit to 551 counts eV. Using the known intensity ratio from spin splitting of the p-orbital, the total area of the Cu $2p$ peak was found to be 826 counts eV.

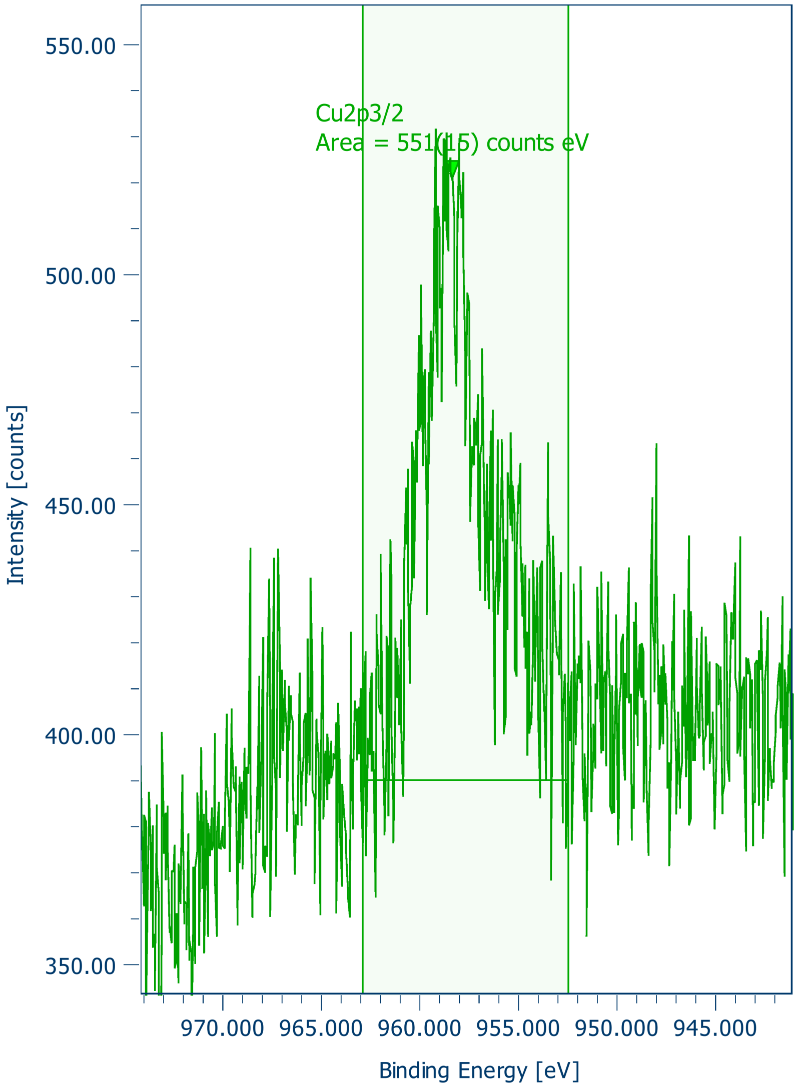

Figure 4.10: Core-level XP spectra of Cu $2p$ measured with an excitation energy of 1080 eV. The Cu $2p_{3/2}$ peak was fitted with the Shirley background.

The left graph in figure 4.11 presents the high resolution spectra obtained for the Ba $3d$ peak. The scan was performed between BE of 825 to 775 eV using an excitation energy of 930 eV, step size of 0.05 eV and 0.1 s dwell time. The Ba $3d$ peak was clearly split into its $3d_{3/2}$ and $3d_{5/2}$ peaks. The graph on the right is a close-up of the $3d_{5/2}$ peak located at 805.6 eV, whose area was fitted using SpecsLab Prodigy's Fit Area function to 1016 counts eV. Using the known intensity ratio from spin splitting of the d-orbital, the total area of the Ba $3d$ peak was found to be 1693 counts eV.

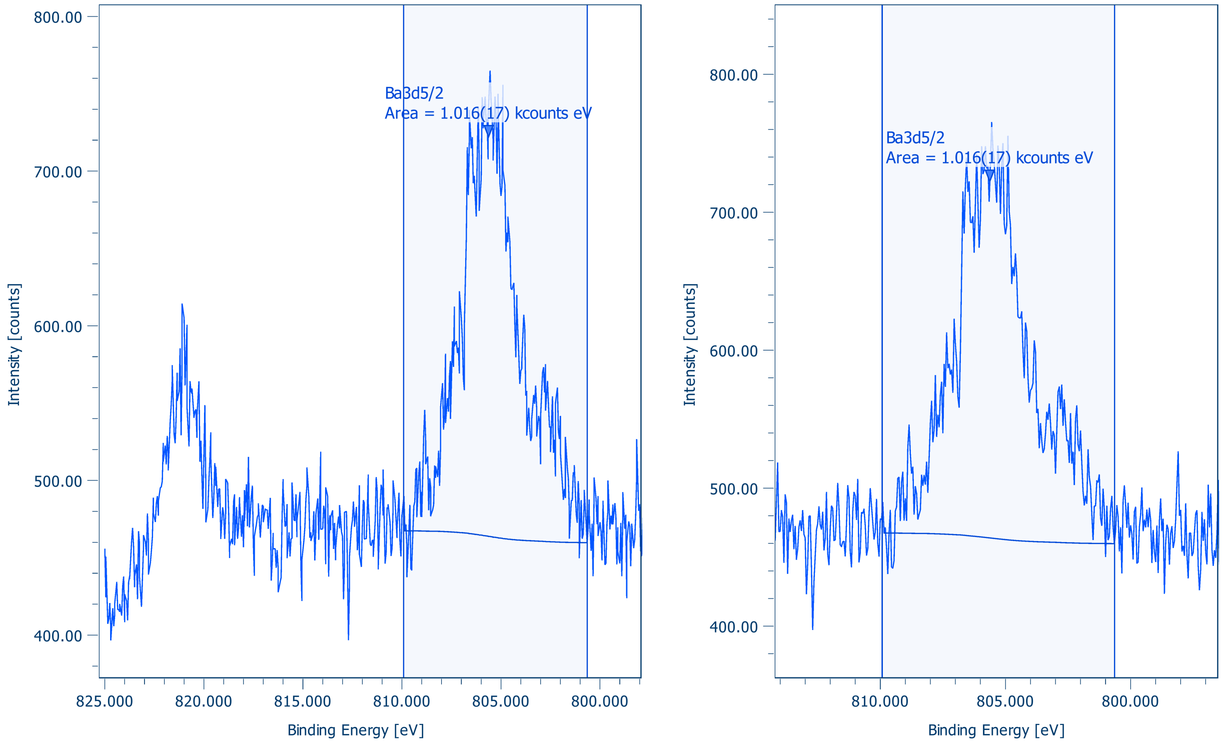

Figure 4.11: Core-level XP spectra of Ba $3d$ measured with an excitation energy of 930 eV. The Ba $3d_{5/2}$ peak (right) was fitted with the Shirley background.

The left graph in figure 4.12 presents the high resolution spectra obtained for the V $2p$ and O $1s$ peak observed around 550 eV. The scan was performed between BE of 560 to 505 eV using an excitation energy of 665 eV, step size of 0.05 eV and 0.1 s dwell time. The O $1s$ peak is clearly displayed at the higher side of the binding energy scale while the V $2p$ peak was split into its $2p_{1/2}$ and $2p_{3/2}$ peaks. The O $1s$ peak is partially cut-off as the chosen scan range did not capture the whole peak. This happened due to charging of the sample. This rendered the peak unusable for quantifying the oxygen-portion present in the sample.

The graph on the right in figure 4.12 is a close-up of the V $2p_{3/2}$ peak located at BE of 545.5 eV, whose area was fitted using SpecsLab Prodigy's Fit Area function to 2938 counts eV. Using the known intensity ratio from spin splitting of the p-orbital, the total area of the V $2p$ peak was found to be 4407 counts eV.

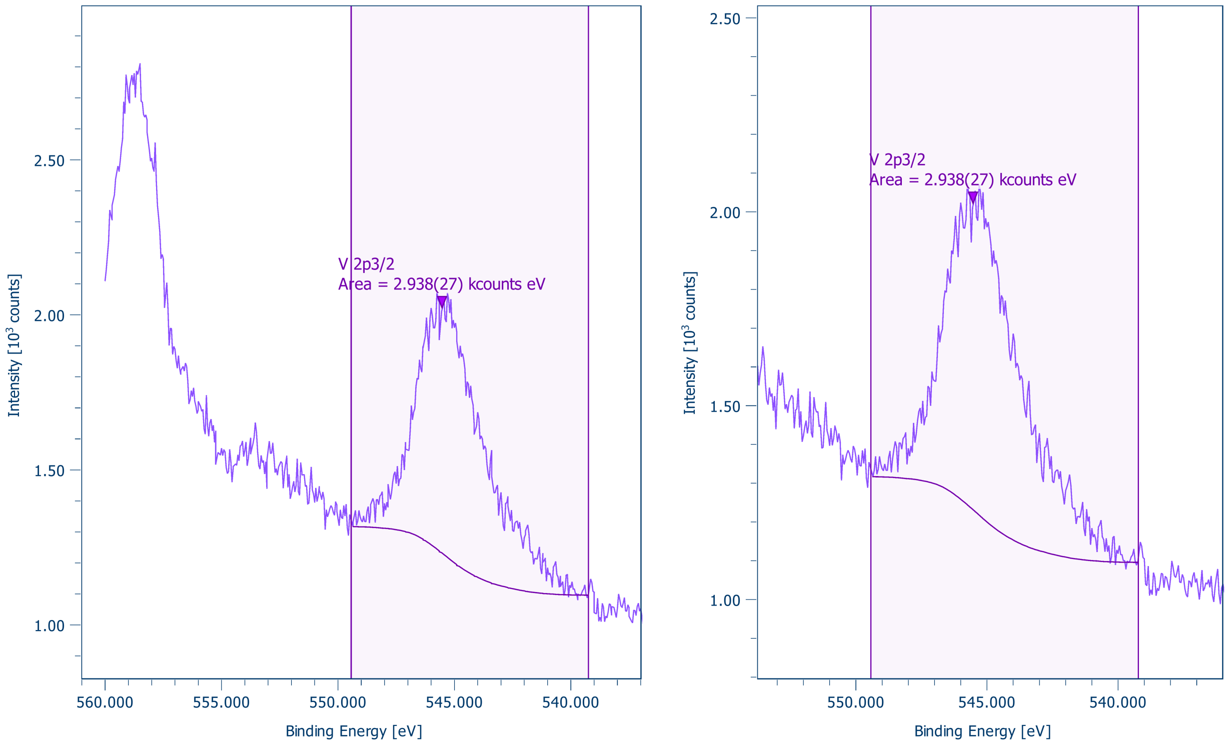

Figure 4.12: Core-level XP spectra of O $1s$ and V $2p$ measured with an exciting energy of 930 eV. The V2 $p_{5/2}$ peak (right) was fitted with the Shirley background.

The three high resolution spectra for the Cu $2p$, Ba $3d$ and V $2p$ peaks were used to quantitatively analyze the surface composition of the synthesized $BaCu_2V_2O_8$-sample. These results and necessary parameters are presented in table 4.9. The inelastic mean free path for electron scattering at 150 eV was found to be 4.69 Å [18]. The sensitivity factor S of the beamline is set by the photoionization cross-section of the peaks' orbital at the given wavelength, the IMFP of the electron's and the photon flux of the beamline.

Peak	Area [counts eV]	Cross section [Mbarn] [50]	Flux [photons/s]	Conc. [a.u.]	Conc. [at.%]
Cu $2p$	826	0.7831	4.45456E10	5.05182E-08	40.6
Ba $3d$	1 693	1.923	7.54163E10	2.48957E-08	20.0
V $2p$	4 407	1.104	1.73878E11	4.89502E-08	39.4

Table 4.9: Atomic surface composition of $BaCu_2V_2O_8$ sample using XPS. Kinetic energy of emitted electron is 150 eV and IMFP of 4.69 Å.

Measurements for all three peaks were repeated using a kinetic energy 500 eV to probe at a different depth of the surface. The inelastic mean free path for the electrons at 500 eV was found to be 9.4 Å [18]. An unreliable factor of the calculations for the surface concentration with these measurements is that the photoionization cross sections are not reported with as great detail at higher energies compared to at lower energies. This introduces a larger uncertainty in the sensitivity factors' underlying components. However it is still beneficial to compare the measurements recorded at this higher energy to those performed previously as a repetition and to investigate the composition further into the sample.

The scans were performed with the same scan intervals, using the same step size 0.05 eV and dwell time 0.1s as the previous measurements. The excitation energies were the only changed parameters, which were set to 1 430 eV, 1 280 eV and 1 015 eV for the Cu $2p$, Ba $3d$ and O $1s$ + V $2p$ peaks respectively. The high resolution spectra for all three peaks can be seen in figure 4.13 and the results are summarized in table 4.10. The signal-to-noise has improved for all peaks when compared to those obtained with a kinetic energy of 150 eV. This can be attributed to the increased IMFP of using a higher excitation energy and the overall increase of electrons being emitted.

Peak	Area [counts eV]	Cross section [Mbarn] [50]	Flux [photons/s]	Conc. [a.u.]	Conc. [at.%]
Cu $2p$	1 791	0.3671	8.99698E9	5.76881E-07	39.2
Ba $3d$	6 610	0.9444	1.93675E10	3.84453E-07	26.2
V $2p$	10 132	0.3940	5.37822E10	5.08691E-07	34.6

Table 4.10: Atomic surface composition of $BaCu_2V_2O_8$ sample using XPS. Kinetic energy of emitted electron is 500 eV and IMFP of 9.4 Å.

Tables 4.9 and 4.10 show that the ratio of Cu to V is nearly one and simultaneously two times greater than the concentration of Ba. These ratios are close to the stoichiometric ratio of $BaCu_2V_2O_8$. This observation might suggest that the by-phase concentration after synthesis is negligible on the surface of $BaCu_2V_2O_8$.

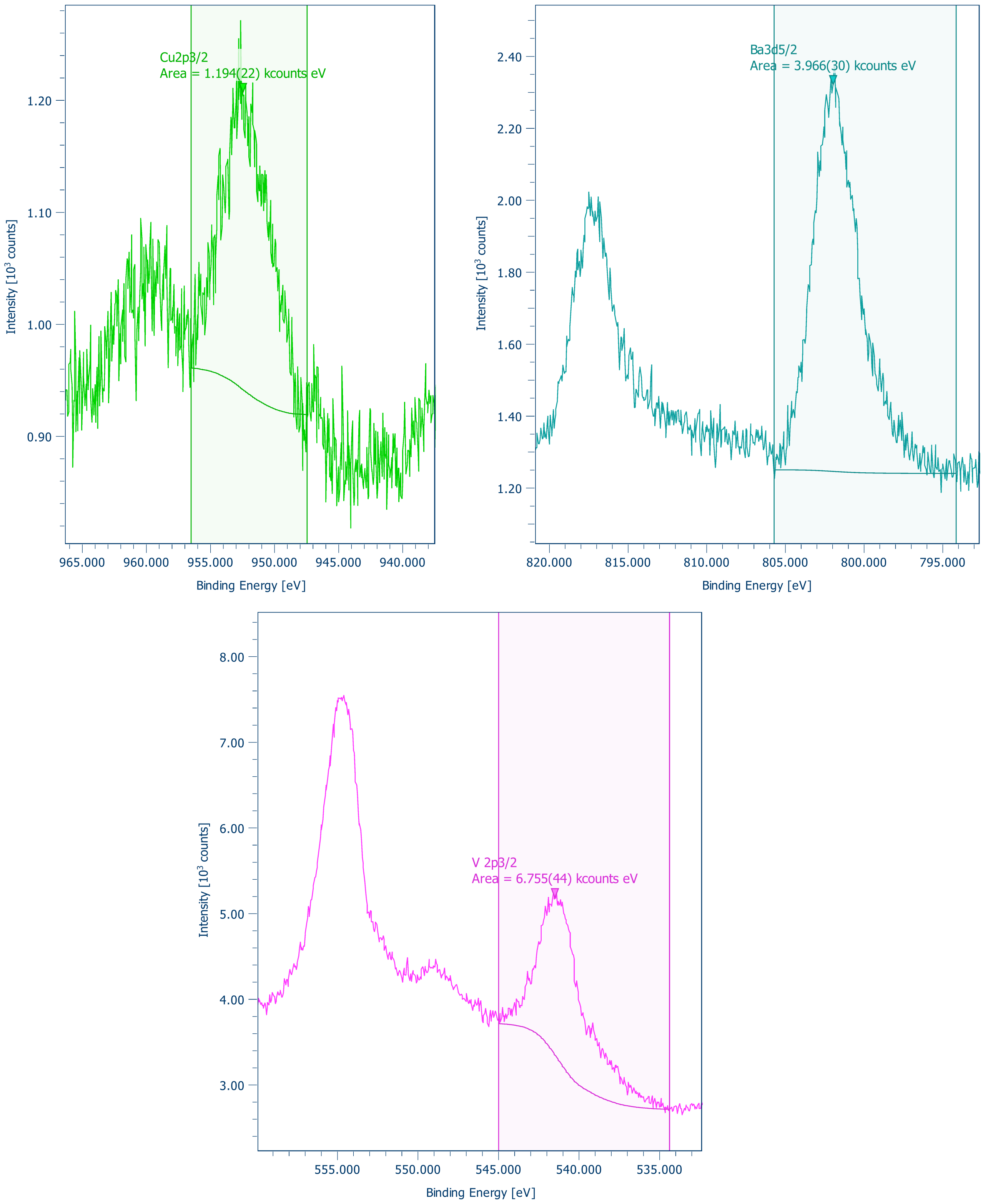

Figure 4.13: Core-level XP spectra of Cu $2p$, Ba $3d$ and O $1s$+V $2p$ regions measured with a kinetic energy 500 eV. All peaks were fitted with the Shirley background and fitted in SpecsLab Prodigy. Top left: Cu $2p$, top right: Ba $3d$, bottom: O $1s$ and V $2p$

Near Edge X-ray Absorption Fine Structure

NEXAFS measurements were performed in partial Auger electron yield mode in normal emission configuration.

Figure 4.14 shows the Cu $L_{2,3}$-edge absorption spectra for the CuO powder reference (blue line) and the synthesized $BaCu_2V_2O_8$ sample (orange line).

The sample's spectrum displays an intense narrow peak above photon energy of 930 eV without following wiggles. The overall shape of Cu L-edge of $BaCu_2V_2O_8$ is similar to CuO spectra which corresponds to transition Cu $2p$ electrons to partially filled Cu $2d^9$ orbitals. The NEXAFS spectrum of $BaCu_2V_2O_8$ differs from that of metallic Cu and Cu_2O[51]. In particular, the metallic Cu L-edge exhibits a significant continuous edge jump and three peaks above photon energy of 933 eV. On the other hand, the Cu L-edge of Cu_2O has its peak at photon energy of 934 eV. This is much higher than in the spectrum of $BaCu_2V_2O_8$ because of the difference in the number of d-electrons in Cu_2O, which has a completely filled d^{10} subshell [52].

We can conclude that the oxidation state of Cu in $BaCu_2V_2O_8$ is most likely +2 based on the similarities between the Cu L-edge of CuO and $BaCu_2V_2O_8$. This is in line with the described crystal and magnetic model of the copper from earlier chapters, where Cu^{2+} ions are coordinated into CuO_4 plaquettes that in turn form edge-sharing Cu_2O_6.

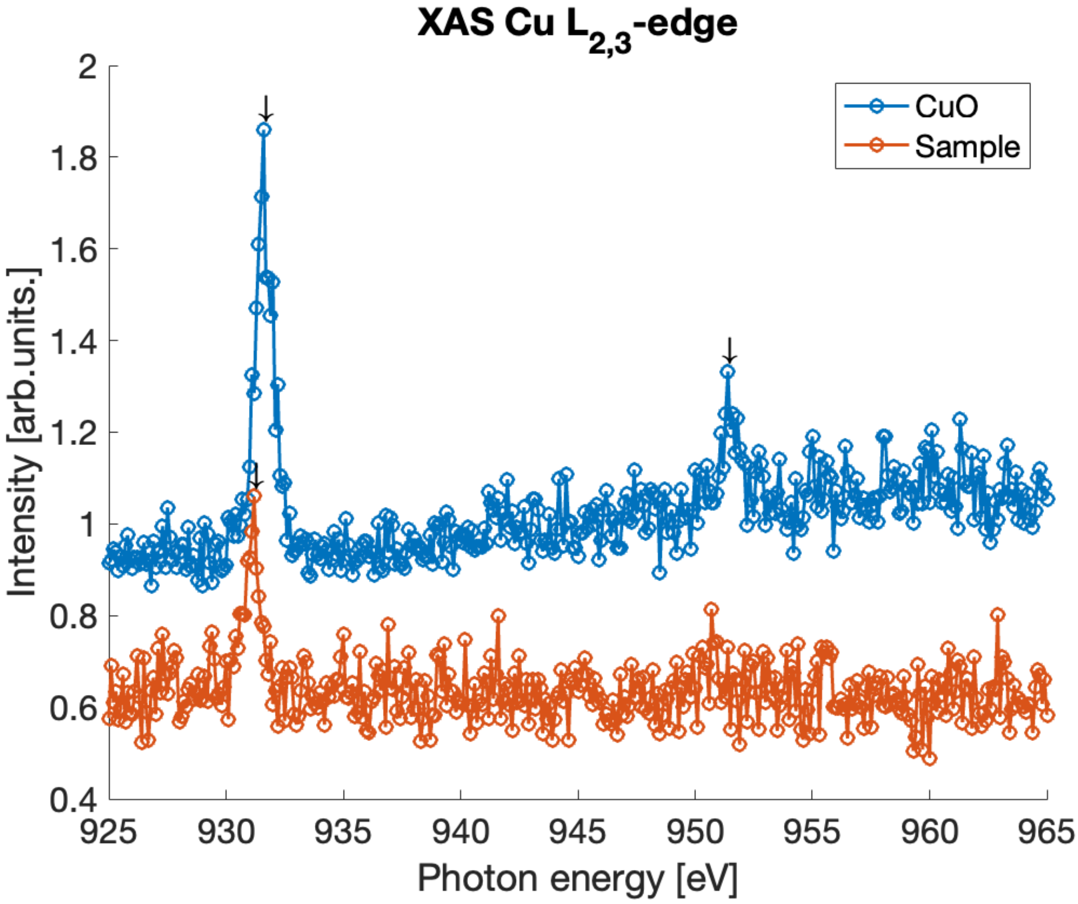

Figure 4.14: NEXAFS spectra of $BaCu_2V_2O_8$ (orange line) and CuO (blue line) in the vicinity of Cu $L_{2,3}$-edge.

Figure 4.15 shows the V $L_{2,3}$-edge (photon energy 513-527 eV) and O K-edge (photon energy 528-540 eV) absorption spectra for the V_2O_5 powder reference (blue line) and the synthesized $BaCu_2V_2O_8$-sample (orange line). The measured V_2O_5 reference spectrum is in a good agreement with literature [53]. The comparison of $BaCu_2V_2O_8$ V L- and O K-edge spectra with the same edges for vanadium oxides [53], V_2O_5, VO_2 and V_2O_3, reveals similarities in spectra of V_2O_5 and $BaCu_2V_2O_8$.

The V L_3-edge spectrum of $BaCu_2V_2O_8$ displays characteristic features at 515.3 eV and 516.3 eV before the maximum appears at 518.6 eV which correspond to transitions of V $2p$ electrons to the partially filled nonbonding V $3d_{xy}$ and unoccupied molecular π^*(V $3d_{xz}$ and V $3d_{yz}$ + O $2p$) and σ^* (V $3d_{z^2}$ and V $3d_{x^2-y2}$ + O $2p$) orbitals, respectively [54]. A second asymmetrical broad peak appears at 525.5 eV and corresponds to the V L_2-edge. It is impossible to resolve three peaks as in the L_3-edge because of final-state broadening of the peak that takes place due to core hole lifetime.

The corresponding O K-edge consists of two peaks at photon energy of 530 and 532 eV. These peaks can be assigned to transitions of O $1s$ electrons to the same unoccupied molecular π^*(V $3d_{xz}$ and V $3d_{yz}$ + O $2p$) and σ^* (V $3d_{z^2}$ and V $3d_{x^2-y^2}$ + O $2p$) orbitals, respectively. It should be noted that transition of s-electrons to d-orbitals is forbidden according to dipole selection rule. [21]

From these observations, it is likely that the oxidation state of the vanadium ions on the surface of the synthesized $BaCu_2V_2O_8$ is +5 as in the reference V_2O_5. This is in line with the described crystal and magnetic model of the vanadium in $BaCu_2V_2O_8$ from earlier chapters, where non-magnetic V^{5+} ions are coordinated into $[VO_4]^{3-}$ tetrahedra.

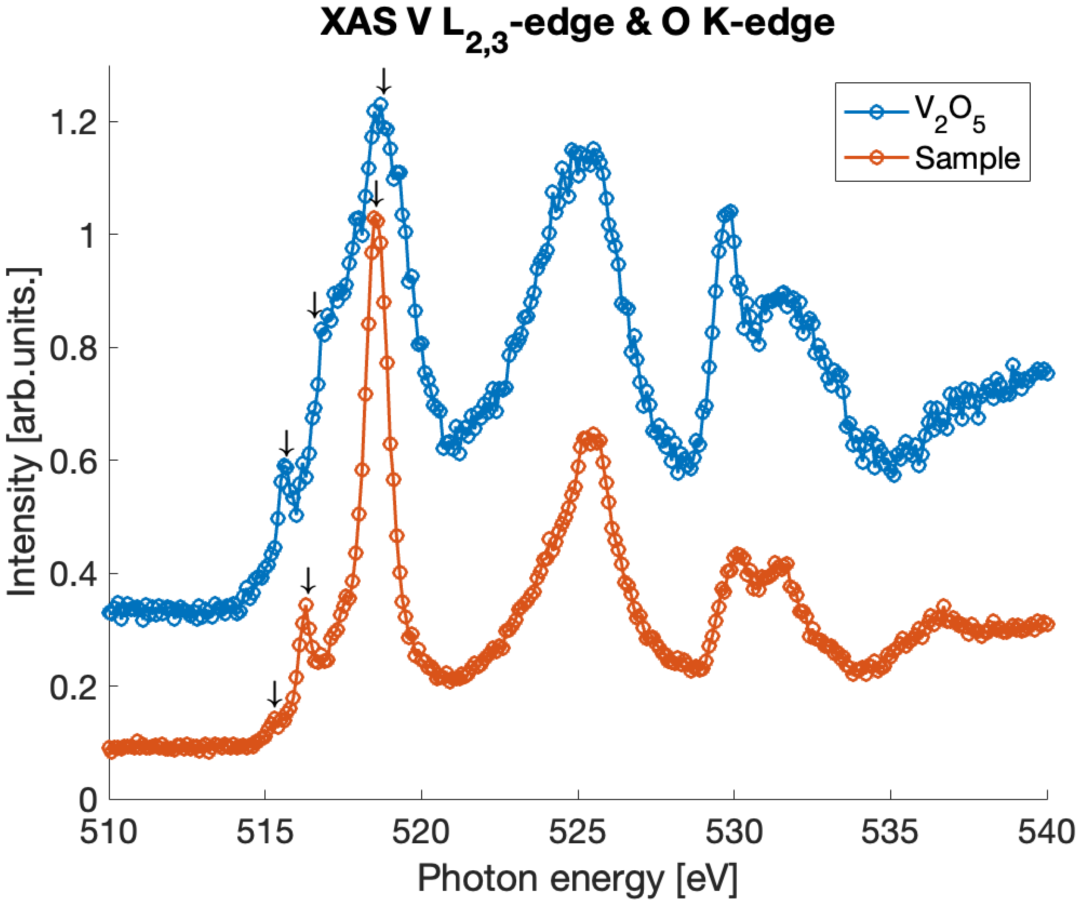

Figure 4.15: NEXAFS spectra of $BaCu_2V_2O_8$ (orange line) and V_2O_5 (blue line) in the vicinity of V $L_{2,3}$-edge and O K-edge.

4.2.5 Magnetic susceptibility measurements in ambient pressure

The samples' magnetic properties were measured at the Advanced Materials Characterisation Facility at the University of Birmingham in collaboration with Dr. Mingee Chung, Dr. Matthew Coak and Dr. Aly Abdeldaim from the Condensed Matter Group.

Experimental settings

The magnetic susceptibility measurements were performed using MPMS3 from Quantum Design. The single crystal was mounted on the sample holder with the magnetic field applied perpendicular to the c-axis of the single crystal.

The sample with mass of 8.5 mg was zero field cooled with cooling rate of 12 K per minute until it reached base temperature of 1.9 K. The measurements of DC moments were taken continuously from 1.9 K to 300 K with a sweep rate of 2 K per minute at magnetic field of 1 T.

General results

Figure 4.16 presents the magnetic susceptibility data of $BaCu_2V_2O_8$ collected over the temperature range from 1.9 K to 300 K in a field of $H = 1$ T applied perpendicular to the c-axis. The data was normalized to obtain the susceptibility per mole of Cu^{2+} magnetic ion. It does not reach the paramagnetic region within the measured temperature range. A broad maximum begins at $T > 200$ K but it cannot be distinguished clearly due to being cut off. A broad maximum would be attributed to the short-range magnetic correlations and is widely observed in quasi-low dimensional systems. Below $T \sim 240$ K the susceptibility drops smoothly until $T \approx 50$ K. The absence of any additional sudden and sharp features suggests the absence of phase transitions in the compound. At temperatures $T < 20$K, the susceptibility increases sharply as the temperature approaches zero. This behavior is named the Curie tail and is attributed to paramagnetic impurities of the crystal structure defects. Apart from the sharp increase due to the impurity contribution, magnetic susceptibility of $BaCu_2V_2O_8$ tends towards zero at a finite temperature. This behavior indicates the presence of the energy gap in the magnetic excitation spectra of $BaCu_2V_2O_8$ and suggests that system is dimerized. However, the temperature at which the susceptibility reaches zero is obscured by the sharp Curie impurity tail.

The low temperature region $1.9 \text{ K} \leq T \leq 15$ K was fitted to account for the impurities' and the temperature independent contributions to the magnetic susceptibility. This helps clearly distinguish the crystal's magnetic behavior from the magnetic properties of the impurities. The impurity and the temperature independent contributions are plotted in the solid red line in figure 4.16. The yellow line in the graph is the fit of the impurity contributions' subtracted from the recorded susceptibility data. It reaches zero between 6.19 K to 6.81 K, confirming the presence of the energy gap.

The magnetic exchange interactions present in $BaCu_2V_2O_8$, the sign and magnitude of the magnetic interactions, can be estimated from the fit analysis using the models that were discussed in section 2.3.

Unfortunately analysis of the Curie-Weiss behavior of the data can not be performed as the sample does not reach the paramagnetic behavior within the measured temperature range.

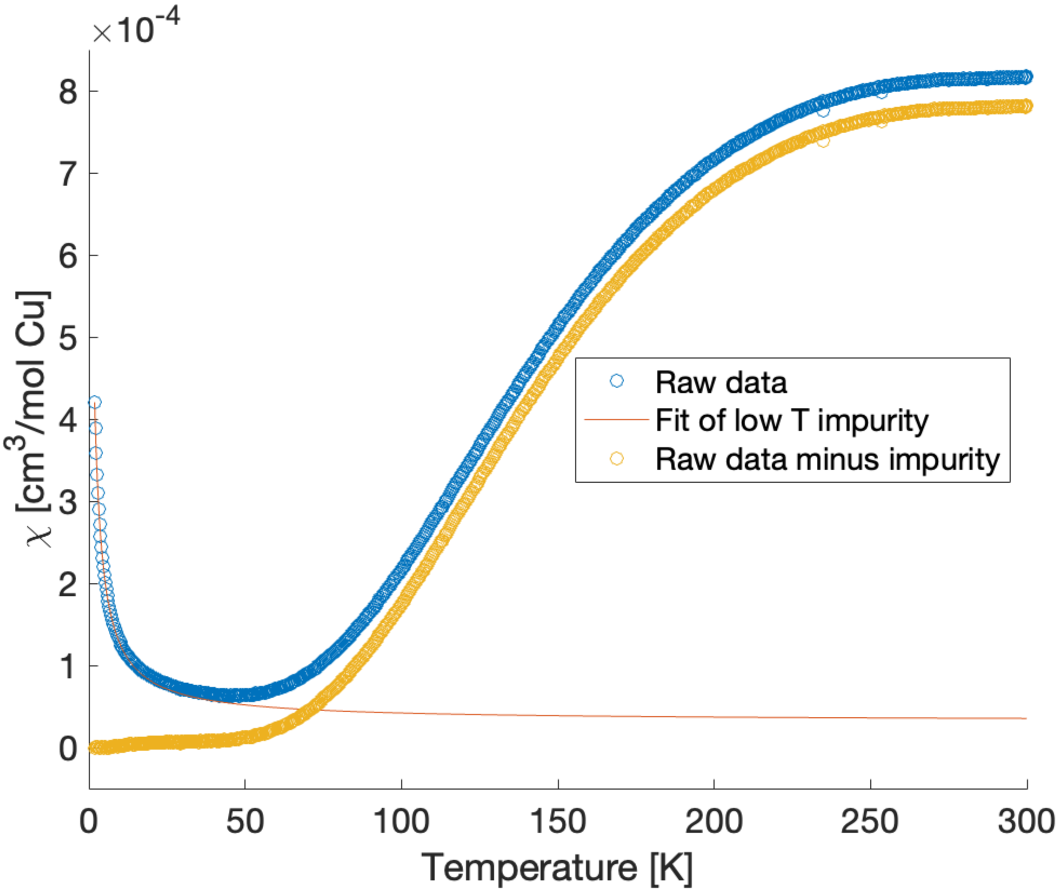

Figure 4.16: The temperature dependence of the raw magnetic susceptibility χ for $BaCu_2V_2O_8$ in an applied field of 1 T, normalized to the molar amount of Cu^{2+} ions.

Fitting data with the isolated dimer model

The black curve in figure 4.17 is the fit of the χ of $BaCu_2V_2O_8$ to the isolated dimer model which is defined by equation 2.9 and 2.10. The extracted parameters were found to be $\chi_0 = 4.41(1) \times 10^{-5}\text{cm}^3/\text{mol}$, $C_{imp} = 8.67(4) \times 10^{-4}\text{cm}^3\text{K/mol}$, $\theta_{CW,imp} = -0.35(1)\text{K}$, $C = 0.5920(4)$ cm^{3}K/mol and $J_{intra} = 40.18(1)$ meV.

The fit of the isolated dimer model with only the dominant intradimer exchange interaction J_{intra} provides a good agreement with the data over whole temperature region. The extracted value of J_{intra} is also in good agreement with the value found from inelastic neutron scattering data. Minimal deviation takes place towards the highest temperature region, above 200 K, of the measurement where a maximum is expected.

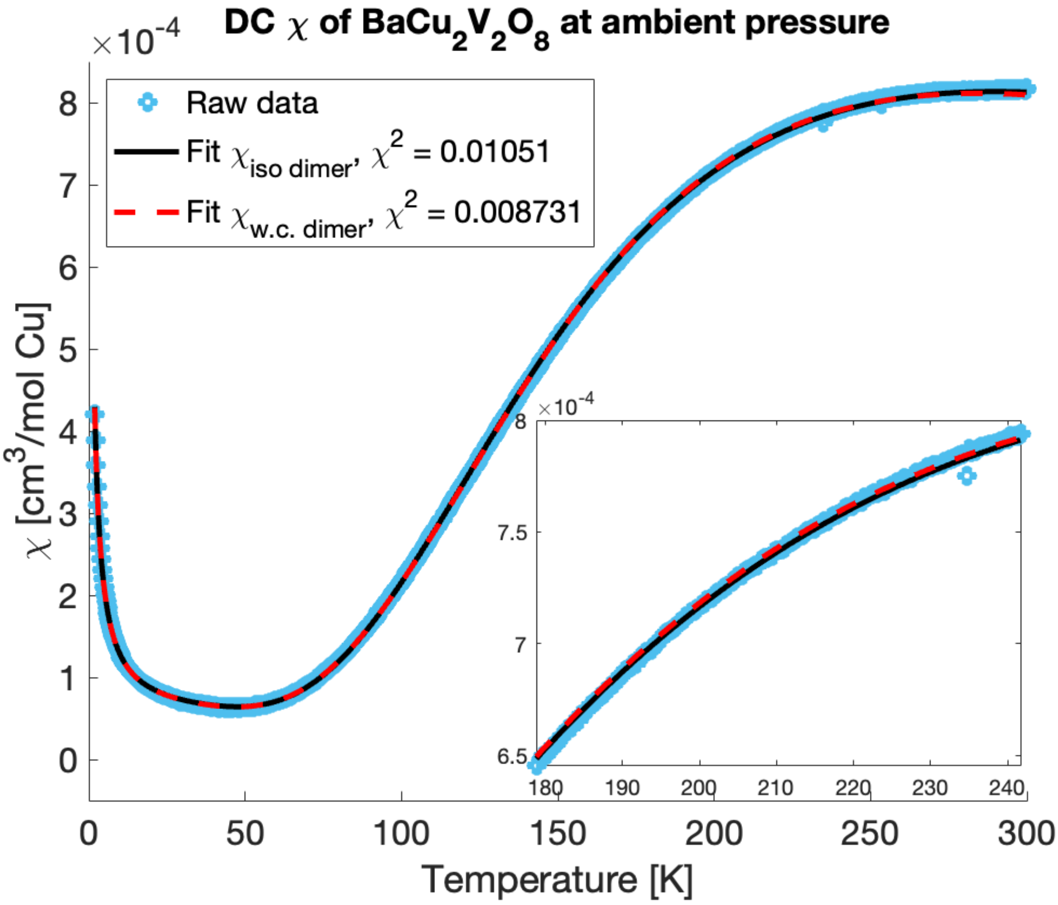

Figure 4.17: The raw susceptibility data χ of $BaCu_2V_2O_8$ fitted with the isolated dimer model and the weakly coupled dimer model. The blue open circles are the raw data points, the black solid line is the fit to the isolated dimer model while the red solid line is the fit to the weakly coupled dimer model. Inset is a closeup of the temperature region between 180 K and 240 K.

Fitting data with the weakly coupled dimer model

The red curve in figure 4.17 is the fit of the raw data to the weakly coupled dimer model as defined by equation 2.9 and 2.11. This model takes into account both the dominant intradimer and the weaker interdimer exchange interactions in $BaCu_2V_2O_8$. The extracted parameters were found to be $\chi_0 = 4.35(1)\times10^{-5}\text{cm}^3/\text{mol}$, $C_{imp} = 8.76(3)\times10^{-4}\text{cm}^3\text{K/mol}$, $\theta_{CW,imp} = -0.38(1)\text{K}$, $C = 0.533(5)$ cm^{3}K/mol, $J_{intra} = 39.39(7)$ meV and $J'_{inter} = -15(1)$ meV.

The weakly coupled dimer model gave an improved agreement with the data compared to the isolated dimer model. This suggests that the interdimer coupling has to be taken into account.

The extracted parameter for the intradimer coupling is in good agreement with previous magnetic susceptibility measurements for the J_{intra} obtained in the same orientation for $BaCu_2V_2O_8$ [11] whereas the interdimer coupling differs. The deviation of J_{inter} can be attributed to the fact that the present measurements were done over a shorter temperature range that did not cover the broad maximum. This is expected to affect the results obtained from the fit analysis with the weakly dimer coupled model. Taking this reason into account we can conclude that the value $J_{inter} = -15(1)$ meV extracted over the temperature range of 2 K - 300 K provides reasonable estimation for the value of of J_{inter}. This is important for the further measurements under applied pressures where the temperatures higher than 300 K are not accessible due to the safety reasons.

The dominant intradimer exchange is antiferromagnetic while the weaker interdimer exchange is ferromagnetic, which is in agreement with previous susceptibility and neutron scattering measurements.

4.2.6 Magnetic susceptibility measurements under applied pressure

The samples' magnetic properties were measured at the Advanced Materials Characterisation Facility at the University of Birmingham in collaboration with Dr. Mingee Chung, Dr. Matthew Coak and Dr. Aly Abdeldaim from the Condensed Matter Group.

Experimental settings

These measurements were also performed using the MPMS3 from Quantum Design.

The same single crystal sample of $BaCu_2V_2O_8$ with a mass of 8.5 mg from the measurement taken in ambient pressure was used. The single crystal was placed inside a Teflon tube with a diameter of 2.1 mm. The tin manometer was placed inside the tube inside the pressure cell before being filled with the pressure transmitting medium Daphne Oil 7373. To apply pressure, the locking nuts on the cell were tightened to compress the cell, obtaining applied pressure on the sample. The applied compression was indicative of the approximate pressure applied as given by the manual for the pressure cell as provided by Quantum Design.

Before starting susceptibility measurements over the whole temperature range, a sweep of the magnetic dc moment from 3.2 K to 3.8 K was taken to determine the applied pressure.

The sample was zero field cooled at 5 K per minute from 300 K to 10 K and then cooled at a rate of 1 K per minute until it reached 1.9 K. A magnetic field of 1 T was applied before measurements were taken. The measurements of DC moments were taken continuously from 1.9 K to 300 K with a sweep rate of 0.8 K per minute.

General results

The measurements of the magnetic susceptibility of $BaCu_2V_2O_8$ were done but the results could not be analyzed directly due to the significant background contribution from the pressure cell relative to the sample's signal. The voltage waveform of the sample under pressure can be seen in Figure 4.18, which differs significantly from a useful voltage waveform (exemplified by Figure 3.5 in chapter 3.4.1). Without a clear signal the susceptibility cannot be extracted from the data because the inbuilt software MultiVu could not fit the voltage waveform of the sample at any temperature. Therefore, additional background measurements of the empty pressure cell with identical experimental conditions are necessary to distinguish the signal of the pressurized sample from the signal from the pressure cell.

However, we were unable to complete supplemental background measurements of $BaCu_2V_2O_8$ in time.

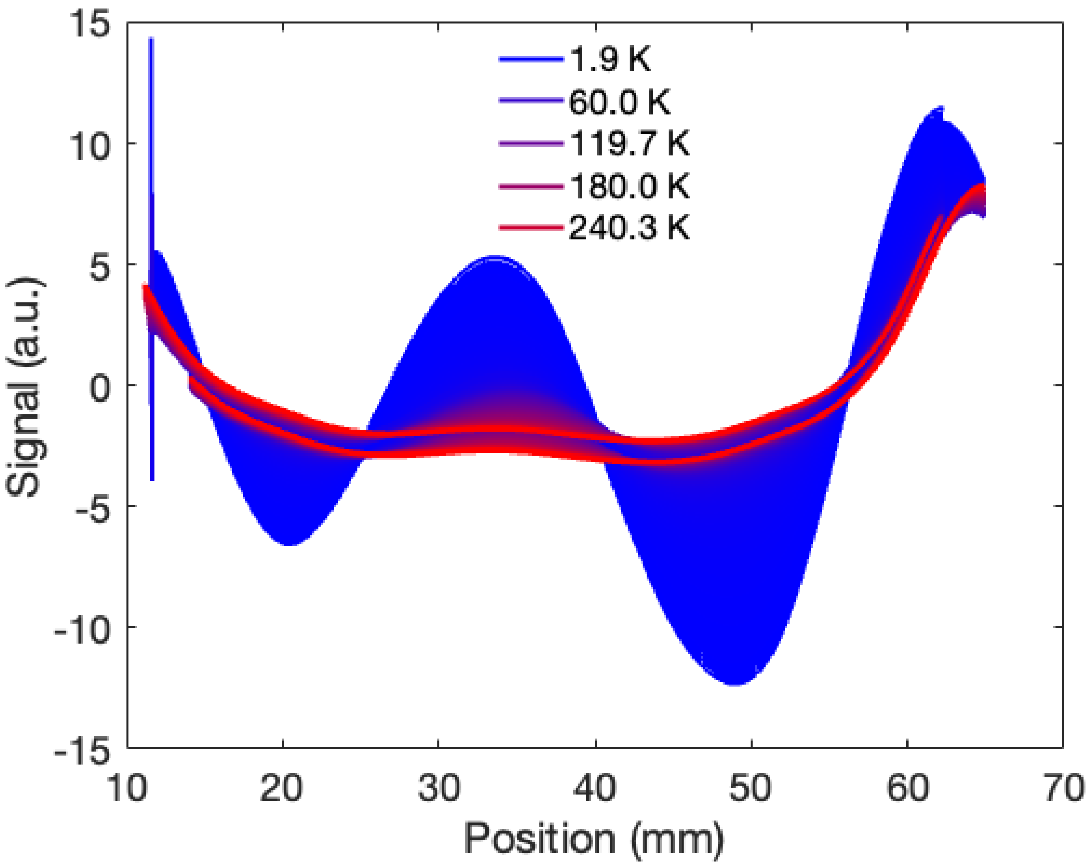

Figure 4.18: The voltage waveform for $BaCu_2V_2O_8$ recorded in the pressure cell under 4.7 kbar of applied pressure in an applied field of 1 T.

Upon deconstruction of the pressure cell an air bubble was found in the pressure medium, as shown in figure C.1 in the appendix.

4.2.7 Conclusion

The synthesis of a polycrystalline sample of $BaCu_2V_2O_8$ was performed using the solid-state reaction. The quality of the sample was explored with PXRD method complemented with XPS and NEXAFS techniques. The powder sample was found to be impure and consisted of 46% and 45% of $BaCu_2V_2O_8$ and $BaCuV_2O_7$ respectively. The spectroscopy measurements revealed that both V and Cu in the explored sample were in their expected valence states.

Magnetic susceptibility measurements of a single crystal $BaCu_2V_2O_8$ collected at ambient conditions yielded results for the intradimer and interdimer couplings $J_{intra} = 39.39(7)$ meV and $J'_{inter} = -15(1)$ meV where J_{intra} was in perfect agreement and J'_{inter} was in reasonable agreement with earlier published results, despite only measuring up to room temperature. This is important information for future analysis under applied pressures where the temperature range of the measurements is limited to room temperature.

The single crystal magnetic susceptibility measurements of $BaCu_2V_2O_8$ were performed but additional measurements of the background from the pressure cell are necessary to further analyze the collected data.

4.3 Strontium copper oxide $SrCuO_2$

4.3.1 Overview

$SrCuO_2$ is a quasi one-dimensional antiferromagnetic cuprate magnet. It has a centered orthorhombic crystal structure with space group $Cmcm$ and with lattice parameters $a = 3.556(2)$ Å, $b = 16.27(4)4$ Å, $c = 3.904(2)$ Å [55]. The coplanar CuO_4 square plaquettes form a crystallographic zigzag chain of Cu^{2+} ions along the c-axis. It was suggested that the Cu^{2+} magnetic ions are bounded by antiferromagnetic magnetic exchange coupling J_2 into straight chains through the $\sim 180°$ Cu-O-Cu bonds, see figure 4.19. These straight chains interact via ferromagnetic intrachain interaction J_1 through the $\sim 90°$ Cu-O-Cu magnetic exchange path [56].

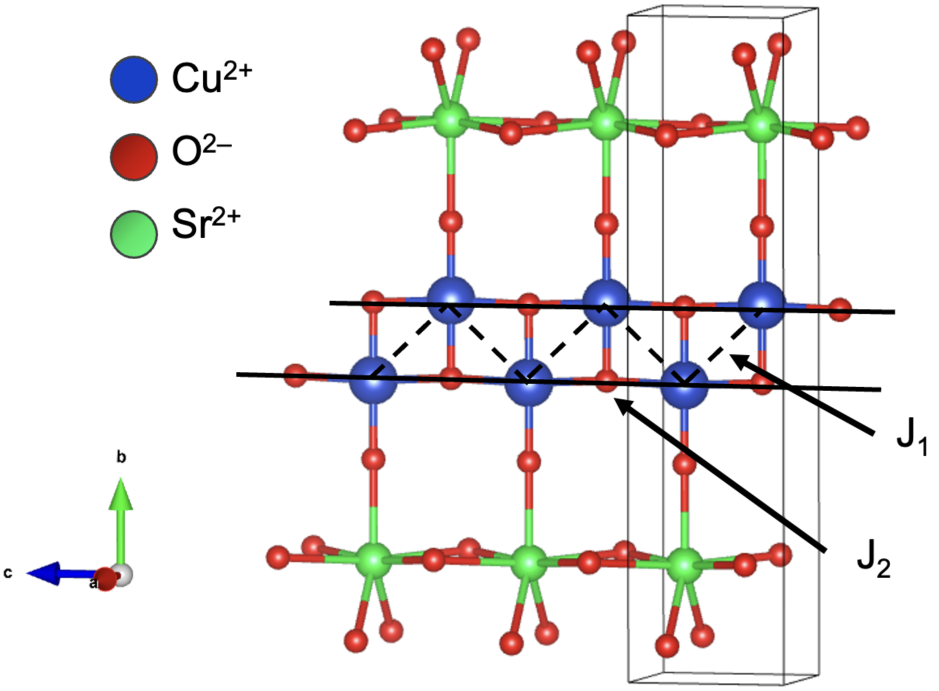

Figure 4.19: Crystal structure of $SrCuO_2$

Thermodynamic measurements of $SrCuO_2$ up to 800 K first suggested that the strong J_2 interaction would be 82 meV [8] before being ammended to 182 meV [57] upon measuring on a single crystal. The ratio between intra- and interchain couplings have been extracted from analysis of the magnetic susceptibility and was estimated to be $J_2/J_1 \sim 10^1 - 10^3$ [8], where the interchain coupling is significantly weaker. The thermodynamic measurements for $SrCuO_2$ were however not conclusive about the interactions. Indeed, the susceptibility measurements suggested values between 82 meV and 190 meV [58] whereas specific heat capacity measurements suggested 224 meV [59], which is much lower then the value of J_2 258 meV estimated from infrared spectroscopy data [60].

Most recently, inelastic neutron scattering measurements concluded that the energy dispersion of $SrCuO_2$ corresponded to that of the spin-$\frac{1}{2}$ Heisenberg chain and with the antiferromagnetic interaction of $J = 226$ meV [55]. The magnetic energy dispersion was gapless and that a uniform 1D chain is the appropriate model describing the magnetism of $SrCuO_2$. The magnetic energy dispersion was gapless and shows that a uniform 1D $S=\frac{1}{2}$ chain is the appropriate model to describe a magnetism of $SrCuO_2$.

The magnetic properties of the Cu^{2+} magnetic ions with spin $\frac{1}{2}$ in $SrCuO_2$ can thus be described by the Hamiltonian [55]:

$$\hat{H} = J\sum_i \vec{S}_i\vec{S}_{i+1}, \tag{4.5}$$

where J is the intrachain coupling while $\vec{S}_i$ and $\vec{S}_{i+1}$ are the spin operators for the ith and neighboring $i+1$ magnetic ions.

Neutron scattering studies also found that rather than developing long range order at low temperatures, the static sublattice in $SrCuO_2$ develops a weak magnetization for $T < 5$ K [61]. The spins freeze and develop short-range order instead. In this thesis we present the polycrystalline synthesis and characterization of $SrCuO_2$.

4.3.2 Synthesis and characterization via powder x-ray diffraction

The powder sample of $SrCuO_2$ was synthesized using solid state reaction

$$SrCO_3 + CuO \longrightarrow SrCuO_2 + \uparrow CO_2, \tag{4.6}$$

where CO_2 evaporates in the process. The precursors $SrCO_3$ (99.99% Thermo Fisher Scientific) and CuO (99.9995% Thermo Fisher Scientific) were mixed in a stochiometric 1:1 molar ratio with 5.9052 g and 3.1816 g respectively to obtain 7.2 g of $SrCuO_2$ powder [8]. The precursors were mixed in a small amount of ethanol before being sintered in an AL23 alumina crucible at 980°C for 30 h total. One instance of intermediate grinding was performed after 15h of sintering. Every sintering instance was heated and cooled at 150°C per hour.

The diffractogram for $SrCuO_2$ was obtained for angles 2θ between 5° and 90° in steps of 0.045° measuring for 5 s per point.

Figure 4.20 shows the refined diffraction pattern of $SrCuO_2$. The data was fitted with a model consisting of its main expected phase $SrCuO_2$ and the precursors. This model reproduce well all observed experimental peaks while the deviation in their intensities can be attributed to the presence of the preferred orientations in the powder sample. The initial parameters of the crystal structures for these phases were taken from published data and then clarified during the refinement [37, 38, 55]. The diffractogram concluded that 96.45% of the sample consisted of $SrCuO_2$, 0.32% of CuO and 3.23% of $SrCO_3$. The lattice parameters of $SrCuO_2$ were $a = 3.56821(4)$ Å, $b = 16.31236(17)$ Å and $c = 3.90905(4)$ Å.

Atom	x	y	z
Cu1	0	0.06103(56)	0.25
Sr1	0	0.33082(39)	0.25
O1	0	0.94828(196)	0.25
O2	0	0.18025(244)	0.25

Table 4.11: Lattice parameters and atomic positions for $SrCuO_2$, refined from PXRD data.

Magnetic susceptibility measurements for $SrCuO_2$ were recorded but not analyzed due to lack of time.

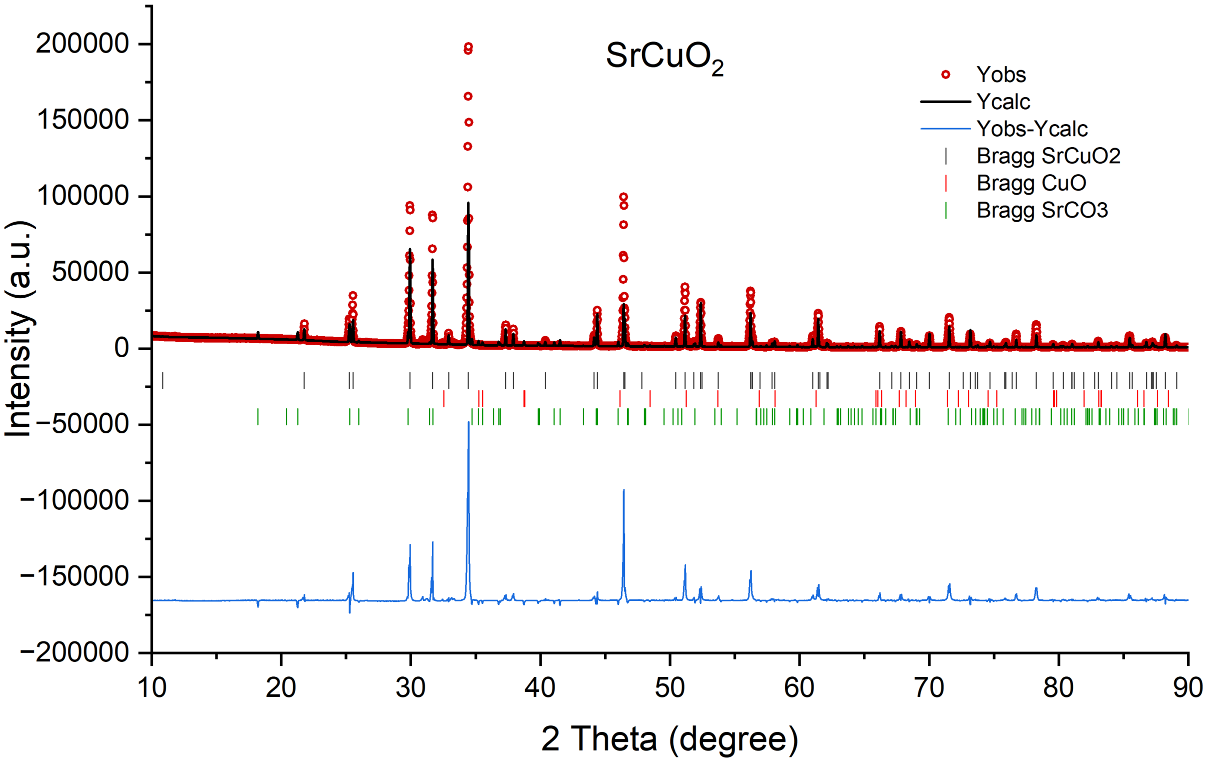

Figure 4.20: Rietveld refinement of the $SrCuO_2$ powder x-ray diffraction data. The red circles are the data points, the black line is the model, the blue line is the difference between data and model and the vertical bars are Bragg peak positions of the different phases included in the model

4.4 Copper germanate $CuGeO_3$

4.4.1 Overview

$CuGeO_3$ is a cuprate 1D spin-Peierls system; one of very few confirmed inorganic spin Peierls compounds. It exhibits a spin-Peierls transition at $T_{SP} = 14$ K [62] where the 1D chain dimerizes. At room temperature, the crystal structure is orthorhombic with space group *Pmma* and lattice parameters $a = 4.801(1)$ Å, $b = 8.469(2)$ Å and $c = 2.943$ Å [63]. The edge-sharing CuO_6 octahedron are surrounded by corner-sharing GeO_4. Linear chains of semi-planar $[CuO_2]^{2-}$ are arranged along the c axis, as shown in figure 4.21. The dimers form along the c-axis as neighboring Cu^{2+} ions couple via two O^{2-} ions.

The magnetic interaction of spins in $CuGeO_3$ was predicted to be one dimensional and to be a uniform 1D Heisenberg chain at temperatures above T_{SP} with intrachain exchange J along the c-axis. Initial thermodynamic measurements of $CuGeO_3$ estimated $J = 7.6$ meV [62] but were clarified using inelastic neutron scattering to be $J = 10.4$ meV [64]. The dispersion measurements also confirmed that the magnetic character in $CuGeO_3$ is one-dimensional along the c-axis, extrapolated that the energy gap at 0 K was 2.1 meV and that the dimerization ratio of $CuGeO_3$ at $T < T_{SP}$ was $\alpha = 0.78$.

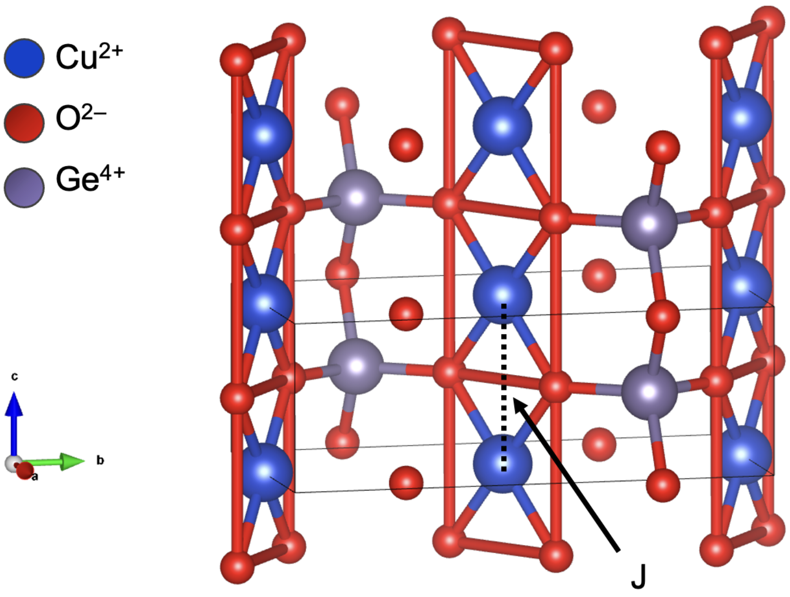

Figure 4.21: The crystal structure of $CuGeO_3$

The pressure effects on the dimerization of $CuGeO_3$ were first explored via AC-susceptibility measurements [65]. The T_{SP} of $CuGeO_3$ was found to increase linearly with pressure up to 1.2 GPa, with $dT_{SP}/dP = 4.8$ K/GPa. T_{SP} was also found to increase to 25 K at 3 GPa using Raman scattering [66]. $CuGeO_3$ had also been studied by inelastic neutron scattering and neutron diffraction. Inelastic neutron scattering found that the magnetic spin-Peierls gap energy increased from 1.8 meV to 4.1 meV with 1.8 GPa of applied pressure [67] alongside the increase of T_{SP}. It was also found that the intrachain exchange constant J decreased with increased pressure. Neutron diffraction found that the effects of pressure were large on the oxygen atoms in the ab plane but small on the Cu ions along the c-axis. However a small decrease in the dimerization of Cu along the c-axis was observed [68]. In this thesis we present the polycrystalline synthesis and characterization of $CuGeO_3$.

4.4.2 Synthesis and characterization via powder x-ray diffraction

The powder sample of $CuGeO_3$ was synthesized using solid state reaction

$$GeO_2 + CuO \longrightarrow CuGeO_3 \tag{4.7}$$

The precursors GeO_2 (99.999% Thermo Fisher Scientific) and CuO (99.9995% Thermo Fisher Scientific) were mixed in a 1:1 molar ratio with 4.18514g and 3.18181g respectively to obtain 7.3 g of $CuGeO_3$ powder [9]. The precursors were mixed in a small amount of ethanol in an agate mortar before being sintered in an AL23 alumina crucible at 950°C for 24 h total. One instance intermediate grinding was performed after 12h of sintering. Every sintering process was heated and cooled at 200°C per hour.

The diffractogram for $CuGeO_3$ was obtained for angles 2θ between 10° and 70° in steps of 0.045° measuring for 8 s per point.

Figure 4.22 shows the refined diffraction pattern of $CuGeO_3$. The data was fitted with a model consisting of its main expected phase $CuGeO_3$ and the precursors. The results reveal that this model reproduce the experimental data very well. The initial parameters of the crystal structures for these phases were taken from published data and then clarified during the refinement [37, 69, 70]. Refinement concluded that there were small amounts of precursors left. The diffractogram concluded that 80.08% of the sample consisted of $CuGeO_3$, 11.78% of CuO and 8.14% of GeO_2. The refined lattice parameters were $a = 4.78802(17)$ Å, $b = 8.46389(26)$ Å and $c = 2.93685(9)$ Å which are in good agreement with the values published in a literature $a = 4.801(1)$ Å, $b = 8.469(2)$ Å and $c = 2.943$ Å [63].

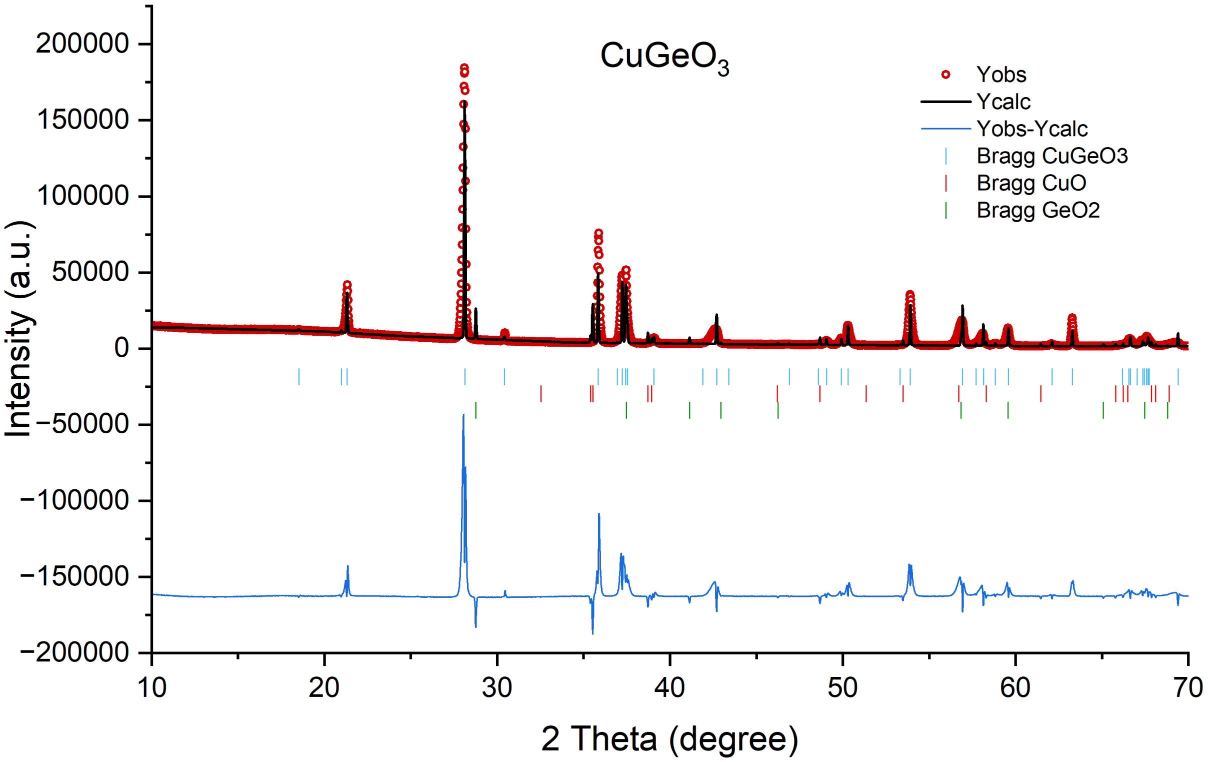

Figure 4.22: Rietveld refinement of the $CuGeO_3$ powder x-ray diffraction data. The red circles are the data points, the black line is the model, the blue line is the difference between data and model and the vertical bars are Bragg peak positions of the different phases included in the model

Atom	x	y	z
Cu	0.5	0	0
Ge	0.07393(393)	0.25	0.5
O1	0.90649(1977)	0.25	0
O2	0.27511(1357)	0.09590(845)	0.5

Table 4.12: Lattice parameters and atomic positions for $CuGeO_3$, refined from PXRD data.

Chapter 5

Summary and Outlook

5.1 Summary

The objective at the start of this thesis was to explore the effects of pressure on the magnetic exchange interactions in different one dimensional and two dimensional quantum magnets with spin-$\frac{1}{2}$.

In summary, this thesis has explored low dimensional quantum magnets and how to synthesize $BaCuSi_2O_6$, $BaCu_2V_2O_8$, $SrCuO_2$ and $CuGeO_3$ via solid-state reactions. Their crystal growth were characterized via PXRD measurements of their bulk crystal structures. The effect of how time affected the purity of the main phase was explored for $BaCuSi_2O_6$. $BaCu_2V_2O_8$ was additionally characterized by XPS and XAS. Magnetic susceptibility measurements of $BaCuSi_2O_6$ and $BaCu_2V_2O_8$ were collected in ambient pressure and under pressure. Through these thermodynamic measurements, we found that pressure increases the interdimer interactions and lowers the dominant intradimer interactions of $BaCuSi_2O_6$. This predicts a broader dispersion but lowering of the gap in the magnetic excitation spectra of $BaCuSi_2O_6$. However, background measurements are necessary to clarify both the extracted intradimer and interdimer exchange couplings to strengthen the conclusions from the susceptibility measurements of $BaCuSi_2O_6$ under pressure. The magnetic susceptibility of $BaCu_2V_2O_8$ measured at ambient pressure was used to establish how confidently the analysis of the interactions was for the available temperature range. Both J_{intra} and J_{inter} extracted from the $BaCu_2V_2O_8$ data measured at ambient pressure within the reduced temperature range are in good agreement with published results. This provided a good foundation for upcoming estimations of how applied pressure would affect the interactions in $BaCu_2V_2O_8$, after appropriate background subtraction.

It is essential to acknowledge the limitations of this study: the lack of background measurements of susceptibility under pressure for $BaCuSi_2O_6$ and those for $BaCu_2V_2O_8$ in particular.

5.2 Future investigation

To further the work started in this project, measurements of the background from the pressure cell at every respective pressure are necessary.

Measurements of the magnetic susceptibility of $SrCuO_2$ in ambient pressure and under applied pressure were performed towards the end of project but the data was not available in time for analysis within this thesis. Recording background measurements and analyzing the data with the models would be a first step in exploring whether $SrCuO_2$ as a one dimensional uniform Heisenberg chain would dimerize upon applying pressure to the material.

The data for the magnetic susceptibility of $BaCu_2V_2O_8$ could be analyzed with the weakly coupled dimer model after correcting for the pressure cell background to see how the magnetic exchange couplings in the one dimensional dimerized Heisenberg chain changes under pressure.

Using the gathered data and background measurements, estimations of the gap can made for $BaCuSi_2O_6$ [42] as further exploration of the 2D dimerized Heisenberg lattice.

In addition, thermodynamic measurements of the heat capacity of the materials investigated in this thesis could be used as a relatively accessible experimental technique to verify the results obtained as well.

Inelastic neutron scattering measurements would be the most conclusive technique to verify the effects of pressure on low dimensional quantum magnets. They would be necessary to confidently conclude the effects of pressure in the magnetic interactions of $BaCuSi_2O_6$.

Bibliography

1. Klyushina, E. *Unconventional magnetic properties of low-dimensional antiferromagnets $BaNi_2V_2O_8$ and $BaCu_2V_2O_8$* PhD thesis (Technischen Universität Berlin, 2017).
2. Blundell, S. *Magnetism in condensed matter* (OUP Oxford, 2001).
3. Barnes, T., Riera, J. & Tennant, D. S= 1/2 alternating chain using multiprecision methods. *Physical Review B* **59,** 11384 (1999).
4. Vasil'ev, A. N., Markina, M. M. & Popova, E. A. Spin gap in low-dimensional magnets (Review). *Low Temperature Physics* **31,** 203–223 (Mar. 2005).
5. Jaime, M. *et al.* Magnetic-Field-Induced Condensation of Triplons in Han Purple Pigment $BaCuSi_2O_6$. *Physical Review Letters* **93,** 087203 (2004).
6. Singh, Y. & Johnston, D. Singlet ground state in the spin-1/2 dimer compound $Sr_3Cr_2O_8$. *Physical Review B* **76,** 012407 (2007).
7. Mugiraneza, S. & Hallas, A. M. Tutorial: a beginner's guide to interpreting magnetic susceptibility data with the Curie-Weiss law. *Communications Physics* **5,** 95 (2022).
8. Matsuda, M. & Katsumata, K. Magnetic properties of a quasi-one-dimensional magnet with competing interactions: $SrCuO_2$. *Journal of magnetism and magnetic materials* **140,** 1671–1672 (1995).
9. Green, M. A., Kurmoo, M., Stalick, J. K. & Day, P. The crystal structure and magnetic properties of $CuGeO_3$. *Journal of the Chemical Society, Chemical Communications,* 1995–1996 (17 1994).
10. Van Well, N. *et al.* Crystal Growth with Oxygen Partial Pressure of the $BaCuSi_2O_6$ and $Ba_{1-x}Sr_xCuSi_2O_6$ Spin Dimer Compounds. *Crystal Growth & Design* **16,** 3416–3424 (2016).
11. Klyushina, E. *et al.* Hamiltonian of the S= 1/2 dimerized antiferromagnetic-ferromagnetic quantum spin chain $BaCu_2V_2O_8$. *Physical Review B* **98,** 104413 (2018).
12. Drioli, E. & Giorno, L. *Comprehensive Membrane Science and Engineering Comprehensive Membrane Science and Engineering* **v. 1,** 222. ISBN: 9780080932507. `https://books.google.se/books?id=1wA_vQ74l3MC` (Elsevier Science, 2010).
13. Koohpayeh, S. Single crystal growth by the traveling solvent technique: A review. *Progress in Crystal Growth and Characterization of Materials* **62.** Special Issue: Recent Progress on Fundamentals and Applications of Crystal Growth; Proceedings of the 16th International Summer School on Crystal Growth (ISSCG-16), 22–34. ISSN: 0960-8974. `https://www.sciencedirect.com/science/article/pii/S0960897416300018` (2016).
14. Rodriguez-Carvajal, J. *FullProf Suite* version 5.10. Sept. 28, 2023. `https://www.ill.eu/sites/fullprof/`.

15. Zagorac, D., Müller, H., Ruehl, S., Zagorac, J. & Rehme, S. Recent developments in the Inorganic Crystal Structure Database: theoretical crystal structure data and related features. *Journal of Applied Crystallography* **52,** 918–925. `https://doi.org/10.1107/S160057671900997X` (Oct. 2019).

16. Downs, R. T. & Hall-Wallace, M. The American Mineralogist Crystal Structure Database. *American Mineralogist* **88,** 247–250. `https://doi.org/10.1107/S160057671900997X` (2003).

17. Vaerst, Olivia. *Internal strain in the magnetocaloric alloy MnCoSi* Student Paper. 2021.

18. Tanuma, S., Powell, C. J. & Penn, D. R. Calculations of electron inelastic mean free paths for 31 materials. *Surface and Interface Analysis* **11,** 577–589 (1988).

19. Shard, A. G. Practical guides for x-ray photoelectron spectroscopy: Quantitative XPS. *Journal of Vacuum Science & Technology A* **38,** 041201. ISSN: 0734-2101. eprint: `https://pubs.aip.org/avs/jva/article-pdf/doi/10.1116/1.5141395/16009771/041201\_1\_online.pdf`. `https://doi.org/10.1116/1.5141395` (July 2020).

20. Stevie, F. A. & Donley, C. L. Introduction to x-ray photoelectron spectroscopy. *Journal of Vacuum Science & Technology A* **38,** 063204. ISSN: 0734-2101. eprint: `https://pubs.aip.org/avs/jva/article-pdf/doi/10.1116/6.0000412/15822858/063204\_1\_online.pdf`. `https://doi.org/10.1116/6.0000412` (Sept. 2020).

21. Stöhr, J. *NEXAFS spectroscopy* (Springer, Berlin : 1992).

22. Newville, M. Fundamentals of XAFS. *Consortium for Advanced Radiation Sources, University of Chicago (USA)[http://xafs. org]* **78** (Jan. 2004).

23. Urpelainen, S. *et al.* The SPECIES beamline at the MAX IV Laboratory: a facility for soft X-ray RIXS and APXPS. *Journal of Synchrotron Radiation* **24,** 344–353 (Jan. 2017).

24. Edgell, M., Paynter, R. & Castle, J. High energy XPS using a monochromated Ag Lα source: resolution, sensitivity and photoelectric cross sections. *Journal of electron spectroscopy and related phenomena* **37,** 241–256 (1985).

25. *MPMS3 - An Introduction (Webinar)* Quantum Design USA. `https://www.youtube.com/watch?v=SdirI2kkdO8`.

26. Buchner, M., Höfler, K., Henne, B., Ney, V. & Ney, A. Tutorial: Basic principles, limits of detection, and pitfalls of highly sensitive SQUID magnetometry for nanomagnetism and spintronics. *Journal of Applied Physics* **124** (2018).

27. Design, Q. *High Pressure Cell for Magnetometry* Brochure. 2019. `https://qd-uki.co.uk/wp-content/uploads/2019/07/High-Pressure-Cell-for-Magnetometry-Brochure-High-Pressure-option.pdf`.

28. Coak, M. J. *et al.* SquidLab—A user-friendly program for background subtraction and fitting of magnetization data. *Review of Scientific Instruments* **91** (2020).

29. Sheptyakov, D. *et al.* Two types of adjacent dimer layers in the low-temperature phase of BaCuSi 2 O 6. *Physical Review B* **86,** 014433 (2012).

30. Sebastian, S. E. *Bose-Einstein condensation in spin dimer compounds* PhD thesis (Stanford University, 2006).

31. Sasago, Y., Uchinokura, K., Zheludev, A. & Shirane, G. Temperature-dependent spin gap and singlet ground state in $BaCuSi_2O_6$. *Physical Review B* **55,** 8357 (1997).

32. Sebastian, S. E. *et al.* Characteristic Bose-Einstein condensation scaling close to a quantum critical point in $BaCuSi_2O_6$. *Phys. Rev. B* **72,** 100404. `https://link.aps.org/doi/10.1103/PhysRevB.72.100404` (10 Sept. 2005).

33. Liu, K. *et al.* Piezochromism and anomalous near-infrared luminescence evolution of BaCuSi 4 O 10 and BaCuSi 2 O 6 via pressure-induced phase transition. *Journal of Materials Chemistry C* **11,** 15833–15840 (2023).

34. Chen, Y., Zhang, Y. & Feng, S. Hydrothermal synthesis and properties of pigments Chinese purple BaCuSi2O6 and dark blue BaCu2Si2O7. *Dyes and Pigments* **105,** 167–173. ISSN: 0143-7208. `https://www.sciencedirect.com/science/article/pii/S0143720814000242` (2014).

35. Sparta, K. M. & Roth, G. Reinvestigation of the structure of $BaCuSi_2O_6$ – evidence for a phase transition at high temperature. *Acta Crystallographica Section B* **60,** 491–495. `https://doi.org/10.1107/S0108768104011644` (Oct. 2004).

36. Yamada, T., Hiroi, Z. & Takano, M. Spin-1/2 Quantum Antiferromagnetic Chains with Tunable Superexchange Interactions Found in BaCu2(Si1xGex)2O7. *Journal of Solid State Chemistry* **156,** 101–109. ISSN: 0022-4596. `https://www.sciencedirect.com/science/article/pii/S0022459600989680` (2001).

37. Åsbrink, S. & Norrby, L.-J. A refinement of the crystal structure of copper(II) oxide with a discussion of some exceptional e.s.d.'s. *Acta Crystallographica Section B* **26,** 8–15. `https://doi.org/10.1107/S0567740870001838` (Jan. 1970).

38. De Villiers, J. P. Crystal structures of aragonite, strontianite, and witherite. *American Mineralogist: Journal of Earth and Planetary Materials* **56,** 758–767 (1971).

39. d'Amour, H., Denner, W. & Schulz, H. Structure determination of α-quartz up to 68 x 10^8 Pa. *Acta Crystallographica Section B* **35,** 550–555. `https://doi.org/10.1107/S056774087900412X` (Mar. 1979).

40. Lin, H. C., Liao, F. L. & Wang, S. L. Structure of $BaCuSi_4O_10$. *Acta Crystallographica Section C* **48,** 1297–1299. `https://doi.org/10.1107/S0108270192001203` (July 1992).

41. I: Refinement of the crystal structures of Ba4[Si6O16], Ba5[Si8O21] and Ba6[Si10O26], silicates with triple, quadruple and quintuple chains. *Zeitschrift für Kristallographie - Crystalline Materials* **153,** 3–17. `https://doi.org/10.1524/zkri.1980.0002` (1980).

42. Johnston, D. C. *et al.* Thermodynamics of spin $S = 1/2$ antiferromagnetic uniform and alternating-exchange Heisenberg chains. *Phys. Rev. B* **61,** 9558–9606. `https://link.aps.org/doi/10.1103/PhysRevB.61.9558` (14 Apr. 2000).

43. Quintero-Castro, D. L. *et al.* Magnetic excitations of the gapped quantum spin dimer antiferromagnet Sr 3 Cr 2 O 8. *Physical Review B* **81,** 014415 (2010).

44. Ma, D.-p., Ma, N., Ma, X.-d. & Zhang, H.-m. ENERGY SPECTRUM AND g FACTOR OF MgO:Ni2+ AND THEIR PRESSURE-INDUCED SHIFT. *Journal of Physics and Chemistry of Solids* **59,** 1211–1217. ISSN: 0022-3697. `https://www.sciencedirect.com/science/article/pii/S0022369798000523` (1998).

45. Mejía-Salazar, J. R. & Porras-Montenegro, N. Hydrostatic pressure effects on the Landé g factor in GaAs–Ga1xAlxAs quantum heterostructures under applied magnetic fields. *Journal of Applied Physics* **107,** 084311. ISSN: 0021-8979. eprint: `https://pubs.aip.org/aip/jap/article-pdf/doi/10.1063/1.3374700/13651662/084311\_1\_online.pdf`. `https://doi.org/10.1063/1.3374700` (Apr. 2010).

46. Vogt, R. & Müller-Buschbaum, H. BaCu2V2O8: Eine Variante des SrNi2V2O8-Typs, mit Cu2+ in 4+ 1+ 1-Koordination. *Zeitschrift für anorganische und allgemeine Chemie* **591,** 167–173 (1990).

47. Vogt, R. & Müller-Buschbaum, H. BaCuV2O7: Das letzte Glied der Reihe MCuV2O7 (M Mg2+, Ca2+, Sr2+, Ba2+). *Journal of the Less Common Metals* **171,** L35–L39. ISSN: 0022-5088. `https://www.sciencedirect.com/science/article/pii/002250889190139U` (1991).

48. Shklover, V., Haibach, T., Ried, F., Nesper, R. & Novák, P. Crystal Structure of the Product of Mg2+Insertion into V2O5Single Crystals. *Journal of Solid State Chemistry* **123,** 317–323. ISSN: 0022-4596. `https://www.sciencedirect.com/science/article/pii/S0022459696901863` (1996).

49. Golovkin, B. & Pakhnutova, N. BaO-CuO-V2O5 phase diagram. *Russian Journal of Inorganic Chemistry* **44,** 1120–1123 (July 1999).

50. Yeh, J. & Lindau, I. Atomic subshell photoionization cross sections and asymmetry parameters: 1 Z 103. *Atomic data and nuclear data tables* **32,** 1–155 (1985).

51. Henzler, K. *et al.* Investigation of reactions between trace gases and functional CuO nanospheres and octahedrons using NEXAFS-TXM imaging. *Scientific reports* **5,** 17729 (2015).

52. Gurevich, A. B., Bent, B. E., Teplyakov, A. V. & Chen, J. G. A NEXAFS investigation of the formation and decomposition of CuO and Cu2O thin films on Cu(100). *Surface Science* **442,** L971–L976. ISSN: 0039-6028. `https://www.sciencedirect.com/science/article/pii/S0039602899009139` (1999).

53. Zimmermann, R., Claessen, R., Reinert, F., Steiner, P. & Hüfner, S. Strong hybridization in vanadium oxides: evidence from photoemission and absorption spectroscopy. *Journal of Physics: Condensed Matter* **10,** 5697 (1998).

54. Goering, E. *et al.* Angular-dependent soft X-ray absorption spectroscopy of V2O5 and V6O13. *Physica B: Condensed Matter* **208-209.** Proceedings of the 8th International Conference on X-ray Absorption Fine Structure, 300–302. ISSN: 0921-4526. `https://www.sciencedirect.com/science/article/pii/092145269400847O` (1995).

55. Zaliznyak, I. *et al.* Spinons in the Strongly Correlated Copper Oxide Chains in $SrCuO_2$. *Physical Review Letters* **93,** 087202 (2004).

56. Matsuda, M. *et al.* Magnetic phase transition in the S= zigzag-chain compound $SrCuO_2$. *Phys. Rev. B* **55,** R11953–R11956. `https://link.aps.org/doi/10.1103/PhysRevB.55.R11953` (18 May 1997).

57. Motoyama, N., Eisaki, H. & Uchida, S. Magnetic susceptibility of ideal spin 1/2 Heisenberg antiferromagnetic chain systems, Sr 2 CuO 3 and SrCuO 2. *Physical review letters* **76,** 3212 (1996).

58. Eisaki, H., Motoyama, N. & Uchida, S. Spin magnetic susceptibility of Cu O chains in Sr2CuO3 and SrCuO2. *Physica C: Superconductivity* **282,** 1323–1324 (1997).

59. Sologubenko, A. *et al.* Thermal conductivity and specific heat of the linear chain cuprate Sr 2 CuO 3: Evidence for thermal transport via spinons. *Physical Review B* **62,** R6108 (2000).

60. Suzuura, H., Yasuhara, H., Furusaki, A., Nagaosa, N. & Tokura, Y. Singularities in optical spectra of quantum spin chains. *Physical review letters* **76,** 2579 (1996).

61. Zaliznyak, I., Broholm, C., Kibune, M., Nohara, M. & Takagi, H. Anisotropic spin freezing in the S= 1/2 zigzag chain compound SrCuO 2. *Physical Review Letters* **83,** 5370 (1999).

62. Hase, M., Terasaki, I. & Uchinokura, K. Observation of the spin-Peierls transition in linear Cu^{2+} (spin-1/2) chains in an inorganic compound $CuGeO_3$. *Physical Review Letters* **70,** 3651 (1993).

63. Braden, M. *et al.* Structural analysis of $CuGeO_3$: Relation between nuclear structure and magnetic interaction. *Phys. Rev. B* **54,** 1105–1116. `https://link.aps.org/doi/10.1103/PhysRevB.54.1105` (2 July 1996).

64. Nishi, M., Fujita, O. & Akimitsu, J. Neutron-scattering study on the spin-Peierls transition in a quasi-one-dimensional magnet $CuGeO_3$. *Physical Review B* **50,** 6508 (1994).

65. Takahashi, H., Mori, N., Fujita, O., Akimitsu, J. & Matsumoto, T. Effect of pressure on the magnetic susceptibility in spin-Peierls cuprate, CuGeO3. *Solid state communications* **95,** 817–822 (1995).

66. Goñi, A. R., Zhou, T., Schwarz, U., Kremer, R. K. & Syassen, K. Pressure-Temperature Phase Diagram of the Spin-Peierls Compound $CuGeO_3$. *Phys. Rev. Lett.* **77,** 1079–1082. `https://link.aps.org/doi/10.1103/PhysRevLett.77.1079` (6 Aug. 1996).

67. Nishi, M., Fujita, O., Akimitsu, J., Kakurai, K. & Fujii, Y. High-pressure effects on the spin-Peierls compound CuGeO 3. *Physical Review B* **52,** R6959 (1995).

68. Katano, S., Fujita, O., Akimitsu, J. & Nishi, M. Pressure effects on the dimerization in the spin-Peierls state of $CuGeO_3$. *Phys. Rev. B* **52,** 15364–15367. `https://link.aps.org/doi/10.1103/PhysRevB.52.15364` (21 Dec. 1995).

69. Braden, M. *et al.* Pressure dependence of the crystal structure of CuGeO 3 to 6.2 GPa by neutron diffraction. *Physical Review B* **60,** 9616 (1999).

70. Baur, W. H. & Khan, A. A. Rutile-type compounds. IV. SiO2, GeO2 and a comparison with other rutile-type structures. *Acta Crystallographica Section B: Structural Crystallography and Crystal Chemistry* **27,** 2133–2139 (1971).

Appendix A: The effect of the *g*-factor on the fit for J $\mathbf{BaCuSi_2O_6}$

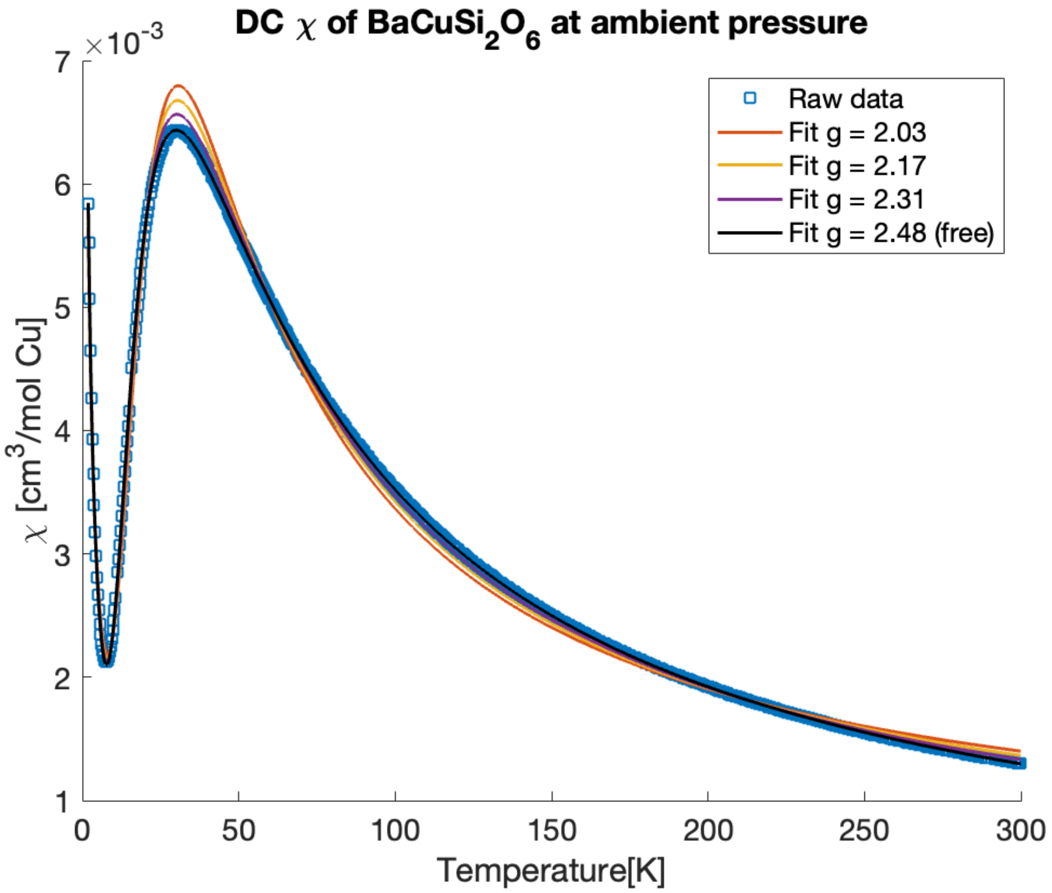

Figure A.1: The raw susceptibility data χ of $BaCuSi_2O_6$ in ambient pressure fitted with the weakly coupled dimer model with different g-factors. The blue open squares are the raw data points and the different lines are different fixed g-factors.

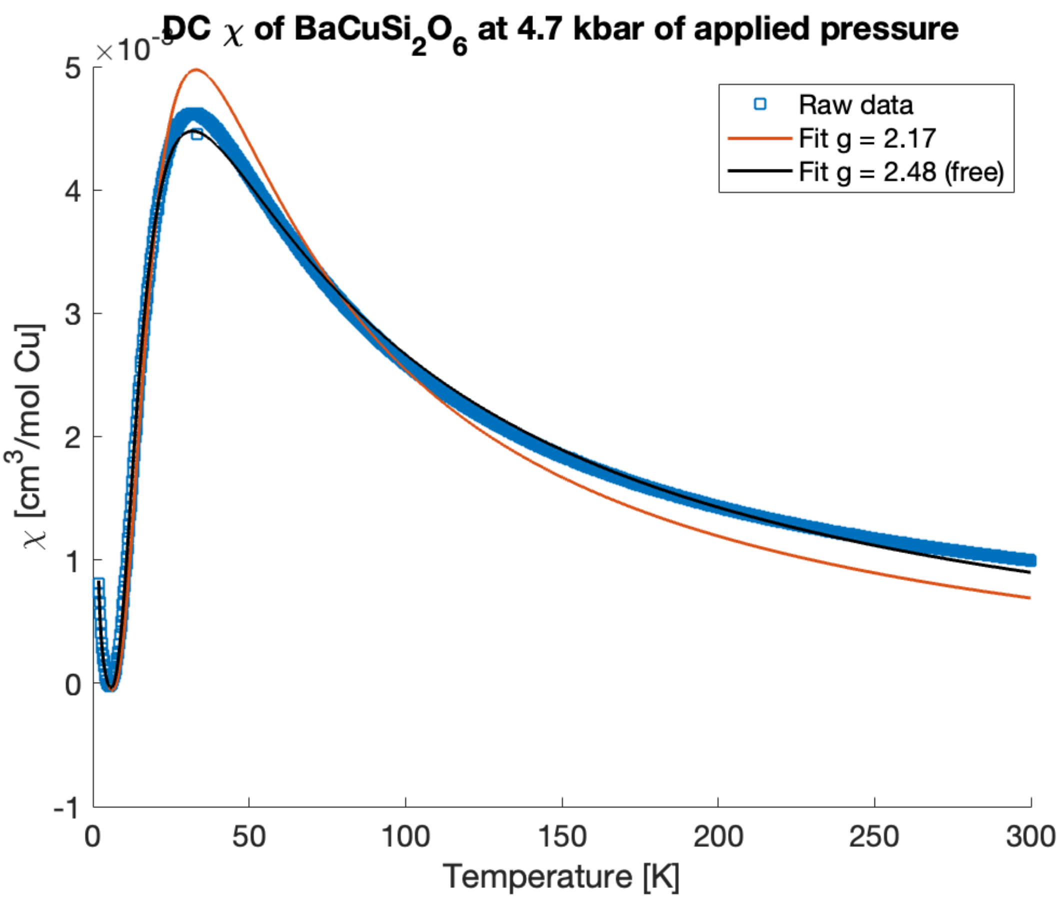

Figure A.2: The raw susceptibility data χ of $BaCuSi_2O_6$ under 4.7 kbar of applied pressure fitted with the weakly coupled dimer model with different g-factors. The blue open squares are the raw data points and the different lines are different fixed g-factors.

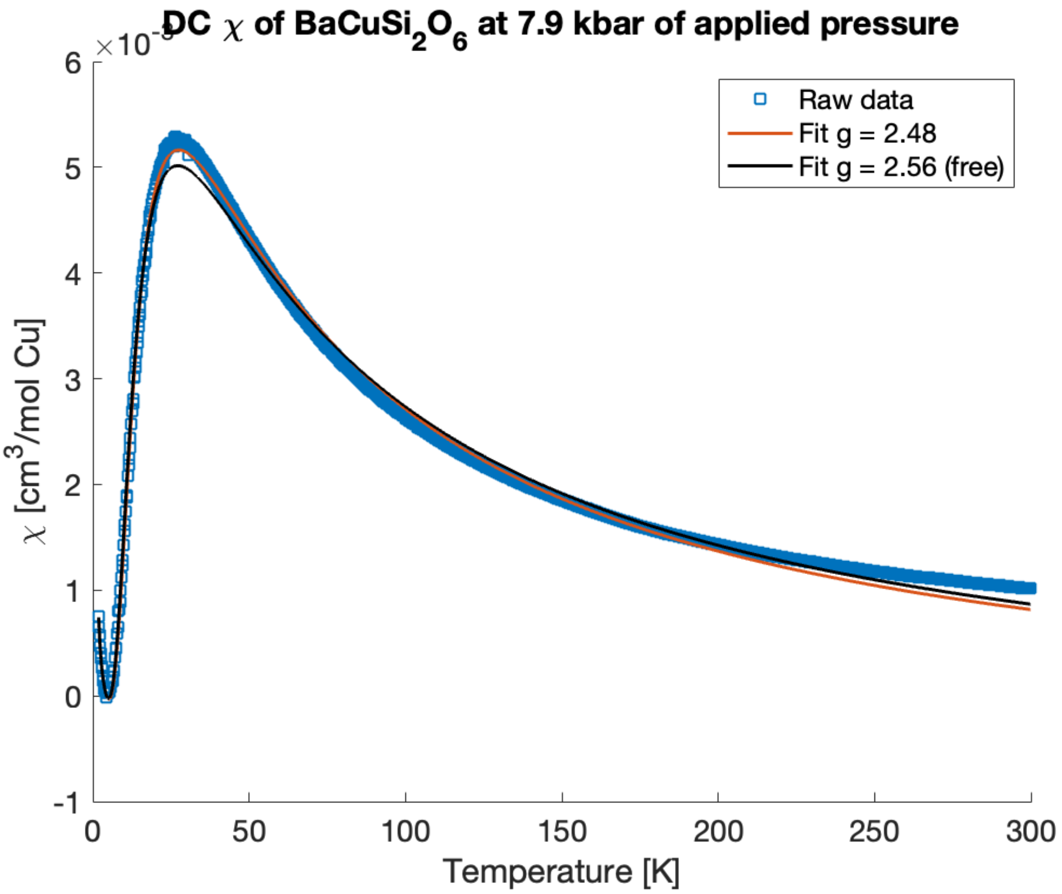

Figure A.3: The raw susceptibility data χ of $BaCuSi_2O_6$ under 7.9 kbar of applied pressure fitted with the weakly coupled dimer model with different g-factors. The blue open squares are the raw data points and the different lines are different fixed g-factors.

Appendix B: Flux of SPECIES beamline

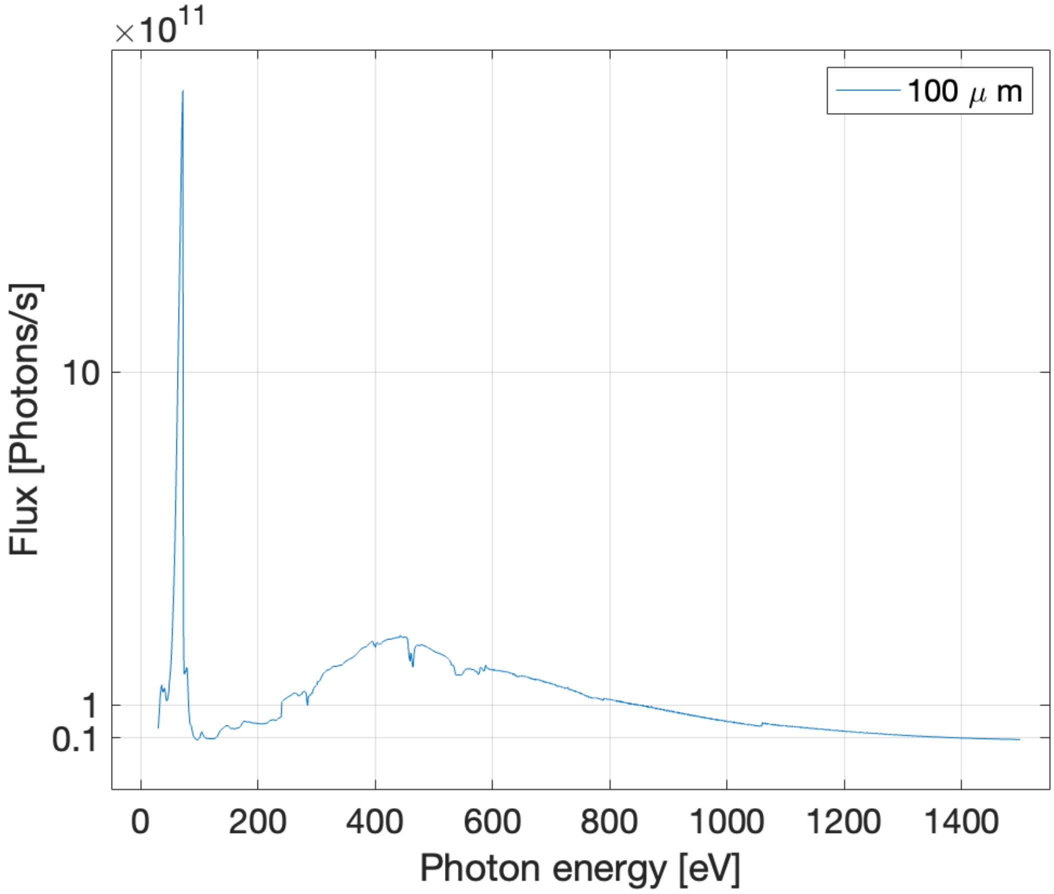

Figure B.1: Approximate flux inside the ambient pressure cell of the AP-XPS chamber. Values measured for fixed slit and 400 mA ring current.

Appendix C: $BaCu_2V_2O_8$ under applied pressure

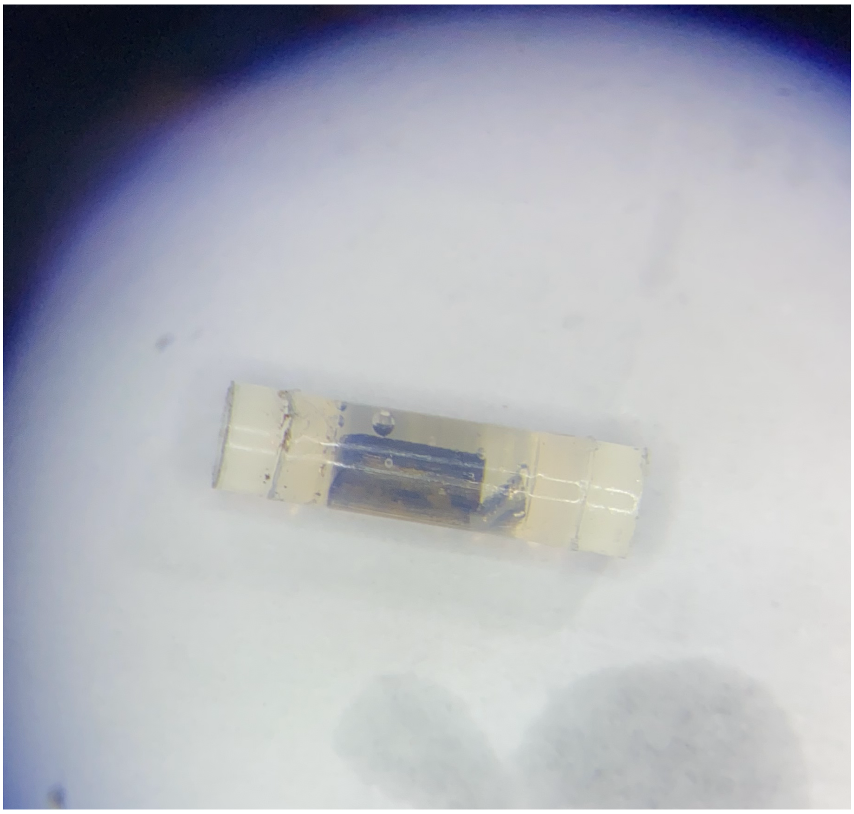

Figure C.1: Single crystal $BaCu_2V_2O_8$ and tin manometer in closed Teflon tube filled with Daphne 7373. Air bubble visible above the single crystal. Image taken using microscope after completed measurements.